Department of Physics and Astronomy

University of Heidelberg

Diploma thesis

in Physics

submitted by

Benjamin Andreas Heß

born in Hünfeld

2011

Online Electron Identification for Triggering

with the ALICE Transition Radiation Detector

This diploma thesis has been carried out by Benjamin Andreas Heß

at the

Physikalisches Institut

under the supervision of

Frau Prof. Dr. Johanna Stachel

Online Elektronen-Identifikation auf Trigger-Ebene mit dem ALICE Übergangsstrahlungsdetektor (TRD)

A Large Ion Collider Experiment (ALICE) am *Large Hadron Collider* (LHC) am CERN hat mit der Untersuchung der Eigenschaften des *Quark-Gluon-Plasmas* (QGP) begonnen. Das QGP wird dabei in hochrelativistischen Schwerionen-Kollisionen erzeugt. Ein Trigger für Elektronen und Jets mit hohem Transversalimpuls ermöglicht die Auswahl interessanter Ereignisse. Für diesen Zweck kann der ALICE Übergangsstrahlungsdetektor (TRD) verwendet werden, denn er besitzt eine sehr schnelle Spurrekonstruktion in der Elektronik zu Level-1-Zeit und eine gute Elektron-Pion-Separation für hohe Impulse.

Auf einer frühen Trigger-Ebene (Level 0) befindet sich der Pre-Trigger, der die TRD-Elektronik bei potentiell interessanten Ereignissen aktiviert. Ein spezialisierter Level-0-Trigger ermöglicht eine Anreicherung der Datensätze, zum Beispiel zwecks der Analyse des Υ's. Im ersten Teil dieser Arbeit wird die Realisierbarkeit eines Υ-Topologie-Triggers durch das TRD Pre-Trigger-System unter Verwendung von Daten des ALICE Flugzeit-Detektors (TOF) untersucht.

Der zweite Teil dieser Arbeit beschäftigt sich mit der Teilchen-Identifikation des TRDs, die auf Look-Up-Tabellen basiert. Die Güte der Teilchen-Identifikation hängt von verschiedenen Parametern ab, wie etwa der Gasverstärkung oder der Driftgeschwindigkeit. Der Einfluss solcher Parameter auf die Güte der Teilchen-Identifikation wird systematisch anhand von Monte-Carlo- und Detektorsimulationen analysiert.

Online Electron Identification for Triggering with the ALICE Transition Radiation Detector

A Large Ion Collider Experiment (ALICE) at the Large Hadron Collider (LHC) at CERN has started studying the properties of the Quark-Gluon Plasma (QGP). At the LHC, the QGP is created in ultrarelativistic heavy-ion collisions. A trigger on high-p_t electrons and jets allows for the selection of interesting events. The ALICE Transition Radiation Detector (TRD) is a fast tracker at level 1 with good e/π-separation for high momenta and can be used as such a trigger.

An early stage of triggering (level 0) provides a pretrigger that wakes up the TRD electronics in case of potentially interesting events. A dedicated level 0 trigger allows to enrich data samples, e.g. for Υ analysis. In the first part of this thesis, the feasibility of an Υ topology trigger from the TRD pretrigger system using information from the ALICE Time Of Flight (TOF) detector is investigated.

The second part of this thesis studies the Particle Identification (PID) of the TRD, which is based on look-up tables. The PID performance depends on several parameters, like gas gain and drift velocity. The impact of such parameters on the PID performance is systematically analysed with Monte Carlo and detector simulations.

Contents

List of Figures

List of Figures

List of Tables

1. Introduction

Mankind has always been curious and tried to understand nature. With the rise and fall of whole empires over the ages, scientists around the world contributed their part to the puzzle of understanding and describing the world or even the whole universe, they lived in. In the last centuries, the knowledge about what the universe is made of underwent a real revolution by a series of experiments in the field of particle physics. Various constituents of matter, like electrons, quarks and gluons, have been discovered. The gathering of all these insights into the fundamental structure of matter and the interactions between the constituents culminated in the formulation of a theory which is able to explain almost all observations made until today: the Standard Model of particle physics.

Despite the great efforts of ancient generations, there are still many mysteries left to resolve. Among other issues, the Standard Model relies on parameters, such as particle masses, that are not predicted by this theory, but need to be taken as input from experiments. Even the mass generation itself is not well understood: The Standard Model postulates a particle, the Higgs boson, which is presumed to be responsible for the generation of mass by its coupling to other particles. Though, the Higgs boson is the only particle in the Standard Model that has not been discovered yet.

Investigating such issues of the microcosm can also help to better understand the macrocosm. An open question for the latter is the evolution of the early universe, around 10 μs after the Big Bang. Within this period, the temperature was above a critical temperature of about $T_{\mathrm{crit}} \approx 170$ MeV [1] (cf. Fig. 1.1, p. 4) such that the matter is expected to have been in a state called Quark-Gluon Plasma (QGP). Understanding this phase of matter and its transition to normal baryonic matter is crucial. It will improve the knowledge about the evolution of the universe and can be used to test Standard Model predictions.

The Large Hadron Collider (LHC) with its experiments addresses these issues. In particular, one of the LHC experiments, ALICE (**A L**arge **I**on **C**ollider **E**xperiment), is focused on the study of the QGP. So, a new era of high-energy physics experiments has started to help to resolve some of the remaining mysteries. This thesis is intended to contribute its small part to the world-puzzle.

In this diploma thesis, two topics have been explored. First, the feasibility of an Υ topology trigger at level 0 with information from the Time Of Flight (TOF) detector has been investigated. In particular, this topic has been investigated with regard to a potential pretrigger for the ALICE Transition Radiation Detector

(TRD). Second, the impact of numerous parameters, such as gas gain and drift velocity, on the online Particle Identification (PID) has been studied in detail.

The theoretical and experimental background is discussed in chapters 1 and 2, including a short introduction to the Standard Model and the quark-gluon plasma. Chapter 3 describes the feasibility study of an Υ topology level 0 trigger. The second topic of this thesis, the online PID, is the subject of chapter 4. The subsequent chapters present, summarise and discuss the results. The appendix contains an overview of the ALICE coordinate system, listings of the used settings for the simulations of the Multi-Chip Modules (MCM) and the Global Tracking Unit (GTU), a collection of all PID performance results and a list of acronyms.

1.1. The Standard Model

Most of the knowledge about elementary particles and their interactions, that has been gathered through a huge number of experiments, has been put into the Standard Model. Within this model, all existing matter is made of 12 fundamental fermions with spin 1/2, that are listed in Tab. 1.1, their anti-particles and gluons (spin 1 bosons, see below). These particles are subject to the three fundamental interactions of the Standard Model — electromagnetic, weak and strong interaction — that are mediated by gauge bosons with spin 1 (see Tab. 1.2). The fourth fundamental interaction, gravity, is not included in the Standard Model. To date, there is no theory on quantum gravitation with distinct predictions and the postulated mediator of this interaction, the graviton, has not yet been discovered. Since gravitational interactions are by far the weakest of all fundamental interactions, they are usually negligible in collider experiments. Thus, they will not be considered further in this thesis.

Generation	Lepton	q/e	$\mathrm{m}{\cdot}c^2$	Quark	q/e	$\mathrm{m}_{\mathrm{bare}}{\cdot}c^2$
First	ν_e	0	< 225 eV	u	$2/3$	1.7 - 3.1 MeV
	e^-	-1	511 keV	d	$-1/3$	4.1 - 5.7 MeV
Second	ν_μ	0	< 0.19 MeV	c	$2/3$	≈ 1.3 GeV
	μ^-	-1	106 MeV	s	$-1/3$	80 - 130 MeV
Third	ν_τ	0	< 18.2 MeV	t	$2/3$	≈ 173 GeV
	τ^-	-1	1.78 GeV	b	$-1/3$	≈ 4.2 GeV

Table 1.1.: Fundamental fermions of the Standard Model. Anti-particles are not shown. The charge q is given in units of the electron charge e and the limits for the neutrino masses are stated with 95% CL (note that smaller mass limits exist for $\bar{\nu}_e$). The values have been taken from [2], where also information about the experiments leading to these results can be found. In the Standard Model, the neutrinos are assumed to be massless.

Interaction	Gauge boson(s)	Coupling to
Electromagnetic	γ	Electric charge
Weak	Z^0, $W^\pm$	$\begin{cases} \text{Weak charge} \\ W^\pm \text{ also to electric charge} \end{cases}$
Strong	8 gluons	Colour charge

Table 1.2.: Interactions of the Standard Model. The interactions between particles are described by the exchange of gauge bosons that couple to their specific charge. In the Standard Model, the electromagnetic and weak interactions are unified and described by the electroweak theory.

The fundamental particles can be grouped into 3 generations (see Tab. 1.1). Until now, neither a heavy bottom-like quark of a fourth generation has been found [3], nor any other particle beyond the third generation (cf. [2]).

All other particles that have been discovered so far are only bound states of the fundamental particles. For instance, (anti-)baryons as the (anti-)proton are described by three (anti-)valence quarks in a sea of gluons and pairs of quarks and anti-quarks. In case of mesons, instead of three valence quarks there are a quark and an anti-quark, which can have different flavours.

The Standard Model is based on Quantum Field Theories (QFT) [4, 5], like Quantum Electrodynamics (QED). QED describes electromagnetic interactions between particles, mediated via photon exchange, very successfully. Therefore, QED has been used as a template for later QFTs. In the Standard Model, QED has been extended to a quantum electroweak theory, that unifies the electromagnetic and the weak interaction. On the other hand, the QFT of strong interactions is Quantum Chromodynamics (QCD). In QCD, the exchange of gluons between colour-charged objects is responsible for strong interactions.

Although the Standard Model describes most of today's observations, there are some measurements that cannot be explained by it, like non-vanishing neutrino masses (the Standard Model assumes the neutrinos to be massless) or the origin and existence of dark matter. Furthermore, the Standard Model gives no answer to questions like: *Why are there 3 families of particles? Why do these particles have such masses, that differ by orders of magnitude? etc.*

Another fundamental problem is the question how all particles acquire their mass, in particular the W and Z bosons. In the Standard Model, the mass of particles results from their coupling to the Higgs boson. However, the Higgs boson has not been discovered yet.

All this gives rise to physics beyond the Standard Model, which will also be searched for in high-energy collisions at the Large Hadron Collider. In particular, this means that the Standard Model is not considered to be a complete theory of particle physics, but only a low-energy limit of a complete theory.

1.2. Heavy-Ion Physics and the Quark-Gluon Plasma

In contrast to other interactions, the mediators of the strong interaction, the gluons, themselves carry colour charge, to which they couple. This results in the self-coupling of gluons, leading to the interesting effect of asymptotic freedom. Asymptotic freedom describes the fact that the strong coupling constant tends to zero for infinite momentum transfers or, equivalently, infinitely small distances.

On the other hand, free coloured objects have not been observed up to now. This experimental observation is called confinement and can be interpreted as follows: If two coloured objects are pulled apart from each other, the energy of the colour field between them is bundled into a flux tube and increases until it is converted into a new pair of coloured objects (one carrying the corresponding anti-colour of the other's colour). Altogether, these objects then form colourless hadrons[1].
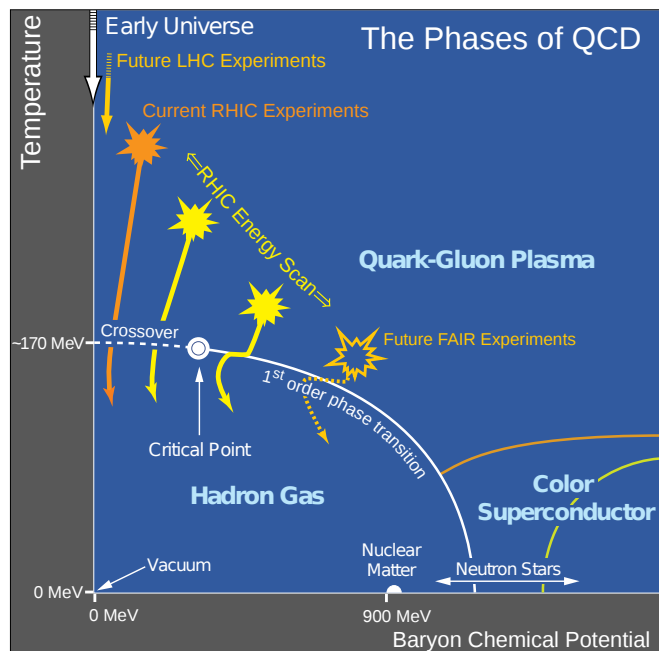
Figure 1.1.: QCD phase diagram with the temperature on the ordinate and the baryon chemical potential, which is directly connected to the baryon density, on the abscissa. Also shown are present and future experiments (yellow and orange arrows), that are designed to study the location and the kind of phase transition between QGP and hadron gas (figure adapted from [6]).

---

[1]There are 3 colours, red, green and blue, and the corresponding anti-colour. (Anti-)quarks carry one (anti-)colour and gluons colour and anti-colour. Combining (anti-)quarks of all 3 (anti-)colours gives a "white", i.e. a colourless, (anti-)baryon. The same is true for the combination of a quark with an anti-quark having the corresponding anti-colour to a meson.

QCD calculations [7, 8] have anticipated that the asymptotic freedom has an interesting consequence: At sufficiently high temperatures and/or net baryon densities, the confinement is repealed and the partons, i.e. the (anti-)quarks and gluons, can move freely. This new state of deconfined matter is called Quark-Gluon Plasma (QGP). Such a phase of matter is assumed to have existed about 10 μs after the Big Bang [1]. With the expansion of the universe, the matter cooled down and the partons became confined inside hadrons. Hence, today's matter is the result of a phase transition from the QGP to the hadronic phase.

The current knowledge and expectations are summarised in the phase diagram depicted in Fig. 1.1: Nuclear matter is located in the hadronic phase, while the core of neutron stars might reach the quark-gluon plasma phase for sufficiently high baryon densities. Current and future experiments (yellow and orange arrows) will search for the position of the phase boundary between hadron gas and quark-gluon plasma. These experiments will also look for the critical point, where the first order phase transition changes to a smooth crossover. The evolution of the early universe is illustrated by a white arrow at zero net baryon chemical potential. Note that this phase diagram is not the only possible one. In particular, the phase transition is not necessarily of first order.

In the laboratory, the only means to create and study a QGP are ultra-relativistic heavy-ion collisions. In the collision zone, the energy density becomes very high resulting in the production of a large number of partons. These partons undergo further collisions. If thermal equilibrium is (approximately) reached, observables like temperature, pressure, energy and entropy density can be defined. Their relation can be described by the equation of state.
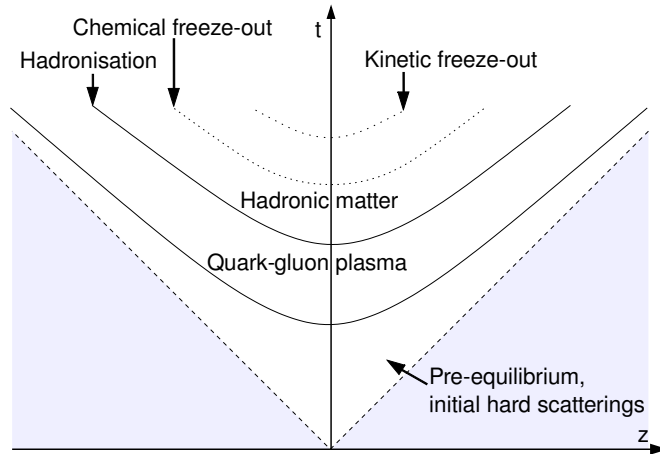
Figure 1.2.: Evolution of the fireball in heavy-ion collisions: After a pre-equilibrium phase, a QGP is formed for sufficiently high densities and temperatures. When the temperature drops below the critical temperature due to the expansion of the fireball, a phase transition to hadronic matter takes place, followed by the chemical and the kinetic freeze-out (figure based on [9]).

1. Introduction

The evolution of the fireball created in heavy-ion collisions is illustrated in Fig. 1.2: After a pre-equilibrium phase, potentially with hard scatterings, the thermalisation of partons to a QGP occurs for sufficiently high collision energies. The fireball expands and, thus, cools down. When the temperature drops below the critical temperature, hadrons are formed. The mean free path length increases with further expansion and, at some point, the inelastic scattering stops and fixes the hadron abundances. This point is called chemical freeze-out. It is followed by the kinetic freeze-out, which occurs after further expansion, when the elastic scattering becomes negligible and the momentum distributions of the particles are fixed.

The QGP created in heavy-ion collisions is only short-lived. The only way to study its properties is the measurement of the trajectories and species of the emerging particles. This allows to determine e.g. momentum distributions, particle flow and the abundance of species. It must be taken into account that the confined partons of the initial state themselves cannot be directly observed. Instead, the properties of the medium can only be inferred from the emerging colourless hadrons, leptons and photons. Both, leptons and photons, do not participate in the strong interaction and offer a direct study of the initial system. Yet, they must be separated from the particles created at later evolution stages, in which e.g. decays occur.

Lattice QCD is a theoretical approach to figure out the properties of a QGP, e.g. the determination of the type and location of a phase transition. It relies on numerical QCD calculations on discrete space-time points. Once experimental results have been obtained, they can be used as input for lattice QCD. From the results predictions for other observables can be obtained and compared to other experimental results. Unfortunately, lattice QCD is very limited by the currently available computing power.

To obtain experimental results for the properties of the QGP, suitable probes are needed. In general, it is useful to examine and compare these probes for different types of collisions: heavy-ion collisions, such as lead-lead, and *pp* collisions. In the first case and for sufficiently high energy, a QGP is likely to be created, while in the latter case, it is not. Indeed, this strategy with different types of collisions is pursued in case of the LHC and, in particular, by ALICE. To investigate cold nuclear matter effects [10], proton-lead collisions are planned for 2012 [11].

Some candidates for suitable QGP probes are listed and explained shortly in the following.

Measurement of quarkonia: Such vector-resonances are, for instance, the J/ψ and the Υ, consisting of a bound state of a quark and an anti-quark (c and c̄ in case of the J/ψ). For simplicity, only the J/ψ will be considered in the following, but similar arguments hold for the Υ.

If a QGP is formed, the colour charges in such a medium are screened. This

is similar to the Debye screening in electrodynamics. The screening can be parametrised by the Debye radius r_{D}. If r_{D} is smaller than the binding radius of quarkonium (which is different for J/ψ and Υ), the quarks are no longer bound, but move freely and independently in the plasma. At the time of hadronisation, they will be bound again with other (anti-)quarks. The probability to form a J/ψ again is then proportional to the number of created c (anti-)quarks squared. The J/ψ yield can be compared to the case without QGP.

Yet, the quarkonia have a relatively short mean lifetime, such that their decay products need to be measured to reconstruct the mother particle. The decay to $e^+ + e^-$ or to $\mu^+ + \mu^-$ suits this purpose well, since the daughter leptons can traverse the medium without distortion due to hadronic interactions (cf. discussion for di-leptons in the following).

Di-leptons: Leptons do not participate in the strong interaction. Consequently, their mean free path length in the medium is large compared to the dimensions of the medium and the probability of collisions is small. So, leptons are very likely to traverse the medium without interaction. Since di-leptons are produced in all stages of the evolution by different mechanisms, they can be used to study the whole history of the collision.

Direct photons: These are all photons not originating from hadronic decays. They are either produced directly in the initial hard scattering process (prompt photons), e.g. via quark-anti-quark annihilation, or during a thermally equilibrated phase (thermal photons). They only participate in the electromagnetic interaction and, therefore, have similar benefits as di-leptons.

Jets: Hard scatterings in the initial phase of the collision (see Fig. 1.2) can result in back-to-back jets with balanced transverse energy. The jets then interact with the medium and loose energy in it due to the radiation of soft gluons. This energy reduction and any other modification of the jet due to interactions with the medium is called jet quenching [12, 13]. The larger the distance the jet passes through the medium, the higher the energy loss will be. So, depending on the position of the hard scattering, the back-to-back jets can have different energies, especially, if the jets are produced in vicinity of the fireball's border.

Except for jets, the above listed observables require a reliable electron or muon identification. The same is true for the measurement of open charm and beauty, i.e. particles with non-vanishing charm or beauty quantum number, via their semi-leptonic decay channels.

With respect to the high event rates, the need of a trigger on events containing such rare probes was planned. A suitable trigger needs to properly identify the muons or electrons online. A trigger on jets is also very beneficial.

1.3. The Upsilon

A very interesting particle is the Υ meson. It is a $b\bar{b}$ bound state with spin 1. A selection of some observed energy states is listed in Tab. 1.3. In general, the $b\bar{b}$ bound states are called "bottomonium family". Analogously, the "charmonium family" labels the $c\bar{c}$ bound states. The J/ψ is an example for such a charmonium state.

According to Tab. 1.3, the Υ is a heavy particle with mass around 10 GeV/c^2. It is noteworthy that the three lower Υ states have total decay widths in the order of 10 keV, whereas the widths of the higher states lie in the 10 MeV regime. The reason for that can be found by considering the masses of the states and of the B-mesons (B^0 and $B^\pm$). The latter masses are approximately 5279 MeV/c^2 [2]. Energy conservation implies that only the Υ(4S) and higher states can decay to two B-mesons. Other strong decays are highly suppressed by the OZI[2] rule (cf. [14, 15]), which accounts for the smaller total width of these states. This rule also explains why the relative branching ratios for di-electron decays are not too small for the lower states, even if these are electromagnetic and not strong decays.

	Υ(1S)	Υ(2S)	Υ(3S)
Mass [MeV/c^2]	9460.30 ± 0.26	10023.26 ± 0.31	10355.2 ± 0.5
Γ_{tot} [keV]	54.02 ± 1.25	31.98 ± 2.63	20.32 ± 1.85
$\Gamma_{e^+e^-}$ [keV]	1.340 ± 0.018	0.612 ± 0.011	0.443 ± 0.008
$\mathfrak{B}(\Upsilon \to e^+ + e^-)$ [%]	2.48 ± 0.07	1.91 ± 0.16	*seen*

	Υ(4S)	Υ(10860)	Υ(11020)
Mass [MeV/c^2]	10579.4 ± 1.2	10876 ± 11	11019 ± 8
Γ_{tot} [MeV]	20.5 ± 2.5	55 ± 28	79 ± 16
$\Gamma_{e^+e^-}$ [keV]	0.272 ± 0.029	0.31 ± 0.07	0.130 ± 0.030
$\mathfrak{B}(\Upsilon \to e^+ + e^-)$ [10^{-6}]	15.7 ± 0.8	5.6 ± 3.1	1.6 ± 0.5

Table 1.3.: Upsilon states $\Upsilon(= b\bar{b})$ [2]. Stated are the mass, the total width, the partial width and the corresponding branching ratio for the di-electron decay for each state. Note that the total width is given in keV in the upper row, but in MeV in the lower one. Similarly, the branching ratio is stated in % in the upper and in units of 10^{-6} in the lower row.

To acquire a qualitative understanding of the mentioned effects, the decay $\Upsilon(1S) \to e^+ + e^-$ can be considered. Its lowest order Feynman diagram is shown in Fig. 1.3. The figure illustrates the decay via one virtual photon. It must be kept in mind that the quarks are not free, but bound by strong interaction. This

---

[2]This rule was independently proposed by Susumu **O**kubo, George **Z**weig and Jugoro **I**izuka in the 1960s. It states that any strong process with a Feynman Diagram that can be split in two by cutting only internal gluon lines will be suppressed.
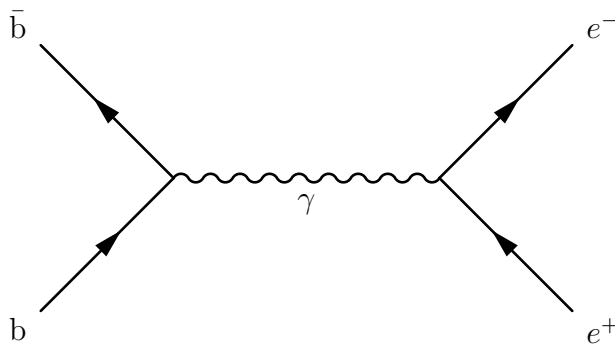
Figure 1.3.: Lowest order Feynman diagram for the decay $\Upsilon \to e^+ + e^-$. The strong binding of the quarks is not taken into account.

can be described phenomenologically by introducing a form factor, but will be neglected here for simplicity. The rather large value of the branching ratio of the electromagnetic decay compared to that of strong decays (e.g. to pions) and the small total width can be explained analogously to the decay of a J/ψ: Due to the conservation of quantum numbers, especially colour, the decay cannot be mediated by only 1 virtual gluon. The decay through 2 gluons in a colour-neutral state is forbidden due to C-parity conservation. Indeed, it can be shown (cf. [15, 16]) that at least 3 gluons are necessary. As a result, the strong decay is of higher order than the electromagnetic decay. Taking into account the larger value of the strong coupling constant compared to the electromagnetic one, both processes are in the same order of magnitude for the transition probability.

But why is the Υ interesting? Even nowadays there is only a poor understanding of hadro-production in nuclear collisions. Although there is much effort to investigate the J/ψ, which is produced much more abundantly in collisions than the Υ and forms a strongly bound state as well, there is one crucial advantage for the Υ: Due to the heavier mass of the b-quarks, theoretical calculations, like cross sections for the Υ production in proton-proton collisions, are more robust for the bottomonium than for the charmonium family. One reason is that heavier particles have lower velocities, which allows for neglecting relativistic effects.

It was mentioned in section 1.2 that the QGP, produced in Pb–Pb collisions, screens the colour charges, which can lead to the melting of quarkonium states. This melting affects the charmonium states (J/ψ, $\psi(2S)$, χ_c, etc.) as well as the bottomonium states ($\Upsilon(nS)$, χ_b, etc. — cf. [17]). Due to different radii and, thus, different binding energies the melting temperature will be different for those states (cf. [18]). So, comparing the yields of all these states in Pb–Pb collisions with those in *pp* collisions results in a melting pattern. From this pattern the critical temperature T_{crit} can be inferred, at which the phase transition between hadronic matter and the QGP takes place. Thus, besides exploring charmonium states, the investigation of bottomonium states can help to understand the QGP

and to provide valuable information to constrain QGP models [19].

For such an investigation, the involved quarkonia need to be reconstructed by measuring the daughters. With respect to this requirement there is still another aspect that makes especially the Υ attractive: As a consequence of its heavy mass, the daughters, e.g. electron and positron in the di-electron channel, acquire high momenta from the decay by 4-momentum conservation. These high momenta might lead to the naive assumption that the decay will still be approximately back-to-back, when the decay is boosted, i.e. the Υ decays during flight. Two leptons, namely electron and positron, flying apart back-to-back should be easy to detect, thus, providing a simple and significant event signature.

This train of thought will be picked up again in chapter 3, where such a signature is used to study a level 0 topology trigger.

1.4. The Large Hadron Collider
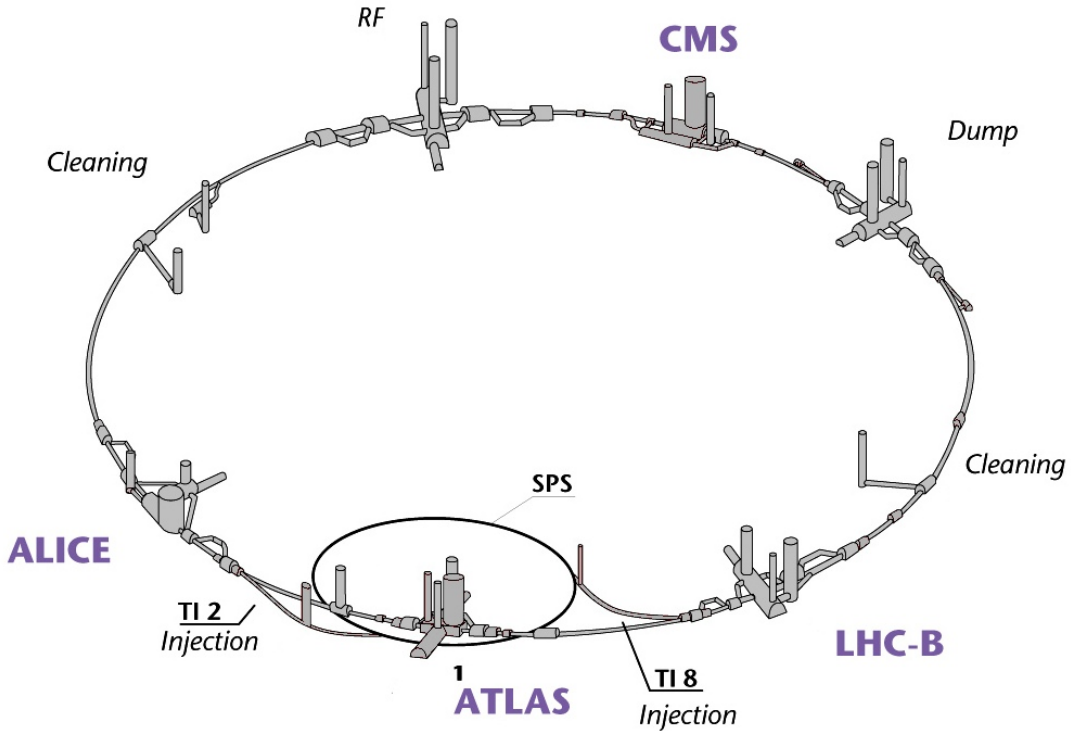
Figure 1.4.: Schematic view of the Large Hadron Collider and the four large experiments: ATLAS, ALICE, CMS and LHCb. The figure also shows the Super Proton Synchrotron (SPS), which lies at the end of a chain of accelerators and injects particles into the Large Hadron Collider (figure adapted from [20]).

The Large Hadron Collider (LHC) is currently the world's highest energy particle accelerator that has been designed to collide either protons or heavy-ions.

It has been installed at CERN[3], near Geneva, in the tunnel of its predecessor LEP (**L**arge **E**lectron-**P**ositron Collider). The LHC has a circumference of about 27 km and is located about 100 m below the surface. The nominal beam energy is 7 TeV for protons and 2.75 TeV/nucleon for lead-ions [21]. The design luminosity is $\mathcal{L}_{pp} = 10^{34}$ cm^{-2}s^{-1} in proton-proton and $\mathcal{L}_{\mathrm{PbPb}} = 10^{27}$ cm^{-2}s^{-1} in Pb–Pb collisions, respectively.

In September 2008, the beam was successfully steered around the accelerator for the first time. Unfortunately, a few days later, a faulty electrical connection between two bending magnets caused damage of parts of the accelerator [22]. The accelerator needed to be repaired and, finally, in November 2009, the first particle collisions after the incident were reported by all four detectors.

The LHC and its four experiments[4] are shown in Fig. 1.4. The particle beams are brought to collision at four interaction points, where the experiments are located.

The **ATLAS** (**A T**oroidal **L**HC **A**pparatu**s**) experiment has been optimised for the search of the Higgs boson, dark matter candidates and physics beyond the Standard Model (e.g. extra dimensions or supersymmetric particles).

The **CMS** (**C**ompact **M**uon **S**olenoid) experiment pursues the same scientific goals as the ATLAS experiment. However, different technical solutions and a different design of the magnet system are used for this purpose. This allows for mutual verification of the results acquired by both experiments.

ALICE (**A L**arge **I**on **C**ollider **E**xperiment) is the only experiment at the LHC that was especially designed to operate in heavy-ion mode — but proton-proton collisions are measured as well. The experiment studies the Quark-Gluon Plasma (QGP) that is created in Pb–Pb collisions. This state is believed to have existed shortly after the Big Bang (cf. section 1.2). With this study, the experiment also investigates the QCD confinement. Compared to CMS and ATLAS, ALICE is designed for smaller events rates, but for the higher multiplicities of heavy-ion collisions. Due to a lower magnetic field, ALICE is capable to measure and identify charged particles with lower transverse momenta than the other experiments.

The **LHCb** (**L**arge **H**adron **C**ollider **b**eauty) experiment searches for the origin of the observed matter-anti-matter asymmetry in the universe by studying the CP-violation in B-meson decays.

---

[3]Originally **C**onseil **E**uropéen pour la **R**echerche **N**ucléaire. The name CERN was retained, but the title of the organisation was changed to *European Organization for Nuclear Research*.

[4]In addition, there are 3 smaller experiments at LHC, TOTEM, LHCf and MoEDAL, which will not be described here.

1.5. The ALICE Detector

The ALICE (**A** **L**arge **I**on **C**ollider **E**xperiment) detector has been optimised for heavy-ion collisions in order to study the properties of the QGP. Yet, ALICE also analyses proton-proton and light-ion collisions for calibration and comparison purposes.

The experiment has a total weight of 10,000 t and its overall dimensions are 16x16x26 m^3 [23]. It can be divided into two parts: the central barrel, which covers the full azimuthal angle and a pseudo-rapidity of $|\eta| \leq 0.9^\dagger$, and the forward muon spectrometer at $-4.0 \leq \eta \leq -2.5^\ddagger$. A schematic view of the detector and its constituents is shown in Fig. 1.5.
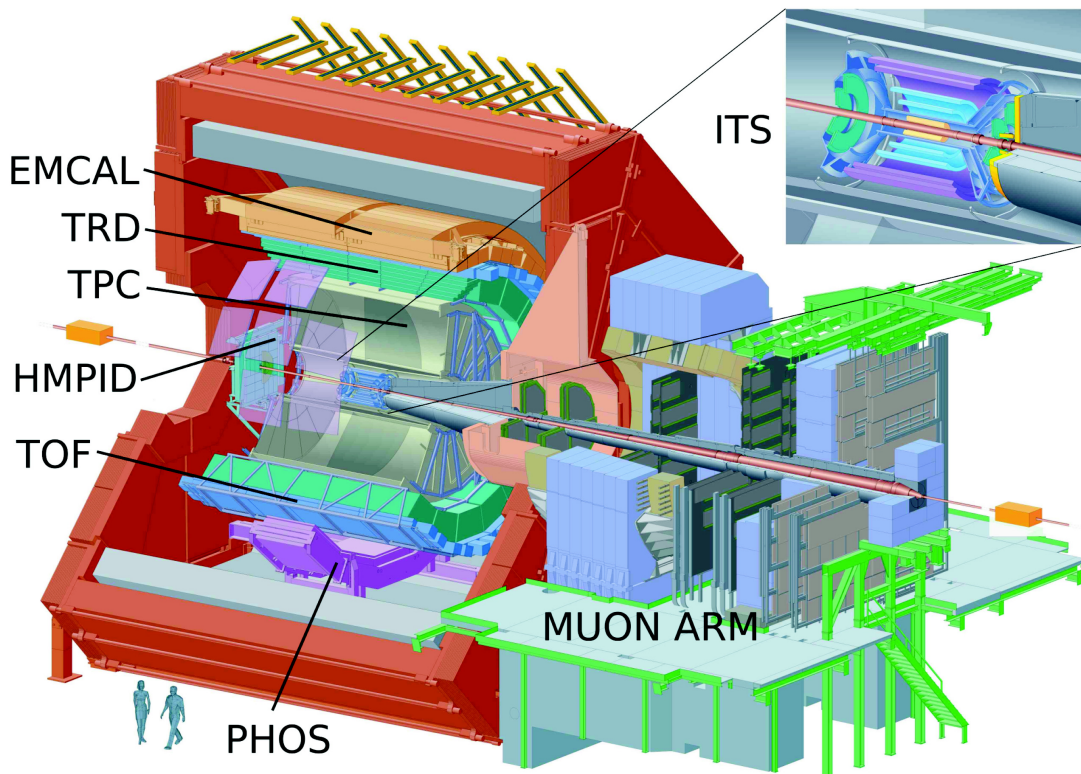
Figure 1.5.: Layout of the ALICE detector system. The detector can be divided into 2 parts: the central barrel and the muon arm in forward direction. The central barrel is embedded in the L3 solenoid and consists of several subdetectors (figure adapted from [24]).

Combining the Particle Identification (PID) power of all detectors, ALICE is capable of identifying particles in a wide momentum range (see Fig. 1.6).

---

†This corresponds to a polar angle coverage from 45° to 135°.

‡This is equivalent to a polar angle of 171° to 178°.
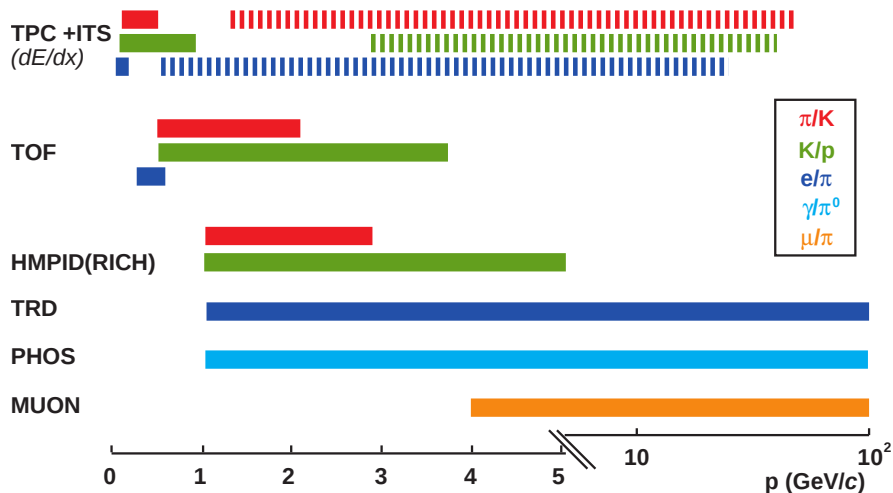
Figure 1.6.: Overview of the particle identification capabilities of the ALICE detector system. The values of this plot are based on [25]. The broken bars indicate momentum regions, in which only a limited PID on statistical basis can be performed by the corresponding detectors, such that this information can only serve to improve the PID of detectors that are more reliable in this momentum region. Taking all detectors together, ALICE allows to identify particles in a wide momentum range [26].

The individual detectors except for the TRD will be described shortly in the following, whereas a detailed description of the TRD follows in chapter 2. A comprehensive description of all detectors with references to the corresponding design reports is given in [23].

1.5.1. The Central Barrel

The central barrel is located inside the L3 solenoid, which provides a magnetic field of up to 0.5 T. The detector has an onion shell structure. Moving from the collision vertex radially to the outside, the produced particles traverse the following detectors: the Inner Tracking System (ITS), the Time Projection Chamber (TPC), the Transition Radiation Detector (TRD) and the Time Of Flight (TOF) detector. Further detectors at large radii are the High Momentum Particle Identification (HMPID) detector, the Photon Spectrometer (PHOS) and the Electromagnetic Calorimeter (EMCal). All detectors, except for HMPID, PHOS and EMCal, which have a smaller overall acceptance, cover the full azimuthal angle.

The global central barrel tracking is based on the information from ITS, TPC and TRD. Thereby, the bending of charged particle tracks in the magnetic field makes a momentum measurement possible. The central barrel's PID information is mainly obtained from the dE/dx measurement in the TPC and in the ITS, the TOF data and the measurement of dE/dx and transition radiation in the TRD.

The Inner Tracking System

The main purpose of the Inner Tracking System (ITS) [27] is the localisation of the primary vertex with a resolution of better than 100 μm and to reconstruct the secondary vertices of short-lived particles. It is also capable of tracking and identifying particles with momenta below 100 MeV/c, which will not reach the TPC.

The ITS consists of 6 layers: The two innermost layers are Silicon Pixel Detectors (SPD), followed by two layers of Silicon Drift Detectors (SDD) and completed by two outermost layers of Silicon Strip Detectors (SSD).

The Time Projection Chamber

The Time Projection Chamber (TPC) [28] plays the central role for the tracking in the central barrel. It has been designed to reconstruct up to 20,000 tracks of charged particles per event. Another crucial purpose is the identification of particles, which can be achieved by comparing the particles' dE/dx for a certain momentum with the Bethe-Bloch curves of possible particle species. An example is shown in Fig. 1.7. It can be clearly seen that the "bands" around the Bethe-Bloch curves of electrons and pions start to overlap at momenta above 3 GeV/c. Hence, other detectors like the TRD must be included to achieve a reasonable e/π-separation in this region.
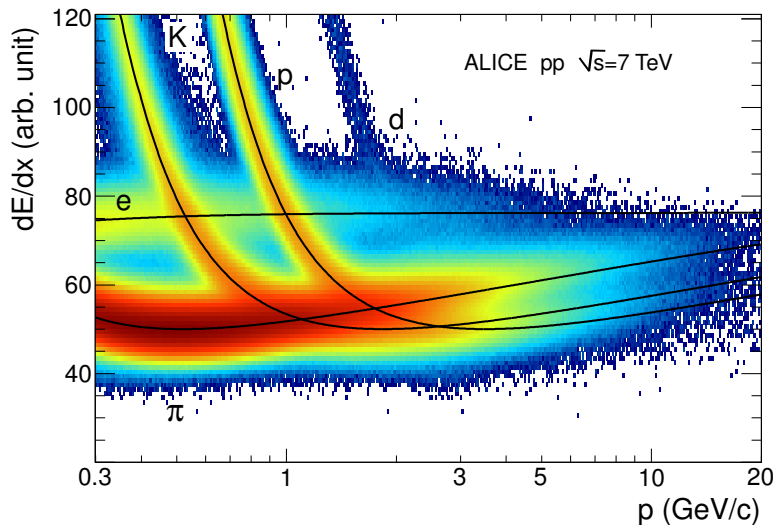
Figure 1.7.: Particle identification with the ALICE TPC via dE/dx: The energy deposit for different species is shown as a function of momentum for proton-proton collisions at a centre of mass energy of $\sqrt{s} = 7$ TeV. The black lines are a parametrisation of the Bethe-Bloch curve. Above 3 GeV/c the electron and pion bands around these curves start to overlap. This means that e/π-separation with TPC dE/dx alone is only limited possible (figure adapted from [29]).

The Time Of Flight Detector

The Time Of Flight (TOF) detector [30] provides very precise time of flight measurements. This renders K/p separation possible and, in general, allows for PID in the momentum range between 0.5 GeV/c and 2.5 GeV/c. Furthermore, the TOF detector can be used as input to the TRD pretrigger.

The modules of the detector are Multi-gap Resistive Plate Chambers (MRPC) and arranged in 18 supermodules.

The other Central Barrel Detectors

Other detectors in the central barrel are the High Momentum Particle Identification (HMPID) detector, the Photon Spectrometer (PHOS) and the Electromagnetic Calorimeter (EMCal).

The HMPID detector is a Ring Imaging Cherenkov Detector (RICH), that is used for hadron identification up to high momenta [31].

PHOS has been designed for the measurement of low-p_t direct photons and for the study of jet quenching via high-p_t π^0 and γ-jet correlations [32]. PHOS also contributes to the trigger, e.g. a trigger on high-p_t photons. It is an electromagnetic calorimeter made of lead-tungstate (PbWO$_4$) crystals.

Finally, EMCal [33] improves the jet quenching measurements and the jet energy resolution. It is also capable of measuring high-p_t photons, neutral hadrons and electrons. In addition, EMCal allows for a fast trigger on high-energy jets. EMCal has been designed as a layered Pb-scintillator sampling calorimeter.

1.5.2. The Muon Spectrometer

The muon spectrometer consists of absorber plates, tracking and trigger chambers and has its own dipole magnet with a nominal field of 0.7 T [34]. The spectrometer is used to measure the spectrum of the ψ and Υ families, as well as the one of the ϕ meson via their $\mu^+\mu^-$ decay channels. Besides, the production of open charm and beauty is studied. The muon arm also provides a trigger on high-p_t (di-)muons.

1.5.3. The Trigger and Forward Detectors

There is a set of forward detectors which are located close to the beam pipe: the Zero Degree Calorimeter (ZDC), the Photon Multiplicity Detector (PMD), the Forward Multiplicity Detector (FMD), the V0 detector and the T0 detector. These detectors allow for fast global event characterisation or for triggering [35].

An additional special purpose is served by the V0 and the T0 detector: The data of either of them can be used as input for the TRD pretrigger system.

Finally, the ALICE Cosmic Ray Detector (ACORDE) is mounted on top of the L3 magnet and can be used to trigger on cosmic rays [36]. It consists of an array of plastic scintillators.

Note that none of these detectors is shown explicitly in Fig. 1.5 (p. 12).

1.6. The ALICE Trigger Strategy

At LHC luminosities, the interaction rate is much higher than the maximum possible rate of the Data Acquisition (DAQ). This introduces the need of a trigger system that decides online which events are to be measured and read out. The heart of this trigger system is the Central Trigger Processor (CTP), which issues the trigger decisions based on the input and configurable conditions. In order to reduce the dead times and to have a fast first response of the trigger system, ALICE uses a multi-level trigger scheme: The level 0 (L0) signal is designed to reach the detectors 1.2 μs after the interaction and the level 1 (L1) signal is designed for arriving after 6.5 μs [37]. The L0 signal is fast and not all detectors that contribute signals to the trigger might be able to send their input in time for L0. Therefore, the remaining fast inputs are collected by L1. Ultimately, there is the final level 2 (L2) trigger signal sent after about 88 μs, which includes a past-future protection (see below) [37].

The *L0* trigger steers the initial activation of the detectors and is issued by the CTP. The CTP gathers the output of fast detectors that are continuously active and checks for which trigger classes the conditions for the L0 input are fulfilled. One or more detector clusters are associated with each trigger class. If the L0 input conditions of a trigger class are fulfilled, the CTP sends the L0 trigger to the corresponding detectors. For these detectors, the L0 signal initiates the local event recording.

After any L0 trigger a subsequent *L1* trigger can be sent. In case of an L1 reject, the data acquisition for the event is aborted and the electronics needs to recover for some time before the next L0 trigger can be handled. Consequently, the time between L0 and L1 should be short, since no other L0 trigger can be issued in that time interval.

Finally, an accept at the *L2* trigger level initiates the data shipping to the DAQ, while an L2 reject causes that the measured data is discarded. The L2 trigger includes the past-future protection, which leads to the large time interval of about 88 μs. This time interval is determined by the TPC drift time. In addition, further trigger algorithms can be performed for the L2 trigger. The *past-future protection* has been invented to properly handle pileup. Pileup means that there are tracks from different collisions at the same time in the detector. Especially in Pb–Pb collisions this might lead to events with multiple collisions, such that it might not be possible to uniquely relate tracks to individual vertices. The single subdetectors have different time windows in which their data can be

reliably used to reconstruct tracks. These windows depend also on the type of collision (*pp* collisions or Pb–Pb collisions with different centralities). The past-future protection circuits can be used to flag events for which pileup has been detected (refer to [37] for details). After all, these flags contribute to the L2 decision.

Further sophisticated event selections are performed by the *High-Level Trigger (HLT)* to reduce the data rate to a feasible rate for mass storage. The HLT consists of a computer farm with up to 1000 multi-processor computers [23] and is directly located in the ALICE experimental area. The HLT is capable of handling input data streams of up to 25 GByte/s, as can be reached after trigger selection in central Pb–Pb collisions [37]. The data rate is reduced by event selections beyond the trigger selections performed so far, by performing partial readout and reconstruction of the events ("physics regions of interest", refer to [23] for further information) and by compressing the data without loss of physics information. The resulting output rate is about 1 GByte/s and can be handled by the DAQ.

1.7. The AliRoot Framework

AliRoot [38] is the official software framework for ALICE. It is based on ROOT [39] and uses AliEN to access the computing grid in order to cope with the huge amount of data that is produced every year. Fig. 1.8 presents a schematic view of the AliRoot framework. The purpose of AliRoot ranges from data simulation and event reconstruction over alignment and calibration of the detector to data analysis. It consists of individual modules, whereby each detector part provides its own module for simulation, reconstruction and analysis. All modules are controlled by the central module of AliRoot, STEER, which provides steering, interface classes and run management. In addition, AliRoot allows for using external software like event generators and transport packages.

The data processing in AliRoot is sketched in Fig. 1.9. Here, only a short overview of this topic is given. A detailed description can be found in [40]. The simulation side of the data processing starts with the simulation of primary collisions and the production of particles via event generators, like PYTHIA or HIJING (see [40] for a description). This is the *Monte Carlo* stage, where the full information of each particle (like momentum, charge, mother-daughter relationships etc.) is available. Next, transport packages like GEANT3 are used to transport the particles through the detector. In this step, the interactions of the particles with the detector and the energy deposition are calculated and stored in *hits*. Afterwards, the detector response is taken into account including the simulation of noise. The result of this stage is stored in *digits*. These contain the digitised signals of sensitive detector parts.
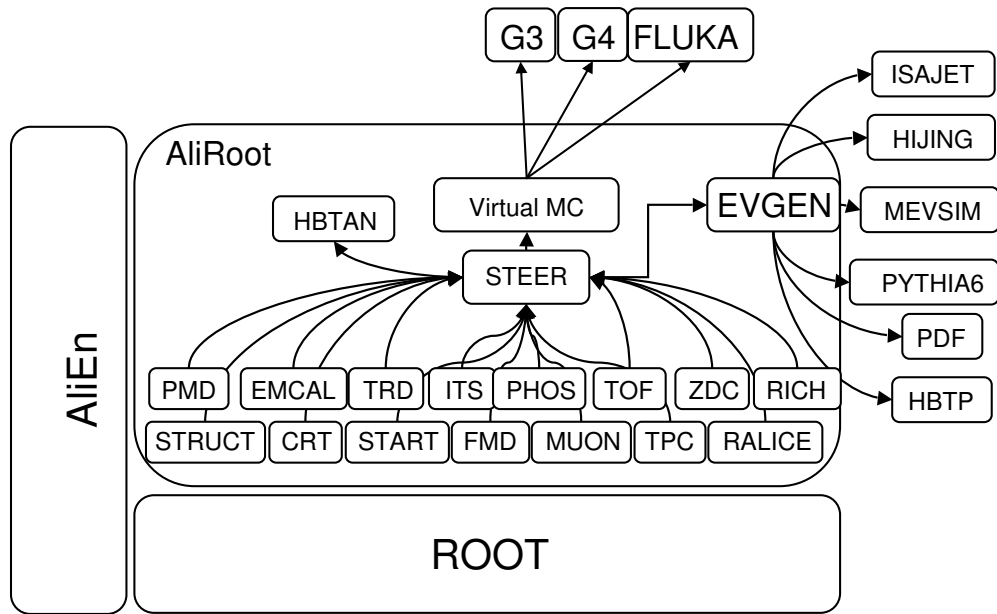
Figure 1.8.: Schematic view of the AliRoot framework [25].
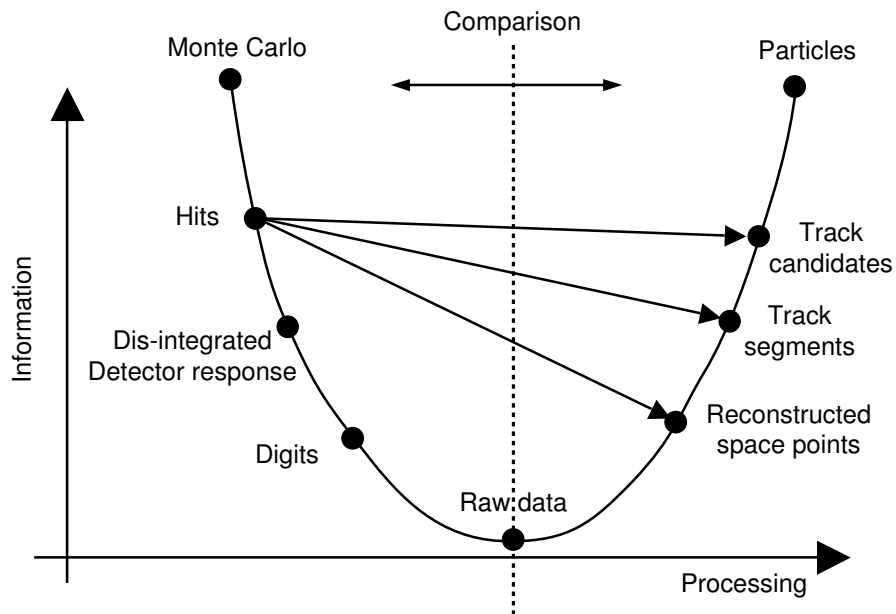
Figure 1.9.: Data processing in the AliRoot framework: comparison between simulation (left branch) and reconstruction (right branch). Raw data has minimum information, i.e. only the local detector response, but no global event information is available. The fully reconstructed events can be compared to the Monte Carlo information, both containing the maximum information [25].

In addition, a conversion to *raw data* is possible to test the actual data size and evaluate High-Level Trigger (HLT) algorithms. With each step, the information content decreases, reaching the minimum for the raw data. The raw data contains only the local detector response, but no global event information.

On the contrary, the information content grows on the reconstruction side of the data processing (right branch in Fig. 1.9). The reconstruction starts with the raw data, that can either stem from AliRoot simulations or from real data. At first, a local reconstruction of the clusters in each detector is performed. Thereby, a cluster is a set of adjacent digits in space and time that originate presumably from the same particle. Afterwards, the positions where the particles crossed the detector pads are estimated and stored as *reconstructed space points.* This information is finally used to calculate *track segments* and, afterwards, *track candidates.* The vertex and track reconstruction and the particle identification result in the final tracks at the *particles* stage. With a set of parameters describing the reconstructed trajectory, the tracks contain the maximum information that can be obtained from the raw data. The reconstruction output is stored in the Event Summary Data (ESD) and can be compared to the Monte Carlo data in case of simulated raw data.

2. The Transition Radiation Detector

Above 3 GeV/c the bands of pions and electrons in the TPC dE/dx spectrum start to overlap (see Fig. 1.7, p. 14). As a consequence, it is not possible to properly separate electrons from pions for such high momenta with the TPC alone. Fortunately, it is possible to make use of transition radiation, which allows for e/π-separation in this momentum region.

The first part of this chapter describes the operation principle and overall structure of the ALICE Transition Radiation Detector (TRD). In the second part, the TRD trigger is discussed.

2.1. Layout of the Readout Chambers and Principle of Operation

If a charged particle crosses the boundary between two media with different diffractive indices, the particle's electromagnetic field gets rearranged. It can be shown [41] that this can lead with a small probability to the emission of a photon. Such photons are called Transition Radiation (TR) and typically have energies of 10 keV for ultrarelativistic particles ($\gamma \gg 1$), i.e. they lie in the X-ray region. The emission probability strongly depends on the γ factor of the particle, $\gamma = \frac{E}{mc^2}$, and is only non-negligible for $\gamma \gtrsim 1000$. At the LHC, this condition is only satisfied for electrons with momenta around 1 GeV/c or larger. In particular, the probability is negligible for pions at momenta of a few GeV/c. Consequently, measuring TR allows for e/π-separation in a momentum region where other methods, like time of flight or pure TPC dE/dx measurements, are not suitable for this purpose. This is one of the reasons explaining the decision to integrate the Transition Radiation Detector (TRD) into the ALICE detector system.

The emission probability of a TR photon is only of the order of the electromagnetic coupling $\alpha_{em} \approx 1/137$. To increase this probability, a special radiator material is used for the ALICE TRD, which consists of many boundaries [42]. The radiator is made of a combination of polypropylene fibre mats and Rohacell foam. These materials have been chosen with respect to mechanical stability and the limited amount of space and material budget, since the TRD is an intermediate tracking device.

2. The Transition Radiation Detector

It is remarkable that the structure of this radiator leads to a saturation of the TR photon yield for high γ's. This effect can be observed for radiators with periodic layers as well, and can be explained by interference effects (a short overview is given in [43]).
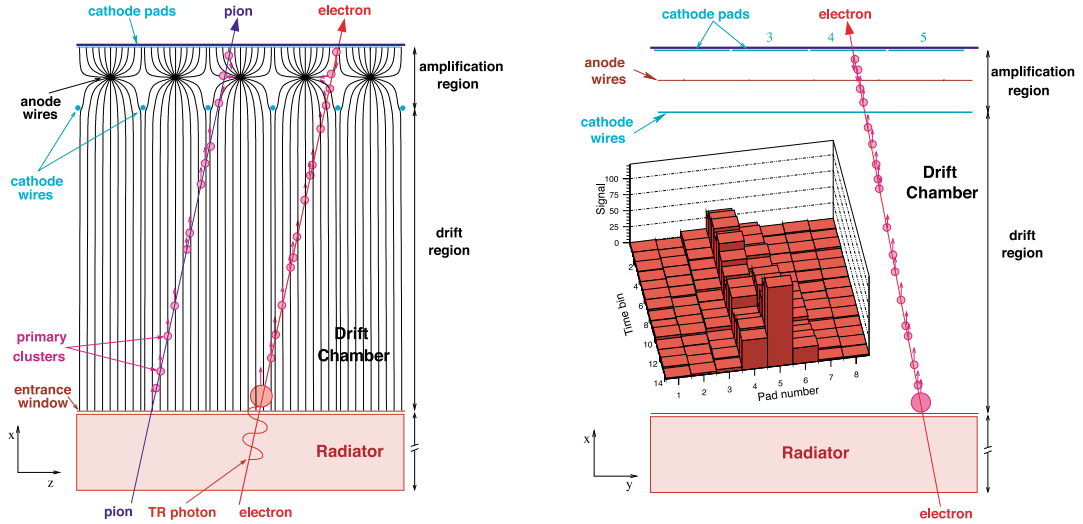
Figure 2.1.: The left panel shows an electron and a pion traversing a TRD chamber (x-z plane). The electrons and ions produced by ionisation near the trajectories drift along the electric field lines to the anode wires. In addition, the electron might produce a TR photon, when flying through the radiator. This photon can be absorbed by the gas in the drift volume. The right panel displays, besides the x-y plane of the chamber, the detected signal for different drift times [23].

The structure and the operation principle of the ALICE TRD chambers are depicted in Fig. 2.1. Each chamber consists of a radiator followed by the drift volume that ends in a Multi-Wire Proportional Chamber (MWPC). A voltage of about -2.1 kV is applied between the cathode wires at the end of the drift volume and the entrance window to form the electric field in the drift region — the resulting drift velocity is about 1.5 cm/μs [42]. The cathode wires are kept at ground potential. After the cathode wires, the amplification region starts with thin anode wires (diameter 20 μm) in the middle and a plane of cathode pads at the end. This is the MWPC part of the chamber. The anode wires are typically kept at a potential of about $+1.5$ kV, whereas the cathode pad plane is at ground potential.

Both regions, amplification and drift region, are filled with a gas mixture of 85% Xenon and 15% CO_2. Xenon is used to have a high absorption of X-ray photons: For 10 keV photons, the absorption length in Xenon is 1 cm [42], i.e. the TR photons are most likely absorbed close to the entrance window. This will result in a TR peak in the average pulse height of electrons and can be used for e/π-separation (cf. Fig. 2.4 (p. 25) and corresponding discussion in the text).

CO_2 has been chosen as quencher because it is non-flammable and cheap (further reasons are discussed in [42]).

Two purposes are served by the chambers: First, each chamber comprises a radiator as a source of TR. Second, the particle's trajectory is measured and TR detected. The principle of operation can be described as follows (see Fig. 2.1): The particle passes the radiator and potentially, in case of electrons, emits TR. It then traverses the drift chamber, where clusters of electrons are created by the ionisation of gas particles. TR photons are most likely absorbed at the beginning of the chamber and, thus, create additional clusters in this region. Due to the electric field in the drift region, the electrons drift to the cathode wires and the ions in the opposite direction. After passing the cathode wire plane and approaching the anode wires, the electrons experience the steep gradient of the electrical field close to the anode wires. This results in a dramatic increase of the electrons' kinetic energy, which, in turn, leads to an avalanche in the vicinity of the anode wires. While the electrons that are liberated by the avalanche are absorbed quickly by the anode wires, the generated heavier ions drift more than 1000 times more slowly away from them. On the cathode pads a signal is induced during the drift, which is amplified and shaped by the front end electronics.

Due to the rather large pad length ($z \approx 9$ cm [42]), clusters normally induce charge on only one pad in z direction. On the other hand, the pad width has been chosen to be relatively small ($y \approx 7$ mm), such that typically two or three adjacent pads in y direction are affected by the charge induction. The y resolution can be improved by making use of the charge distribution over adjacent pads. This can be achieved by using the Pad Response Function (PRF), which describes the fraction of the charge induced on adjacent pads by a point-like avalanche, and using the y dependence of the PRF to determine the avalanche's y position. For the chamber geometry of the ALICE TRD, the PRFs can be described by the Mathieson parametrisation [44].
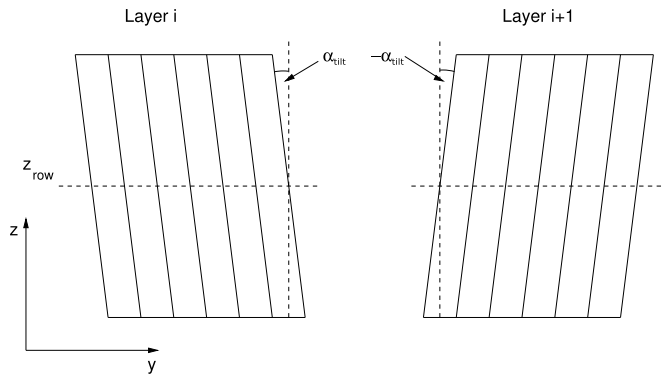
Figure 2.2.: Tilting of the TRD pads: To improve the z position resolution, the pads of neighbouring layers are tilted by an angle of $\alpha_{tilt} = 2°$ in opposite directions [42].

2. The Transition Radiation Detector

To achieve an improvement of the z resolution, the TRD pads are tilted by an angle α_{tilt} with respect to the z-axis and this tilt is performed in opposite directions in consecutive layers (see Fig. 2.2). The pad tilting allows for a z resolution better than the rather long pad length ($z \approx 9$ cm), but causes a slight decline of the y resolution.
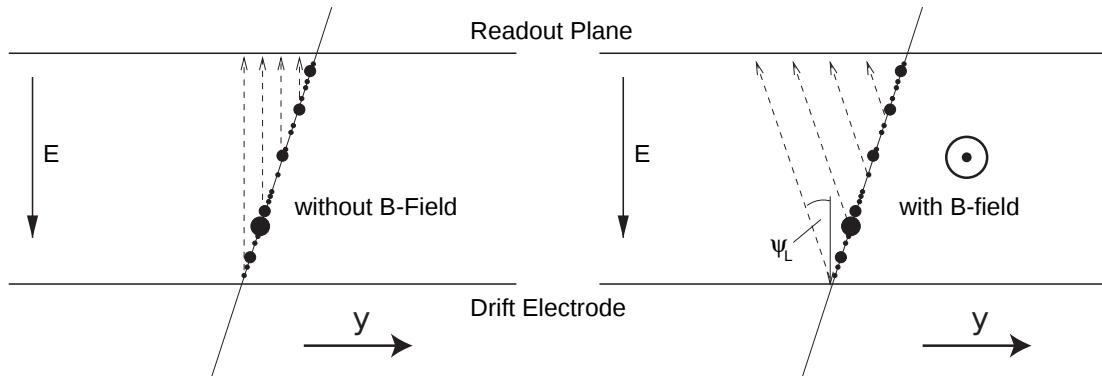
Figure 2.3.: Drift of the electron clusters without (left panel) and with (right panel) magnetic field. Without magnetic field, the electron clusters drift perpendicularly to the readout plane, while in the case with magnetic field, the drift direction changes by the Lorentz angle ψ_{L}. This leads to a deflection along the y direction [42].

Another effect, that must be taken into account, is the Lorentz angle ψ_{L} as shown in Fig. 2.3. The magnetic field causes a deflection of the drifting electrons that are produced by particles traversing the chamber. Both effects, pad tilting and Lorentz angle, must be taken into account for the reconstruction of the cluster position.

In summary, the trajectory of a particle is measured by reconstructing its clusters. The MWPC is used to determine the y coordinate and the pad row, that is the only available information about the z position, of each cluster. The drift time contains information about the x positions.

The design of the chambers and the use of a radiator leads to typical shapes of the pulse height versus time bins for different particle species. In Fig. 2.4, an example for the pulse height versus time bins averaged over many electrons and pions, respectively, is illustrated. The data points have been obtained from test beam measurements that used chambers with a different gas mixture and radiator than the current chambers [42]. Anyway, the basic trends are the same, so that the figure can be used to understand the shape as follows (also see Fig. 2.1): The particle traverses the chamber at a time of 0.3 μs creating clusters along the trajectory and, in case of electrons, there are possibly clusters created by a TR photon at the chamber entrance. When the first electron clusters reach the anode wires, avalanches and, thus, ions are created there. The ions lead to a steep increase of the signal. At first, clusters from both sides of the anode wires drift
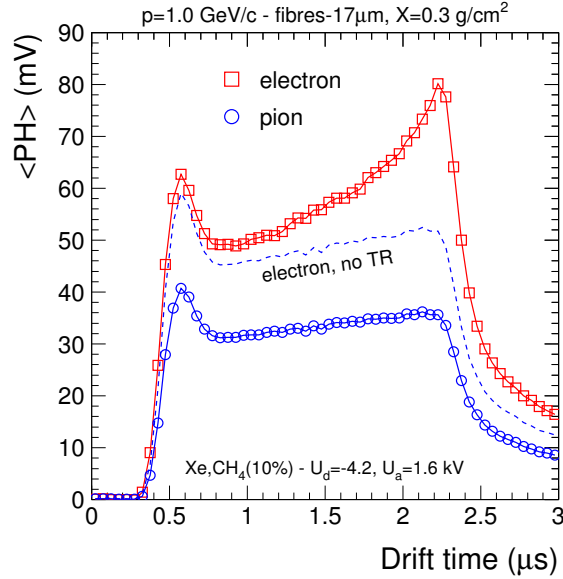
Figure 2.4.: Average pulse heights of electrons (red boxes) and pions (blue circles) as a function of the drift time. The dashed blue line represents the energy deposit by pure ionisation in case of electrons. The data points are from test beam measurements. Note that the gas mixture and the radiator are different for the currently used chambers, but this does not change the trending discussed in the text [42].

towards the wires. They create a high number of avalanches and, therefore, a high number of ions. After a few 100 ns, all clusters created in the amplification region have reached the anode wires. From now on, only clusters from one side, namely those created in the drift region, will arrive at the anode wires and contribute to the signal. This results in a decreasing signal compared to before, such that the signal shows an "amplification peak" at the beginning of the drift time. Shortly after, the signal becomes rather flat in case of pions (or electrons without TR). This "plateau" extends over the full drift time. The slight increase is caused by the slowly drifting ions created by the avalanches: The signal of newly created ions adds up with that of previously created ones which still have not reached the cathode plane. In case of electrons with emission of a TR photon, this photon produces clusters most likely close to the chamber entrance, i.e. at large drift times. These clusters cause a "TR peak" at the end of the drift time. Since the absorption length of the TR photon is about 1 cm for the used gas and the length of the drift region is 3 cm, most of the TR photons are absorbed at the entrance of the chamber, but there is a small probability to have some photons being absorbed not before reaching the anode wires. Hence, the amplitude of the average pulse height of electrons is increased at all times compared to the case without TR, but the most significant increase is observed at large drift times. It is also notable that the signal amplitude of pions is smaller than that of electrons due to the smaller dE/dx at such momenta (in Fig. 2.4, $p = 1$ GeV/c).

2.2. Detector Layout

The TRD is located between the TPC and the TOF detector. In radial direction, the TRD extends from a radius of 2.9 m to 3.7 m, while the length is about 7 m in beam direction. It covers a pseudo-rapidity of $|\eta| \leq 0.9$ and the full azimuthal angle [42]. The radial detector thickness is smaller than 0.25 radiation lengths [23].

The main purpose of the TRD is the e/π-separation at momenta in excess of 1 GeV/c, where other detectors are not or only limitedly suitable for this separation. Another purpose is related to the momentum measurement: The particles' momenta are calculated from the curvature of the measured trajectory in the magnetic field. Due to its position at a larger radius than the TPC, the TRD improves the resolution of the momentum measurement. Finally, the TRD is a fast tracker allowing for a level 1 trigger based on tracks with Particle Identification (PID) information.
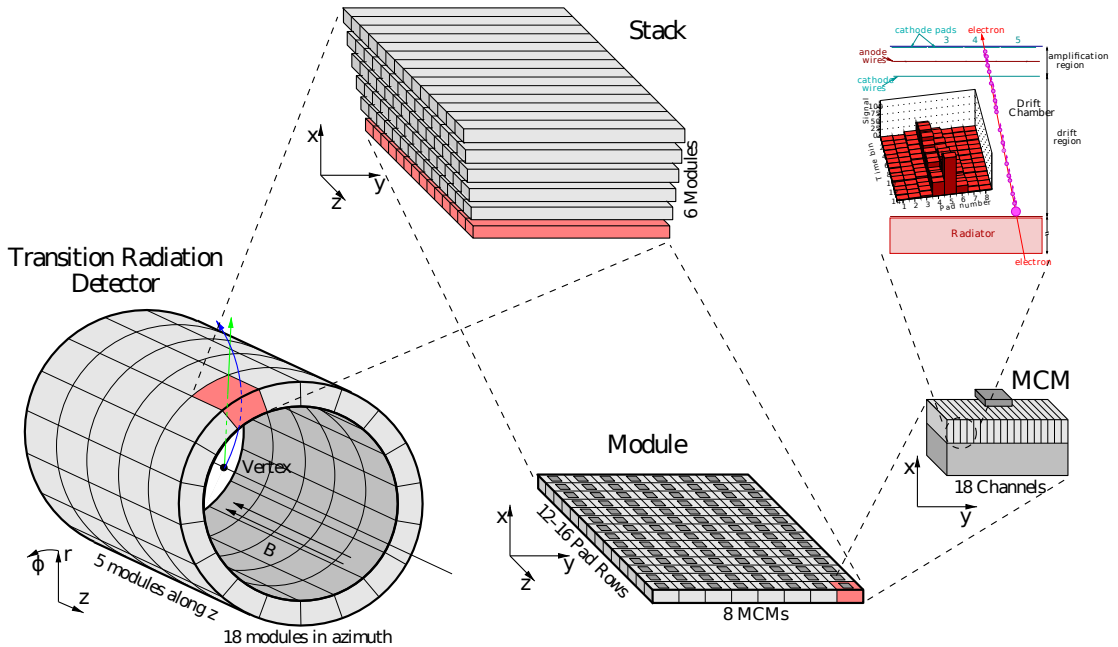
Figure 2.5.: Layout of the ALICE TRD. The TRD comprises 18 supermodules. Each supermodule is divided into 5 stacks, each containing 6 chambers. The readout pads of each chamber are arranged in columns and rows. Every Multi-Chip Module (MCM) is connected to 18 pads. The figure also shows the local coordinate system of a TRD supermodule, in this case depicted for a single stack [45].

The TRD has the common 18-fold azimuthal segmentation of the ALICE central barrel, each sector being filled with one Supermodule (SM). The overall detector structure is illustrated in Fig. 2.5. The SMs are divided along the z direction into 5 stacks, each containing 6 chambers arranged in layers. The

central stacks of the TRD SMs in front of three PHOS modules (sectors 13, 14 and 15) are not equipped with chambers because the material budget of the TRD would spoil the PHOS energy measurement. Hence, this gives a total number of 522 chambers and a gas volume of about 27 m^3 for the TRD. The readout plane of each chamber consists of 144 pad columns in azimuthal direction and 12-16 pad rows in z direction. The granularity has been chosen such that highest-multiplicity events result in an occupancy[1] of about 34%, which was found to be reconstructable [42].

The design goal is a pion suppression[2] by a factor 100 for particle momenta above 3 GeV/c and a momentum resolution of better than 5% at 5 GeV/c [42]. Such a good momentum resolution is necessary for a sharp momentum threshold and a smaller probability for fake tracks at trigger level.

2.3. The Front End Electronics

Since the induced signals, that have been described in section 2.1, are very small (order of 10^5 electrons), it is necessary to reduce the noise as much as possible. For this purpose, the front-end electronics, which reads out and processes the signal, is directly mounted on the backside of the detector modules. A set of 18 cathode pads in the same pad row is grouped and connected to one Multi-Chip Module (MCM) (cf. Fig. 2.5). Each MCM houses two chips: the Pre-Amplifier and Shaper (PASA) and the Tracklet Processor (TRAP). This chip combination allows for the calculation of tracklets. A tracklet is just a track segment fitted by a straight line within one TRD chamber.

The PASA collects the induced charge of each individual pad and, before shaping the signal, amplifies the signal in order to use the full input range of the subsequent Analogue to Digital Converters (ADC), which are part of the TRAP.
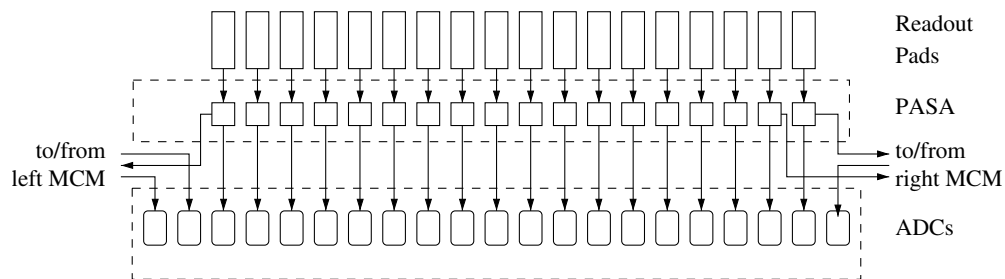
Figure 2.6.: Readout scheme of the pad plane [46].

---

[1]The occupancy is defined as the percentage of detector pixels in a time bin with a signal above threshold.

[2]The PID performance of the TRD will be discussed in detail in chapters 4 and 5.

Fig. 2.6 shows that all 18 readout pads of the MCM are used for the input to the PASA. The TRAP provides 21 input channels: 18 of them are just the output channels of the same MCM's PASA. Another 1 and 2 input channels are connected to the right and the left neighbouring MCM, respectively. This design is needed for the proper on-chip reconstruction of the tracklets. As a result, there are 21 ADCs per MCM/TRAP.
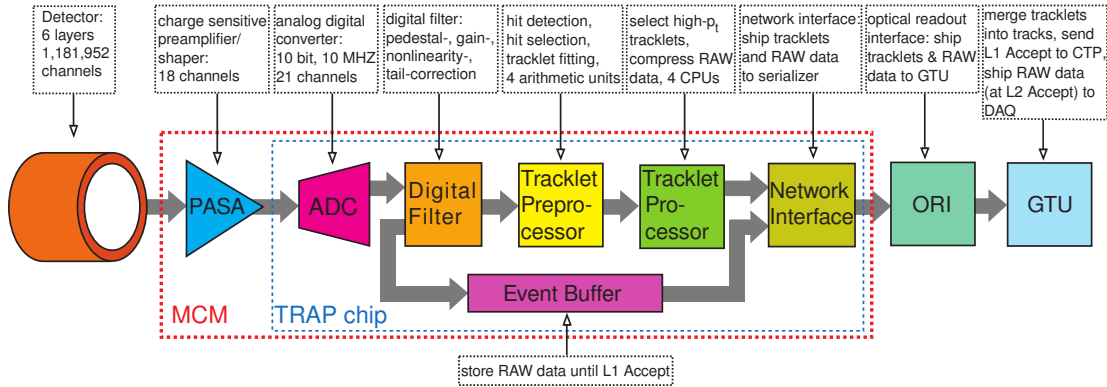
Figure 2.7.: Schematic overview of the TRD readout electronics (figure adapted from [23]).

Besides the ADCs, the TRAP consists of a set of digital filters, event buffers and processing units, see Fig. 2.7. The ADCs have a sampling rate of 10 MHz and a digitisation resolution of 10 bits [47]. The digitised signal is then sent through a series of filters. The filtering is required, since this information is the basis of the TRD trigger decision, e.g. the filters have a crucial effect on the cluster finding in the tracklet preprocessor (further details about the TRAP and the tracklet processing can be found in [47]). The filter stages are in the following order:

1. **Non-linearity correction**: This filter corrects the non-linearities introduced by the PASA. Currently, the filter is not used.

2. **Pedestal correction**: The pedestal filter determines and subtracts the individual baseline of each channel. Afterwards, a common baseline is added to avoid negative values for the signal. Such negative values can be introduced by later filter stages, e.g. by the tail cancellation filter.

3. **Gain correction**: The gas gain and electronic amplification differ channel by channel. The gain correction can be used to compensate these effects by scaling the input data within a range of $\pm 12\%$ and by using individual additives for each channel.

4. **Tail cancellation filter**: This filter stage suppresses the signal of the ion tails. The ions drift slowly and, therefore, induce a slowly decreasing signal in the pads. There is still a residual signal left, when the next ionisation

and amplification process takes place in the chamber. The tail cancellation filter is used to calculate and subtract this residual signal[3].

5. **Crosstalk suppression**: At design time of the electronics, it was taken into account that capacitive coupling of the readout pads might cause the problem that an induced charge in one pad also affects neighbouring pads. As a result, the signals of neighbouring pads would be correlated. The crosstalk filter allows for correcting this effect. Yet, it turned out during testing that this filter is not needed. Hence, it was decided not to use this filter in the experiment.

These filters need to be configured with appropriate parameters or can also be bypassed. The configuration is carried out by the Detector Control System (DCS) board of each chamber.

On the one hand, the filtered output is stored in an event buffer for further readout. On the other hand, the output is further processed by the tracklet preprocessor, that searches for hits[4] and determines some parameters of the tracklets. The tracklet preprocessor is capable to process up to 4 hits per time bin in parallel. If more hits are found, those with the highest deposited charge are selected.

The tracklet processor fits the found hits with a straight line and produces tracklets. The straight line assumption is a good approximation for the particle trajectory in the TRD, since the length of the drift volume is only 3 cm. For high-p_t particles, which the TRD trigger is mainly aiming for, the whole particle trajectory from the vertex to the TRD is a relatively straight line. Therefore, the tracklets are demanded to lie in two adjacent ADC-channels (but can also lie in only one in case of very high p_t), which can be understood by considering Fig. 2.5 (p. 26). Again, 4 tracklets can be calculated in parallel. In case of more tracklet candidates, those with the most hits are chosen. At this stage, information about the inclination of the tracklet and the tracklet's deposited charge is available. It can be used to identify high-p_t particles and tag possible electron candidates at trigger level.

Next, in the readout process, the resulting tracklets and, afterwards, the raw data are transferred serialised at half-chamber level. The serialisation is necessary to cope with the large number of TRAPs per chamber. This task is executed by the network interface used for inter-chip data transfer. Each half-chamber is equipped with an Optical Readout Interface (ORI), which transmits the data via an optical fibre to the Global Tracking Unit (GTU). The GTU processing will be discussed in section 2.5. The MCMs also support zero suppression, which allows

---

[3]Technically, the weighted sum of two exponentially decreasing signals with different lifetimes is used to determine the expected ion tail for each time bin. The effect of the tail cancellation on the signal will be studied in section 5.7. A detailed study for the tail cancellation used in offline analyses may be found in [43].

[4]Basically, a hit is a cluster with deposited charge exceeding a threshold (cf. appendix B).

to decrease the data volume. This means that the MCMs send only the raw data of those channels fulfilling some configurable conditions.

The huge amount of electronics dissipates a lot of heat. Thus, water-cooling is used, which is operated at under-pressure to avoid water leaking out of the cooling system.

2.4. The Detector Control System

Each chamber is equipped with a Detector Control System (DCS) board, which is responsible for the entire configuration, monitoring and the control of the electronics of this chamber. The DCS board hosts a Trigger Timing and Control (TTC) interface, which receives the central LHC clock signal. This signal is re-shaped and distributed to all MCMs of the chamber to synchronise their internal clocks. The configuration of filters and parameters for the tracklet calculation are steered by the DCS board, as well. Moreover, the DCS board monitors temperature and voltages of the MCMs and allows for switching off the electronics in case of too high temperatures or currents.

All states that are monitored by the DCS board and the states of the services (low and high-voltage, cooling, gas) are part of Finite State Machines (FSM) (more information on this topic can be found in [46]). These FSMs are controlled with a higher level control system realised in the program packages PVSS[5] and SMI++[6].

Similar systems exist for other subdetectors of ALICE. This makes it possible to operate the whole ALICE detector system from a single workplace, which is situated in the ALICE control room at LHC Point 2.

2.5. The Global Tracking Unit

This section will only give a short overview of the Global Tracking Unit (GTU) and its principle. A much more detailed description is given in [45, 50].

In the GTU, the tracklets of different layers that presumably belong to the same particle track are matched. Due to the very limited amount of time, the matching cannot be performed by checking all possible tracklet combinations for the expected (high) multiplicities. Instead, the tracklets of a stack are matched by propagating them to a common reference plane. Since for triggering with the TRD high-p_t particles are of interest, a straight line can be assumed for the trajectory in good approximation. Essentially, the matching is done by projecting the tracklets to a reference y-z plane[7] and by searching for windows in this plane

---

[5]**P**rozess**v**isualisierungs- und **S**teuerungs**s**ystem. This software has been developed by the Austrian company ETM [48].

[6]**S**tate **M**anagement **I**nterface. See [49] for more information.

[7]The local coordinate system of a TRD supermodule is shown in Fig. 2.5 (p. 26).

that contain more tracklets than a given threshold. The idea is that all tracklets of the same track will be concentrated in a small region of the projection plane. The currently used threshold is 4, such that the GTU accepts only tracks with at least 4 tracklets per track.

The GTU comprises an individual Tracklet Matching Unit (TMU) for each stack, i.e. 87 TMUs in total. The TMUs process the tracklets and calculate the tracks for the stack they are associated with. The results are sent to the corresponding Supermodule Unit (SMU), where the tracks of the single stacks are merged. Based on these tracks and some criteria, e.g. demanding n tracks to have a p_t exceeding a certain threshold, the SMU derives a level 1 trigger contribution, which is then sent to the central trigger processor. Finally, there is a buffer for the raw data from the supermodules. In case of a level 2 accept, the raw data is shipped to the data acquisition using the Detector Data Links (DDL).

There is still some subtlety that becomes important for the online PID discussed in chapter 4: It might happen that a MCM finds 2 tracklets in neighbouring channels with very similar positions and both tracklets can be matched. Another interesting case is that a tracklet lies in the shared channels of a MCM. These channels are read out by the two neighbouring MCMs (see Fig. 2.6, p. 27) and it happens that both MCMs find a corresponding tracklet with almost the same position. The GTU handles such cases by basically sorting the tracklet candidates ascending in the z position and, in case of equal z positions, also ascending in the y position and by selecting the first tracklets of the resulting list for matching.

Section 4.7 will discuss the relevance of this aspect with respect to PID performance.

2.6. The TRD Trigger

Besides allowing for a proper e/π-separation at momenta in excess of 1 GeV/c and improving the momentum resolution, the TRD fulfils a third task: It allows for fast online standalone tracking, which opens the possibility of a high-p_t trigger. It is possible to adjust the p_t thresholds and the number of particles that are demanded to have transverse momenta above these thresholds. Together with the good electron identification, it is possible to trigger on high-p_t electrons and jets.

2.6.1. Motivation

To study the Quark-Gluon Plasma (QGP), suitable probes are required (cf. section 1.2). High-p_t particles and jets are interesting in this context because they are mainly produced in the early stage of a heavy-ion collision. Furthermore, perturbative QCD can be used to calculate their production rates. In general,

particles that do not interact strongly can provide a relatively direct view of the reaction scenario, without distortion due to hadronic interactions.

There are several interesting processes with electrons and/or positrons in the final state, for example:

- $J/\psi, \Upsilon \rightarrow e^+ + e^-$

- electrons from photon conversion

- electrons from heavy-flavour hadron decays

- electrons from thermal di-lepton production

However, the cross sections of such electromagnetic and weak interactions are small compared to that of hadronic interactions. Typically, the probability of having such a rare probe in a collision is in the order of 10^{-5} [42]. Consequently, a dedicated trigger is required to enhance events that contain such interesting signals. It is also necessary to have a very powerful online electron identification, since the electrons are very rare compared to the huge environment mainly consisting of pions. All this makes the TRD a good candidate for such a dedicated trigger. Of course, other detectors are used as well to contribute to the final trigger decision.

2.6.2. The TRD Pretrigger System

The trigger strategy described in section 1.6 is more involved for the TRD: The TRAP chips are normally in sleep mode to safe power and to reduce noise. Therefore, a wake-up signal is needed prior to the sampling. However, the TRD receives the L0 trigger too late after the interaction to measure the full signal in the drift chambers. Hence, the pretrigger system has been developed. It is installed inside the L3 magnet and directly receives the data from fast detectors (like e.g. V0 or T0) contributing to the L0 trigger, without detour to the CTP. If the input fulfils the trigger conditions, the pretrigger issues a wake-up signal to the TRD. In the ideal case, the trigger conditions are the same for the pretrigger and the CTP, meaning that every L0 trigger is preceded by a pretrigger signal.

To sum up, the triggering for the TRD works as follows: The pretrigger wakes the electronics up and, with the arrival of the L0 trigger, the MCMs start the tracklet calculation. Then, the tracklets are sent to the GTU, where they are used to calculate the tracks. Based on the tracks, the GTU sends its L1 contribution to the CTP. If the TRD sees an L1 trigger from the CTP, the raw data is read out and sent to the GTU. From there it is shipped to the DAQ after an L2 accept.

2.6.3. Situation for Triggering

The situation for triggering is completely different to that of offline analysis. Offline, the complete information is available from all detectors, especially PID

information from TPC, TRD, TOF and other detectors like the HMPID. The whole reconstruction machinery, including sophisticated tracking algorithms, can be used to analyse the recorded data. In principle, there is an "arbitrary" amount of time available and latency does not play any role.

In contrast, the available data and time is very limited in the online case. For instance, all calculations for the L1 trigger contribution must be finished within a few microseconds. In case of the TRD, the L1 trigger contribution is purely based on the data that is recorded by the MCMs and further processed by the GTU, i.e. there is no information from other detectors, that can be used. Also, the PID is solely based on TRD information. How this information is exactly used to identify particles will be explained in detail in section 4.1.2.

At this point, it shall only be emphasized that it is not feasible to do advanced PID calculations in the MCMs for time reasons and with respect to the very limited processing power of a single MCM. Therefore, Look-Up Tables (LUT) are used to assign an electron likelihood to a tracklet (which is later used by the GTU to calculate the electron likelihood for a whole track). These LUTs contain the electron likelihood for different values of parameters. For example, the total charge deposit of a tracklet can be chosen as such a parameter. In this case, the MCMs determine the total charge deposit and obtain the electron likelihood from the corresponding entry in the LUT, which can be done quite fast.

In conclusion, this method allows for online PID that can be used for trigger decisions. Finally, the offline analysis can make use of the particle identification power of all detectors to analyse the triggered events.

3. Feasibility of an Υ Topology L0 Trigger with TOF

This chapter describes the concept of an Υ topology trigger from the TRD pre-trigger system based on data from the TOF detector. First, the demands and capabilities of such a dedicated trigger are discussed. Thereafter, an overview of the TOF detector with respect to the granularity seen by the TRD pretrigger is given. Subsequently, the topology trigger principle is described. Section 3.4 discusses the expectations based on simulations. To judge the feasibility of such a trigger, an estimation of the background is needed. This is the topic of section 3.5, which is followed by the presentation and discussion of the results. Since in all these sections the TOF detector's z segmentation is not used, section 3.6 investigates, whether the trigger performance could be improved with the additional z information.

At L0, the TOF detector has no information about the particle identities, such that all detected particles are considered for triggering at this level and not, for example, only electrons[1]. A simple topology trigger makes only sense for sufficiently low multiplicities of the considered particles. Therefore, only proton-proton collisions are investigated in this chapter, since the multiplicities are much lower than for lead-lead collisions.

According to [51], the $\Upsilon(1S)$ state is the most abundantly produced $\Upsilon(nS)$ state in proton-proton collisions and has the highest branching ratio for the di-muon decay of these states [2]. The branching ratio for the di-muon decay is approximately equal to the one for the di-electron decay. Therefore, the dominant part of all di-electrons from $\Upsilon(nS)$ decays stems from the $\Upsilon(1S)$ state, for which the simulations are carried out in section 3.4[2]. For electrons, a good Particle Identification (PID) can be achieved with the TRD (cf. chapter 4). Hence, the di-electron decay channel of the Υ is the interesting decay channel with respect to the topology trigger. The following sections will focus on this decay channel.

---

[1]This is different at L1. For example in case of the TRD, information of the electron ID is available at L1.

[2]As can be learnt from Tab. 1.3 (p. 8), the other $\Upsilon(nS)$ states have similar masses, so that similar results can be expected for these.

3.1. Motivation

Hitherto, the central detectors of ALICE have mainly used a trigger on minimum bias events and collected a lot of data with it. As the name "minimum bias" suggests, this trigger accepts almost every event. However, running the central detectors with this trigger another year would improve the error on already taken data only slightly. This is due to the fact that ALICE, in contrast to the other experiments, does not benefit from the increased luminosity of future runs, because the collision rate for ALICE is limited by the TPC. Therefore, it makes sense to develop new trigger strategies for future runs that allow to focus on special physical processes and to collect the corresponding data. Especially, this means to decrease the L1 rate or, in other words, to become more selective at L0. This will become very important for future runs with a higher interaction rate.

A suitable trigger is able to enrich the fraction of events containing special physical processes at L0. In turn, this allows for a more probable selection of such events at L1, which is very important with respect to the limited rate and dead times. Since the available information of an event is very limited for L0, it has to be looked for characteristic, but simple signatures of the interesting events.

As seen in section 1.3, the Υ is important for the study of the QGP. So, it would be useful to analyse as many Υ's as possible. Therefore, the goal is an Υ trigger for ALICE. Such a trigger can be realised by triggering on di-electrons at L1 with the TRD. As pointed out before, a good input sample is needed for L1, which could be achieved by a suitable pre-selection at L0.

It was shown in section 1.3 that the electrons and positrons from Υ decays have quite high momenta around 4.7 GeV/c. In the Υ's rest frame the decay is always back-to-back. The high momenta of the daughters can lead to the naive expectation that this decay will still be approximately back-to-back after the boost into the lab frame. But "back-to-back" is such a simple signature that can be recognised at L0 by the TOF detector. This makes the Υ di-electron decay a perfect candidate for an L0 topology trigger.

The power of such a dedicated L0 trigger can be seen from the following estimation of the number of detectable Υ's [52, 53]. First, the Υ production cross section and the branching ratio for a di-electron decay is required for this estimation (as stated above, the di-muon branching ratio can be used as an approximation). Lacking a trigger, ALICE has not performed any Υ measurements yet. Hence, 2010 CMS data is taken instead [51]:

$$\sigma_\Upsilon \equiv \sigma(pp \to \Upsilon(1S)X)\big|_{|y|<2} \cdot \mathfrak{B}(\Upsilon(1S) \to \mu^+\mu^-)$$
$$= (8.3 \pm (0.5)_{\text{stat.}} \pm (0.9)_{\text{lumi.}} \pm (1.0)_{\text{syst.}}) \text{ nb.}$$

These results have been obtained for proton-proton collisions at $\sqrt{s} = 7$ TeV, integrated over the rapidity range $|y| < 2.0$. However, the ALICE central barrel covers only the rapidity range $|y| < 0.9$. Assuming a flat distribution of the Υ's in y, the Υ production cross section and branching ratio is estimated to be half of the CMS value σ_Υ: $\sigma_\Upsilon^{\text{ALICE}} \approx \sigma_\Upsilon/2 \approx 4$ nb.

Only those Υ's in the rapidity range of the ALICE central barrel can be reconstructed for which both daughters (e^+ and e^-) are detected. To take into account the limited acceptance with respect to the daughters, a factor $\epsilon_{\text{acc}}^{\text{ALICE}}$ needs to be introduced. In simulations, the value is found to be $\epsilon_{\text{acc}}^{\text{ALICE}} \approx 0.4$ (see section 3.4).

In 2011, 10 of 18 TRD supermodules were installed. This implies a factor $\epsilon_{\text{acc}}^{\text{TRD}} = 10/18 \approx 0.5$ for the TRD acceptance.

In the following, the situation without dedicated trigger will be considered. Afterwards, this will be compared to the situation with a dedicated trigger. Without dedicated trigger, a rough estimation for the Υ recording rate is

$$R_\Upsilon \approx R_{\text{DAQ}} \cdot (\sigma_\Upsilon^{\text{ALICE}}/\sigma_{\text{MB}}),$$

where $\sigma_{\text{MB}} \approx 70$ mb is the Minimum Bias (MB) cross section for *pp* collisions at 7 TeV [54] and the typical rate of the Data Acquisition (DAQ) is $R_{\text{DAQ}} \approx 800$ Hz as found for the runs in 2010. The DAQ rate is the rate with which the events (in this case, the minimum bias events) are recorded and the ratio of the cross sections estimates the fraction of Υ decays in minimum bias events.

Finally, for one "good year" of data taking ($T = 10^7$ s), the number of *detectable* Υ's inside the TRD acceptance is:

$$N_{\text{NoDedicatedTrigger}} \approx T \cdot R_\Upsilon \cdot \epsilon_{\text{acc}}^{\text{ALICE}} \cdot \epsilon_{\text{acc}}^{\text{TRD}} \approx 90.$$

For a dedicated trigger, the optimistic case yields the following estimation: The maximal possible L1 input rate is $R_{\text{L1}}^{\max} = 100$ kHz. If this maximal rate could be achieved for the L0 output rate of the dedicated trigger, the corresponding maximal sampled luminosity would be $\mathfrak{L}_{\text{sampled}}^{\max} = R_{\text{L1}}^{\max}/\sigma_{\text{MB}}$. Assuming a trigger efficiency of $\epsilon_{\text{trigger}} = 0.5$, the number of *detectable* Υ's inside the TRD acceptance is then:

$$N_{\text{DedicatedTriggger}} \approx T \cdot \mathfrak{L}_{\text{sampled}}^{\max} \cdot \sigma_\Upsilon \cdot \epsilon_{\text{acc}}^{\text{ALICE}} \cdot \epsilon_{\text{acc}}^{\text{TRD}} \cdot \epsilon_{\text{trigger}} \approx 5700.$$

It must be emphasized that these numbers are only the *detectable* Υ's. No efficiencies for detection, reconstruction etc. have been taken into account yet. These would significantly decrease those numbers, both for the MB and the triggered sample.

Since a small latency for L0 is needed and the desired signature is based on topology, the TOF detector seems to be a good choice for the data source of the Υ L0 trigger.

3.2. The TOF Granularity at Trigger Level

To get an idea of how the TOF detector looks like from the TRD pretrigger (cf. section 2.6.2) point of view, Fig. 3.1 can be consulted. The TOF trigger consists of 4 Local Trigger Modules (LTM) for each of the 18 TOF Supermodules (SM), 2 LTMs in z direction and 2 in ϕ direction. So, the TOF trigger is segmented into 72 LTMs, each providing 8 channels [55, 56].
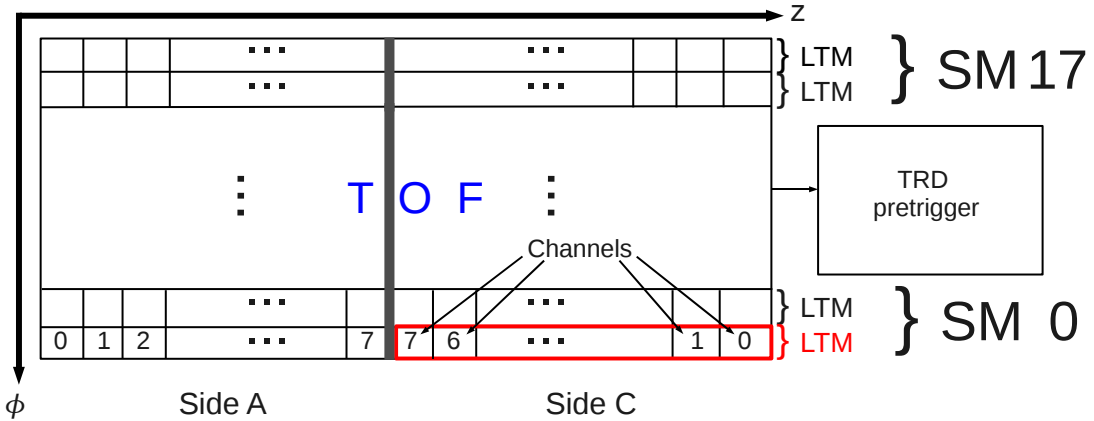
Figure 3.1.: TOF granularity as seen by the TRD pretrigger. There are 4 Local Trigger Modules (LTM) (one example is highlighted in red) per TOF Supermodule (SM), each LTM comprising 8 channels to the TRD pretrigger.

The important aspect with respect to the topology trigger is the granularity of the TOF trigger system: 36 bins in ϕ direction and $2 \cdot 8$ bins in z direction. This implies for the bin size in ϕ the important value: $\Delta\phi = 10°$.

3.3. The Principle of a Topology Trigger

With the knowledge about the TOF granularity for the topology trigger, the basic principle of such a trigger can now be discussed.

3.3.1. Daughters with Infinite p_t

As discussed in section 3.1, the decay of interest is $\Upsilon \to e^+ + e^-$, for which a back-to-back signature of the daughters is expected. However, the magnetic field inside ALICE must be taken into consideration and it must also be kept in mind that TOF lies at the large radius $R_{\mathrm{TOF}} = 3.7$ m [30]. Thus, the daughters' trajectories will be bent in the B-field (see Fig. 3.2). The back-to-back signature is expected to be seen in the limit $p_t \to \infty$ only. For simplicity, infinite transverse momenta will be assumed and the discussion of the consequences of the bending will be
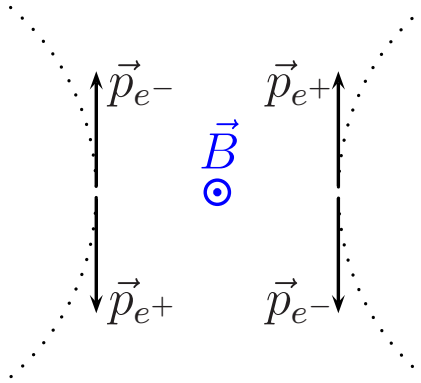
Figure 3.2.: Bending of the e^+ and e^- trajectories in the magnetic field (blue). The solid black lines indicate the initial momenta of the particles, the dotted black lines their trajectories. On the left side, the e^- flies upwards and the e^+ downwards, while the directions are switched on the right side.

postponed to section 3.3.2. With this assumption, straight trajectories and an event signature as shown in Fig. 3.3 are expected.

Furthermore, the z segmentation of the TOF detector will be neglected to make the discussion clearer and simpler. Section 3.6 will investigate, if the result of the following sections will change significantly, when taking into account the z segmentation.

The Lorentz boost is also not considered. Its effect on the event signature will be discussed in section 3.4.

After returning to Fig. 3.3, it is assumed that the red star symbolises a hit in the corresponding bin, i.e., in this case, a ϕ bin of TOF SM 17. A back-to-back signature of the Υ daughters is expected, hence the trigger should fire if there is another hit in the bin exactly on the opposite side. The corresponding bin is denoted by a yellow star.

3.3.2. Daughters with Finite p_t

So far, the curvature of the electron/positron tracks has been neglected by assuming the limit $p_t \to \infty$. Now this assumption will be dropped and finite p_t's will be considered. This will cause the trajectories to be curved and, thus, as can be seen in Fig. 3.2, the $\Delta\phi$ of the electron and the positron will be less than 180°. The deviation from 180° depends on the transverse momenta of the daughters: The lower the p_t, the less the hits at the TOF detector will be back-to-back.

From Fig. 3.2, another aspect can be deduced: If the electron flies to the top and the positron to the bottom of the picture, the bending due to the magnetic field will "move the hits" in Fig. 3.3 closer to each other "to the left" (yellow star anti-clockwise, red star clockwise) compared to the case with infinite transverse
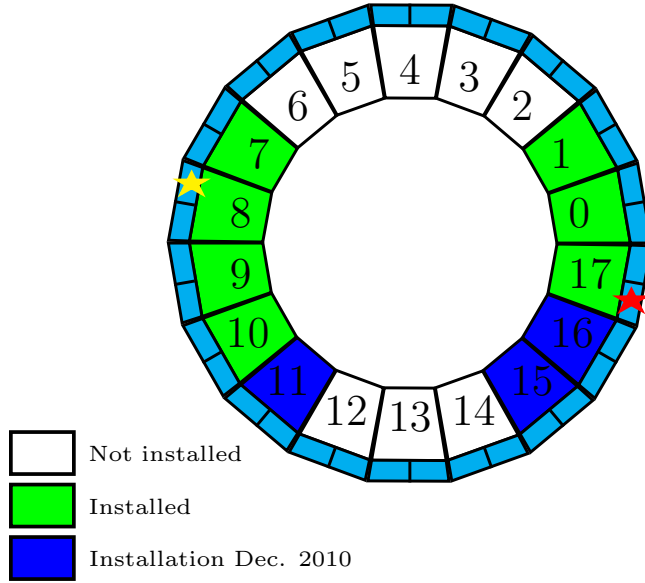
Figure 3.3.: The principle of a topology trigger in the simplest case (real back-to-back signature). Shown are the current status of each TRD SM, the ϕ bins of the TOF SMs (cyan), as well as 2 Hits (red and yellow stars) in back-to-back manner. Remember that each TOF SM provides 2 bins along ϕ.

momenta. However, since it is unknown which particle is the electron and which one the positron at L0, the case with the electron flying to the bottom and the positron flying to the top (right part of Fig. 3.2) has to be considered as well. Then, the magnetic field will move the hits "to the right" (yellow star clockwise, red star anti-clockwise).

To sum up, for finite p_t and given a fixed hit on one side of the TOF detector, the expected hit on the other side can move both, in clockwise and anti-clockwise direction compared to the case of infinite p_t. So, this is a symmetric effect with respect to the difference in azimuthal angle of the hits. How can this be taken into account for the topology trigger?

The idea is to define a "tolerance" as demonstrated in Fig. 3.4. It is assumed that the red star symbolises a hit. For the firing of the trigger, it can now be demanded to have a hit in one of the bins denoted by the yellow stars (logical OR of the yellow stars). This would correspond to a tolerance equal 1, i.e. back-to-back ± 1 bin in ϕ direction (remember that the bin size along ϕ is $\Delta\phi = 10°$).

The tolerance can be increased further, but it must be kept in mind that a too high tolerance is disadvantageous for such a topology trigger, since then the trigger will fire in almost every case — and also in the case of some uncorrelated hits from background. This, of course, will not decrease the L0 trigger rate sufficiently.

It is useful to calculate the deflections of the electrons in the magnetic field with respect to infinite p_t for a fixed (transverse) momentum. In detail, the
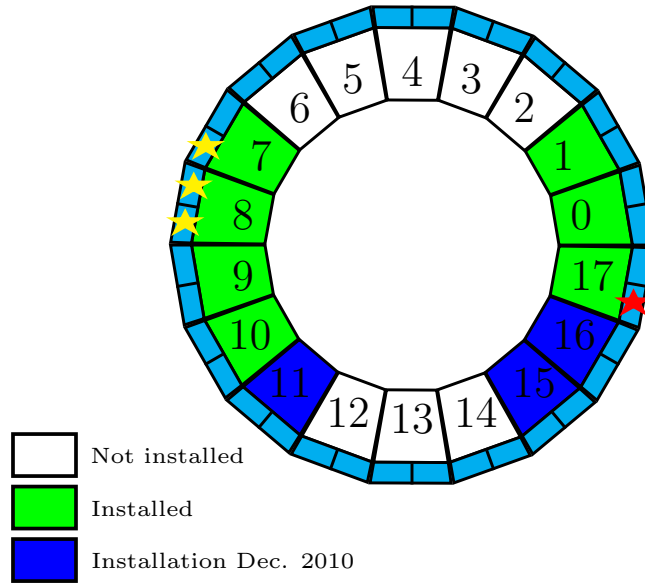
Figure 3.4.: The principle of a topology trigger in the more sophisticated case (back-to-back signature with tolerance ±10°). Shown are the current status of each TRD SM and the ϕ bins of the TOF SMs (cyan). Also drawn in are a hit on the right side of the figure (red star) and the corresponding possible hits on the opposite side (yellow stars) that would cause the trigger to fire (for this fixed tolerance).

interesting quantity is the deflection of one daughter for finite p_t with respect to infinite p_t when reaching the TOF detector, see Fig. 3.5. Another interesting quantity is the deviation of the daughters' $\Delta\phi$ from 180° at the TOF detector. The first angle will be called α, the latter β.

To calculate these angles, the well-known formula for the radius of curvature is needed, which can be easily deduced by equating the Lorentz force and the centripetal force:

$$R_{\text{curvature}}[m] = \frac{p_t[\text{GeV}/c]}{0.3 \cdot B[\text{T}] \cdot |q[e]|},$$

where $R_{\text{curvature}}$ denotes the radius of curvature in meter, p_t the transverse momentum in GeV$/c$, B the magnetic field in Tesla and q the particle's charge in units of the electron charge e. Consequently, electrons/positrons have $|q| = 1$. The typical magnetic field strength of the L3 solenoid of ALICE is 0.5 T.

To determine α and β, the inner radius of the TOF detector needs to be known. In [30], this radius is stated as $R_{\text{TOF}} = 3.7$ m. Considering Fig. 3.6, it can be found:

$$\alpha = 90° - \arccos\left(\frac{R_{\text{TOF}}}{2 \cdot R_{\text{curvature}}}\right).$$
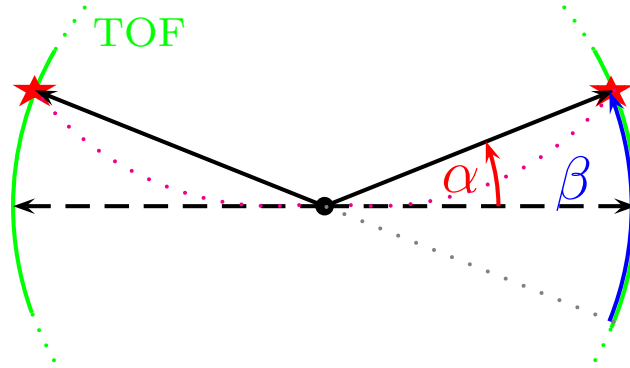
Figure 3.5.: Definition of the deflection angles of the ϒ daughters. The dashed black lines illustrate the flight directions of the daughters for infinite p_t, whereas the solid ones point to the position where the corresponding particle with finite p_t hits the TOF detector (the corresponding trajectories are indicated by dotted magenta lines, the hits by red stars and the TOF detector by the green circle). α is defined as the deflection of one daughter for finite p_t with respect to infinite p_t when reaching the TOF detector. β is the deviation of the daughters' $\Delta\phi$ from 180° at the TOF detector.
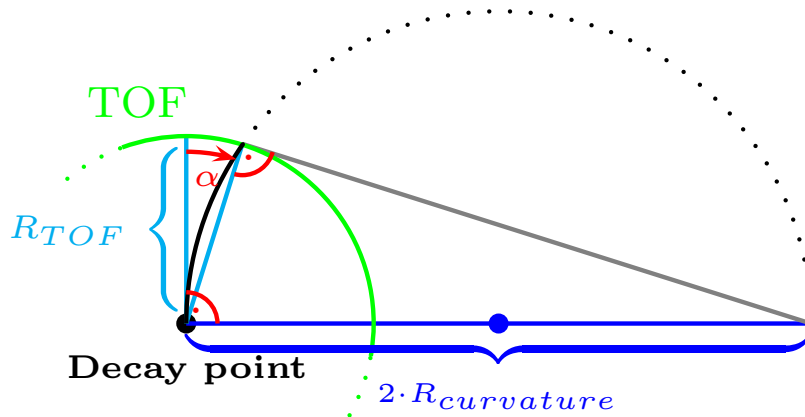
Figure 3.6.: Derivation of the formula for the deflection angle α. The figure schematically displays the TOF detector (green circle around the decay point) and the trajectory of a daughter (black). Using Thales' theorem the angle α can easily be read off as a function of the TOF inner radius R_{TOF} and the radius of curvature $R_{\mathrm{curvature}}$.

Combining both formulas and plugging in the relevant numbers leads to the results shown in Tab. 3.1. Note that for β a decay of the Υ at rest is assumed. In this case, both particles have the same deflection α — one in clockwise, the other one in anti-clockwise direction. This yields the simple relation $\beta = 2 \cdot \alpha$. If the Υ has non-vanishing p_t, this simple relation is no longer valid. However, the values for the decay at rest will be used to get a rough estimation of β.

p_t of e^+/e^-	α [deg.]	β [deg.]
2.5	6.4	12.8
3.0	5.3	10.6
3.5	4.5	9.0
4.0	4.0	8.0
4.8	3.3	6.6
6.3	2.52	5.04
6.4	2.49	4.98

Table 3.1.: Deflections of e^+/e^- in the B-field. The angles are defined in Fig. 3.5. Note that the values for β are only valid for Υ's decaying at rest.

What does this mean with respect to the topology trigger? As Tab. 3.1 suggests, only for electrons with $p_t = 6.4$ GeV/c or higher β is $\leq 5°$, i.e., on average, there is a real back-to-back signature (note that the bin size in ϕ direction is 10°). When considering Υ's decaying at rest, the electrons will have $p_t \leq 4.8$ GeV/c due to energy conservation. In principle, the p_t can become arbitrarily small for daughters with polar angle Θ close to 0° or 180°, i.e. daughters flying approximately in or against z direction. But daughters flying too close to the z-axis lie outside of the acceptance of the central barrel. Hence, they will not be seen by the detector. It was calculated that the p_t of the electrons inside the central barrel's acceptance will be > 3.3 GeV/c in case of decays at rest. This implies that, in this case, β will be between 6.6° and 10°. The size of one bin in ϕ direction is 10°, hence the signature will not necessarily be back-to-back, but might be shifted by 1 bin depending on p_t.

Since the daughters' p_t is not known at L0, there are only two options: Either the trigger efficiency for detecting Υ's is decreased by picking a fixed and small p_t range and adjusting the angles according to this range. Or the tolerance is increased and it is accepted to suffer from higher background from uncorrelated hits. Note that the first method will also introduce a bias. The following sections will investigate, which choice is the best and if there is a viable choice at all.

3.4. Expectations from Υ Simulations

In section 3.3, the basic principle of an Υ topology trigger has been discussed. So far, all ideas have been developed based on rather naive expectations (decay takes place almost back-to-back). This was necessary in order to get some feeling on this subject and how the trigger should qualitatively work.

However, to make quantitative estimations, it is necessary to perform simulations of the Υ decay and look at the corresponding results. For this purpose, the simulation features of AliRoot have been used (cf. section 1.7). The idea is to generate pure Monte Carlo events which contain Υ decays only.

```
AliGenParam* upsilon = new AliGenParam(1,
    AliGenMUONlib::kUpsilon, "CDF pp 7", "Upsilon");
upsilon->SetPtRange(0., 60.0);
upsilon->SetYRange(-1.0, 1.0);
upsilon->SetPhiRange(0., 360.0);
upsilon->SetForceDecay(kDiElectron);
```

Listing 3.1: Specifications for the class *AliGenParam* used for the Υ simulation.

In detail, the class *AliGenParam* has been used with the settings stated in Listing 3.1: For the Υ's p_t spectrum, a CDF[3] scaled distribution for *pp* collisions at 7 TeV is used[4] (see line 1). Then, the p_t range of the Υ's is set to 0-60 GeV/c (line 2), the rapidity range from -1 to 1 (line 3) (it was checked that this is no restriction for the later analysis, since there will be a cut on the acceptance of the central barrel anyway, that is more restrictive) and the ϕ range from 0° to 360° (line 4). Finally (line 5), the decay to $e^+ + e^-$ is forced, since this is the decay channel of interest.

These settings are used to simulate 10^5 Υ decays.

So far, all the mentioned cuts (see Listing 3.1) are applied during the simulation. However, a further cut has been used for the analysis, namely a cut on the acceptance of the central barrel: Only decays with both daughter particles having polar angles $45° \leq \Theta \leq 135°$ are taken into account.

Figure 3.7 shows the p_t spectrum of the Υ's. As can be seen from this figure, the p_t cut in the simulation ($0 \leq p_t \leq 60$ GeV/c) poses no harm, since the Υ yield for such high transverse momenta (≥ 30 GeV/c) is negligibly small. According to this plot, it is also expected that most of the Υ's exhibit a p_t of 3.5 GeV/c, but that also approximately 6% of them have a $p_t > 15$ GeV/c.

---

[3]**C**ollider **D**etector at **F**ermilab, see URL http://www-cdf.fnal.gov.
[4]The CDF data for $\sqrt{s} = 1.8$ TeV [57] is extrapolated to LHC energies. Details about this extrapolation can be found in [58].
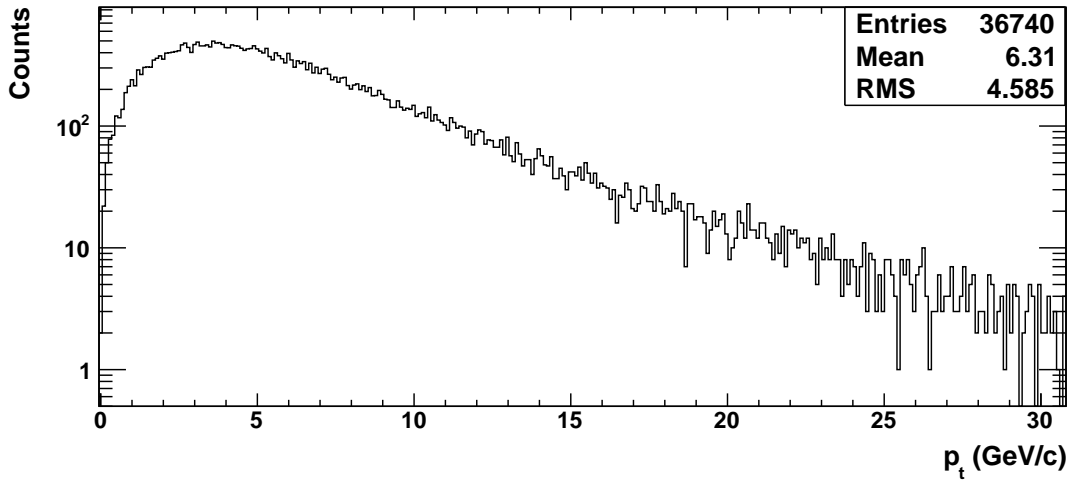
Figure 3.7.: Simulated p_t spectrum of the Υ's. Only Υ's with daughters with polar angle $45° \leq \Theta \leq 135°$ are taken into account.

The figure also shows that approximately $(367.4 \pm (1.9)_{\text{stat.}}) \cdot 10^2$ of 10^5 simulated events pass the Θ cut on the daughters. Since this cut represents the acceptance of the ALICE detector for Υ's, this acceptance is approximately $\epsilon_{\text{acc}}^{\text{ALICE}} \approx 40\%$ (also see section 3.1).

With respect to the Υ trigger, the distribution of the daughters' $\Delta\phi$ at the decay point, i.e. the ϕ angle between the daughters, is a crucial quantity. It is worth mentioning that there is a p_t dependent bending of the daughters' trajectories in the magnetic field until they reach the TOF detector (see section 3.3.2). This will complicate the interpretation of the detected hit signature further.
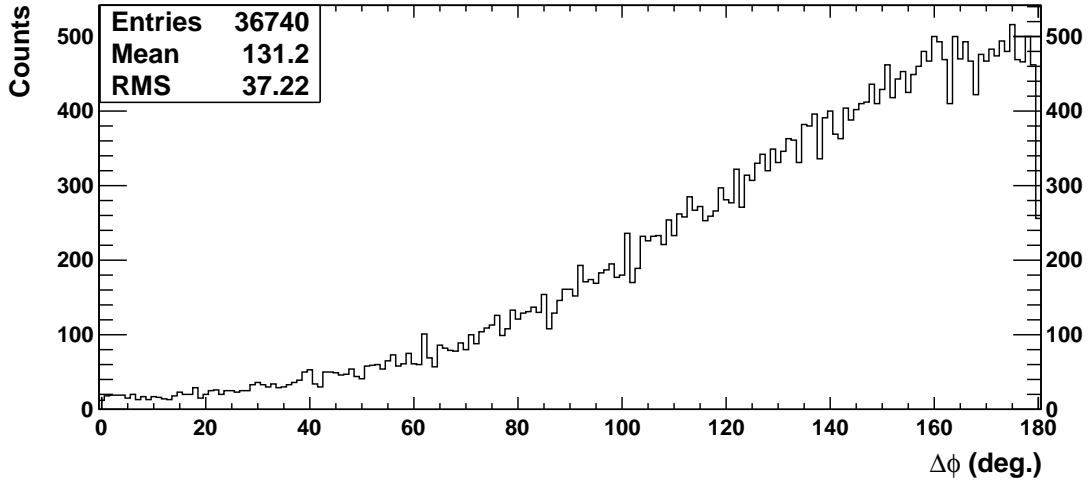
Figure 3.8.: Simulated $\Delta\phi$ of the Υ daughters at the decay point, i.e. the azimuthal angle between e^+ and e^-. Only Υ's with daughters with $45° \leq \Theta \leq 135°$ are taken into account.
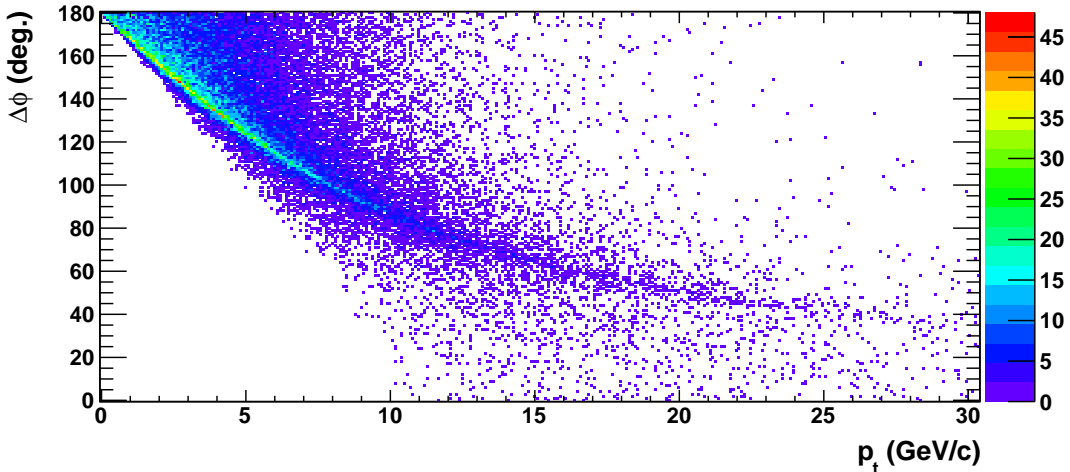
Figure 3.9.: Simulated correlation between $\Delta\phi$ of the Υ daughters and the transverse momentum of the Υ's. Only Υ's with daughters with $45° \leq \Theta \leq 135°$ are taken into account.

However, the underlying $\Delta\phi$ distribution is of great importance and should be investigated. It is illustrated in Fig. 3.8. As naively expected (and discussed in preceding sections), there are a lot of decays resulting in back-to-back configuration, i.e. with angles close to 180°. Yet, about 70% of the decays have angles smaller than 160° and approximately 5% have angles even smaller than 60°.

This casts doubts on the Υ trigger, since there seems to be no clear back-to-back signature, but a rather broad distribution of $\Delta\phi$. What is the reason for this issue? To understand the problem, Fig. 3.9 can be considered, which shows the $\Delta\phi$ of the Υ daughters plotted against the transverse momentum of the Υ. As expected, a strong correlation between these quantities is visible: The larger the Υ's transverse momentum, the smaller the daughters' $\Delta\phi$ can be. How can this very important figure be explained?

As a start, the Υ decay in the Υ's rest frame will be considered (cf. Fig. 3.10a). The daughters will fly apart from each other back-to-back in some arbitrary direction — the decay is isotropic in this frame. First, note that a boost in z direction will not change $\Delta\phi$. Therefore, the case with $p_z^\Upsilon = 0$ can be considered for simplicity. Second, there is no preferred direction in the x-y plane, which allows for arbitrarily choosing a boost in x direction, i.e. $p_t^\Upsilon = p_x^\Upsilon$ without restriction. This means the Υ flies into x direction in the lab frame.

If the daughters fly along the x-axis (or close to this direction), the boost will not (or only slightly) change the daughters' $\Delta\phi$, i.e. $\Delta\phi$ will be (approximately) equal to 180°. This explains, why there are entries in the upper part of Fig. 3.9 even for higher p_t. Note that this explanation implicitly assumes the Υ's transverse momentum not to exceed that of a daughter. Otherwise, both daughters would fly into the same direction in the lab frame, thus, having small $\Delta\phi$.

(a) Effects of the boost

(b) Effects of the central barrel's acceptance
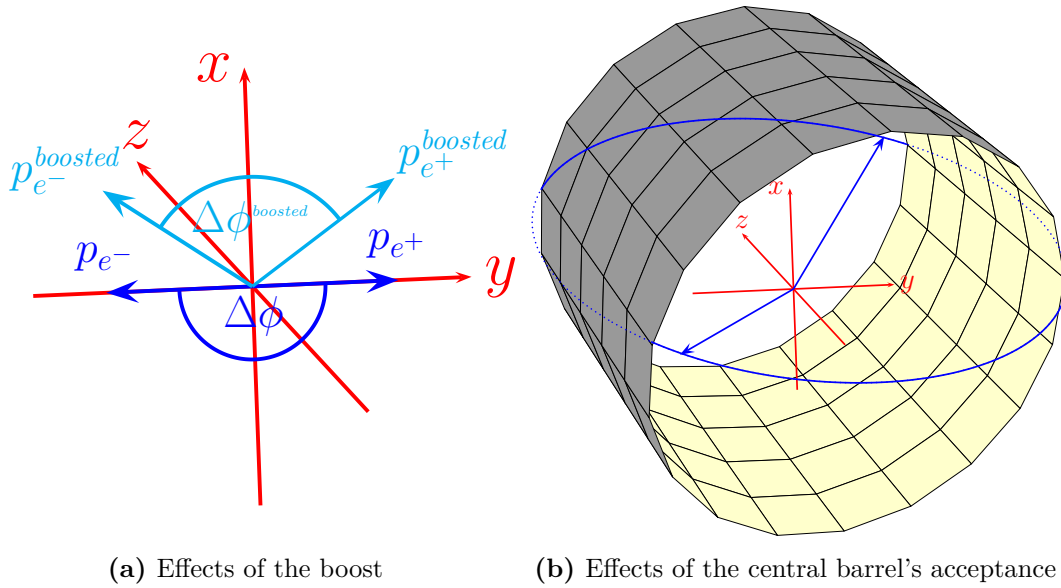
Figure 3.10.: The effects of the boost from the Υ's rest frame to the lab frame are shown in **a)**. The blue vectors indicate the momenta of the Υ daughters in the Υ's rest frame, whereas the cyan ones are the daughters' momenta after the boost into the lab frame. The boost is assumed to be in x direction. Also shown is the daughters' $\Delta\phi$ for both cases.

In **b)**, the outer part of the central barrel is sketched to illustrate the effects of the central barrel's acceptance in Υ decays. The momentum of the Υ daughters in the lab frame is indicated by the blue vectors, which form a "V"-like structure. A rotation of this "V" about the x-axis is allowed by 4-momentum conservation. The blue circle denotes this rotation. If the "V" falls on the circle's solid part (as shown), the particles will be out of the central barrel's acceptance.

For daughters flying along the y-axis, the corresponding momentum vectors form a "V"-like structure after the boost into the lab frame (see Fig. 3.10a). The higher the Υ's p_t, the smaller the opening angle of this "V" will be. 4-momentum conservation allows cases in which the "V" is rotated about the x-axis. Of course, such a rotation changes $\Delta\phi$ and can even lead to $\Delta\phi = 0°$, if the "V" is rotated into the x-z plane.

Yet, there is a white "gap" in Fig. 3.9 in the region of low $\Delta\phi$ and low p_t. This is a consequence of the central barrel's acceptance (cf. Fig. 3.10b): A rotation about the x-axis makes the daughters' momentum vectors (the "V") describe a circle (blue in the figure). Obviously, for a sufficiently large opening angle of the "V", the daughters will be outside of the central barrel's acceptance for some rotations of the "V" (solid part of the blue circle). Especially, this will happen for the configuration with the "V" approximately parallel to the x-z plane, which corresponds to rather small $\Delta\phi$. Consequently, small detectable values of $\Delta\phi$ can only be achieved for a sufficiently large p_t of the Υ. Such a p_t leads to an

adequately small opening angle of the "V", such that the "V" will touch the top of the central barrel in Fig. 3.10b for every rotation about the x-axis.

But what causes the peak structure (green band) in Fig. 3.9? To get $\Delta\phi$, the "V" is projected onto the x-y plane. As stated above, the "V" can be rotated about the x-axis without violating 4-momentum conservation. But projections onto the x-y plane map all "V's" that lie approximately parallel to this plane nearly onto the same points. This implies that the corresponding $\Delta\phi$'s will belong to the same $\Delta\phi$ bin. Thus, due to the projection character of $\Delta\phi$, a certain value of $\Delta\phi$ will be favoured, i.e. appear most abundantly. As mentioned before, the opening angle of the "V" depends on the Υ's p_t. But this angle is equal to $\Delta\phi$, if the "V" lies in the x-y plane. As a result, the favoured value of $\Delta\phi$ depends also on p_t.

A discussion in section 3.6 will demonstrate that the phase space prefers configurations with both daughters having $\Theta = 90°$, i.e. daughters flying in the x-y plane, as well. This amplifies the "peak" effect.

Note that the favoured value of $\Delta\phi$ is different from the minimum possible one (upper edge of the white "gap") for adequately high p_t. This is because the first appears in cases with the "V" lying in the x-y plane, but the latter in cases with the "V" as parallel to the x-z plane as possible.

All these trends of the "peak" can be clearly seen in Fig. 3.9.

What is the bottom line of all this? Remember some facts: First, there is no information about the momenta of the daughters at L0. Second, it makes no sense to run a topology trigger with too high tolerance with respect to the background (cf. discussion in section 3.3.2). But Fig. 3.9 reveals that a high tolerance is needed, if all Υ's (with daughters having a broad distribution in $\Delta\phi$) are to be triggered.

Nevertheless, there might be a way out: If it is e.g. decided to concentrate on Υ's at rest or close to it, for instance $0 \leq p_t \leq 1$ GeV/c, the $\Delta\phi$ of the daughters is between 160° and 180°. This allows for a rather small tolerance. Alternatively, it can also be tried to concentrate on the "peak" in $\Delta\phi$ for high p_t (e.g. the peak is around $\Delta\phi = 120°$ for $p_t = 6$ GeV/c) and sacrifice the rest of the events with different $\Delta\phi$. Yet, it must be paid attention to the fact that, in this case, only a "sample" for a given p_t range is chosen, which might introduce a bias.

3.5. Background Estimation

At next, the background needs to be estimated. As pointed out in the last section, it is possible to concentrate on Υ's with small p_t to be able to use small tolerances for the trigger. So, the final goal is a background estimation as a function of the tolerance. This will allow to see which tolerances are practicable and, as a consequence, which freedom exists in choosing the Υ's p_t range for the trigger.

3.5.1. Background from Uncorrelated Hits

The topology trigger is designed to look at hits that are positioned more or less back-to-back (see sections 3.3 and 3.3.2), since this is the expected signature for the Υ decay at low p_t (cf. section 3.4). Yet, it is possible to get the same signature from uncorrelated hits because there exist also many other particles after the collision. Consequently, the question arises how probable it is to get a back-to-back signature from uncorrelated hits.

To answer this question, the following situation in Fig. 3.4 (p. 41) can be imagined: There are x hits, e.g. $x = 2$ for a first simple demonstration. These hits are assumed to be uncorrelated and, since there is no preferred direction in the x-y plane, uniformly distributed over the 36 ϕ bins of the TOF trigger modules. It is now desirable to figure out the probability to get a trigger for a fixed tolerance and a given number of hits x.

For a quantitative answer, the random number generator of ROOT [39] can be used. The first step is to divide the interval [0,1] into 36 bins. Then, a random number with a uniform distribution in [0,1] is generated and the corresponding bin is filled, i.e. a hit is assigned to this bin. Since the detector can only notice, whether there was a hit or not, it will not be distinguished between 1 or more hits in a bin.

Finally, it is checked for each bin with a hit whether the bin on the opposite side (for tolerance = 0) also got a hit. If this is true for at least one bin, the trigger will fire for this event. This procedure is repeated 10^5 times and the number of triggered events is divided by the total number of events, giving the probability for a trigger from uncorrelated hits.

The generalisation for tolerance > 0 is obvious (cf. Fig. 3.4 (p. 41) and corresponding discussion). Note that combinatorics can be used as well to calculate these probabilities. In the case of 2 hits, this is easy and can be used to check if the MC method described above gives the same result[5]. However, for more than 2 hits, the combinatorial approach becomes complicated. That is why the MC method has been chosen.

Fig. 3.11 shows the probability for a trigger from uncorrelated hits for tolerance = 0 (black line), 1 (red line) and 2 (green line), respectively.

A reasonable background probability for the topology trigger should be in the order of 10%. As Fig. 3.11 suggests, this can only be achieved for tolerance = 0, if there are at most 4 hits per event. For tolerances ≥ 1, even 3 hits seem to be too much. Of course, this critical number of hits would further decrease for larger tolerances.

Obviously, a serious problem arises, since 4 or more hits should occur quite

---

[5]This is indeed the case: The probability to get a hit in bin x is $\frac{1}{36}$. For tolerance = 0, the trigger fires, if there is a hit in the bin on the opposite side of bin x (probability $\frac{1}{36}$). There are 36 possibilities for x, so the probability for a trigger from 2 uncorrelated hits is $p(x = 2) = 36 \cdot \frac{1}{36} \cdot \frac{1}{36} = \frac{1}{36} \approx 0.03$.
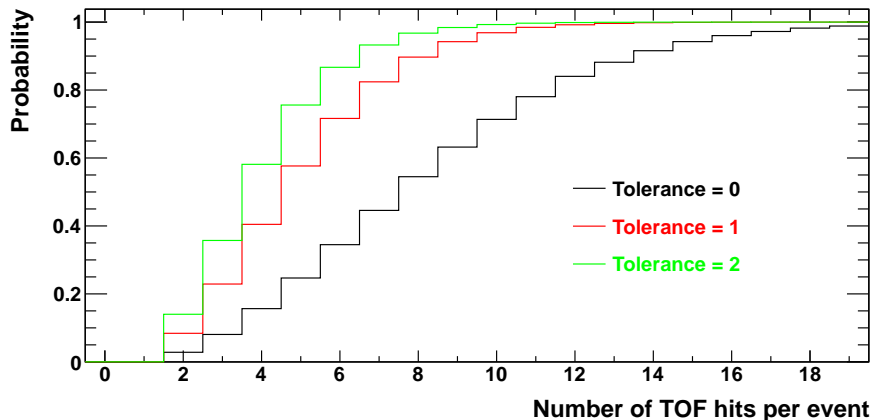
Figure 3.11.: Probability to get a trigger from uncorrelated hits for tolerance = 0 (black), 1 (red) and 2 (green). For more than 20 TOF hits per event (not shown) the probability is approximately unity in all cases.

frequently in proton-proton collisions (and many more hits in lead-lead collisions). This would imply that the trigger fires in every second event or even more often, although there was no Υ decay in any of these events. This is a rather unpleasant result, since the major goal of the dedicated L0 trigger is to decrease the L1 input rate, which would be only a factor 2 or less compared to a minimum bias trigger.

3.5.2. Analysis of Minimum Bias Data

This section takes a deeper look at the observed multiplicity of proton-proton collisions. How can the last section's final statement that "4 or more hits occur quite frequently" be quantified? One strategy, that will be pursued in the following, is to look at minimum bias (raw) data for proton-proton collisions from the LHC10c run period in 2010.

Yet, there is some trouble in simply opening raw files and counting hits. There will be pathologically noisy channels, that spoil the multiplicities. So, the first task is to identify these noisy channels and to create a mask for them. As soon as the mask has been created, the minimum bias data can be analysed and the corresponding multiplicities can be determined.

3.5.2.1. Mask Creation for Noisy Channels

To create a mask for pathologically noisy channels, these need to be identified first. To achieve this, empty bunch crossings can be used by doing the following: When looping over the raw events, only events of type "Physics" are taken into account[6]. From these events, those with the trigger class *CINT1-E-NOPF-ALL* are selected.

---

[6]Other event types are "Calibration", "Start of run" etc.

The name of the class encodes information about the trigger condition [59]: The 'C' is simply a prefix for each class, while 'INT1' stands for "interaction 1", which means that interaction events of version 1 are triggered. The version denotes which condition on the trigger inputs is used to declare an event as an interaction event. Next, 'E' represents that there were empty bunches on both sides, A-side and C-side (cf. Fig. A.1, p. 107). 'NOPF' indicates the absence of past-future protection conditions (cf. section 1.6) for this trigger class. Finally, 'ALL' means that all ALICE detectors are read out.

The multiplicities of the selected events can be extracted using the AliRoot class *AliTOFTrigger*, which provides the function *GetTRDmap* that returns the hit map as seen by the TRD pretrigger. The result for data of run 118560 is depicted in Fig. 3.12. In order to have fast access to data (faster than getting data from the grid), the processing was performed on the cluster at GSI[7] and as input the data available there has been used.
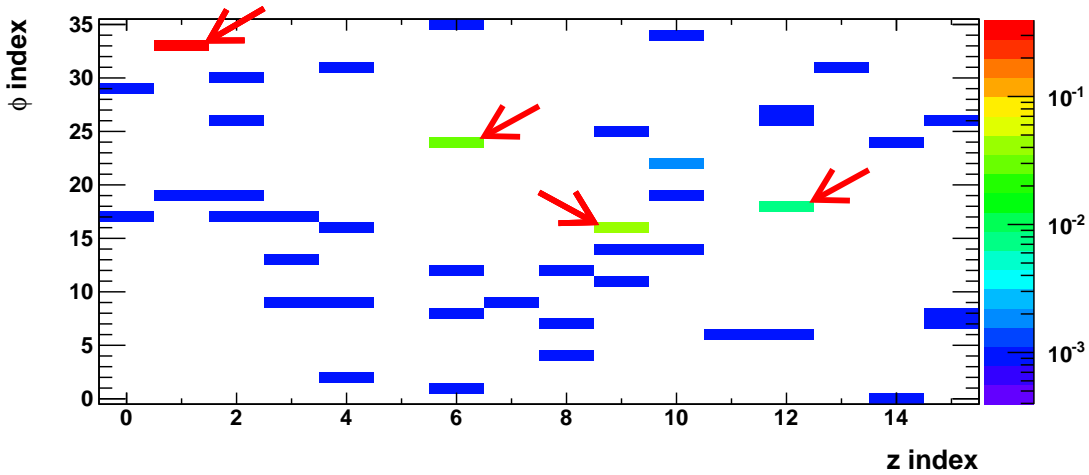
Figure 3.12.: TOF hit map for empty bunch crossings. Plotted are the hits as a function of the ϕ and the z index. The entries are normalised to the number of events. The most prominent noisy channels are indicated by red arrows. This plot is based on parts of the raw data of run 118560.

Since empty bunch crossings are considered, there should be no hits produced by particles, but only from noise. As illustrated in Fig. 3.12, there are indeed some noisy channels for this run.

In order to loose as little information as possible, the strategy is to take only the most prominent noisy channels and mask them out. These channels are indicated by the red arrows in Fig. 3.12. However, if this analysis is carried out for different runs, different channels are found to be noisy from run to run. This causes some trouble, since it implies that a single mask would have to be created

---

[7]"GSI Helmholtzzentrum für Schwerionenforschung GmbH". The original name was "**G**esellschaft für **S**chwer**i**onenforschung mbH". See URL `http://www.gsi.de`.

for every run. To get this trouble under control, it can be tried to iteratively add up the noisy channels of each run and see if the mask converges sufficiently fast.

Fortunately, it turned out that the mask seems to converge after 3 runs[8]. It is a very promising result that only 8 of the $36 \cdot 16 = 576$ channels (cf. Fig. 3.12) are denoted as noisy and, therefore, masked out. It would remain a future task to check, if the mask is valid for other runs.

Now, that the mask has been created successfully, it can be looked at minimum bias data. It will also be shown that the mask works properly.

3.5.2.2. TOF Raw Multiplicities

To look at minimum bias interaction events, the trigger classes *CINT1-B-NOPF-ALL* or, equivalently, *CINT1B-ABCE-NOPF-ALL* for events of type "Physics" are selected. The class name *CINT1-B-NOPF-ALL* can be interpreted as in section 3.5.2.1: The 'B' indicates the presence of filled bunches on both sides, A-side and C-side. The 'B-ABCE-' is just an older naming scheme for '-B-'.

The result for run 119859 is shown in Fig. 3.13. The effect of the masking can clearly be seen: On the one hand, the "peaks" from the noisy channels in Fig. 3.13a are gone in Fig. 3.13b, as desired. On the other hand, there is a more or less flat distribution with a slight asymmetry: fewer hits for high z indices. The same asymmetry for minimum bias events has been observed by the TRD and might be an effect of the muon absorber, which is situated at high z indices (cf. Fig. A.1 on p. 107, high z indices correspond to negative z values in the ALICE coordinate system).

The "blanks" are either due to missing detector parts or due to the fact that the detector indeed notices a hit, but there is a malfunction in converting and forwarding the information at the trigger level. This causes the white half-rows in Fig. 3.13. By counting the "blanks" in Fig. 3.13a, it is found that there are 141 channels off for this run. This is a huge number compared to the 8 noisy channels, that are masked out.

Counting the number of hits for every event, the multiplicities can be obtained as illustrated in Fig. 3.14, which shows again data of run 119859. The mask excludes the noisy channels, hence the mean multiplicity decreases slightly from 18.08 (black) to 17.34 (red) in Fig. 3.14. The most probable value is in both cases around 5. Unfortunately, this is still a far too high mean value with respect to the topology trigger, as a glance back on Fig. 3.11 reveals: The probability for a trigger from 17 uncorrelated hits is close to 1. Even for 5 hits and tolerance $= 0$, the probability is around 25%.

These first results do not look very promising.

---

[8]The runs 118556, 118557 and 118560 have been used to create the mask. Afterwards, the mask has been tested successfully with the runs 118561, 118903, 119859, 119923 and 120503, i.e. no further noisy channels have been found.
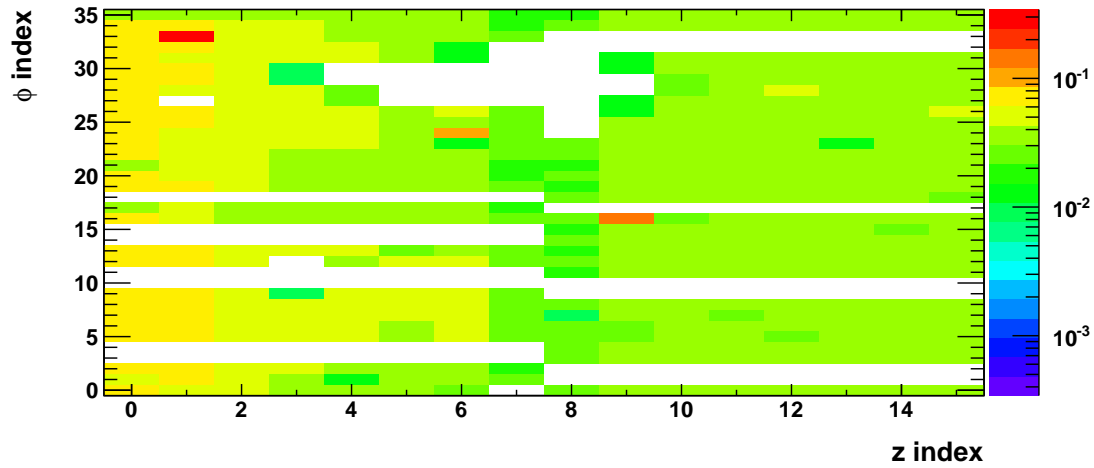
(a) TOF hit map before masking
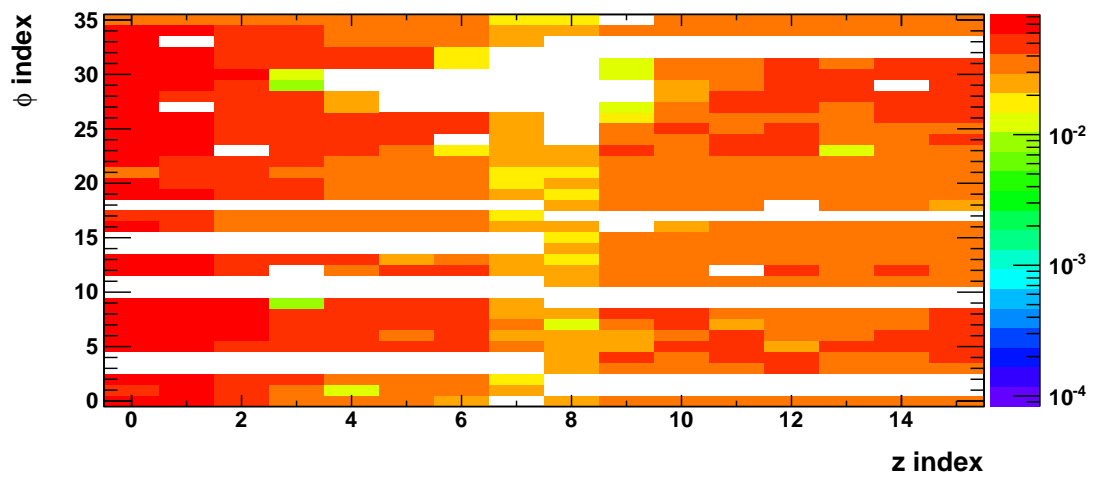
(b) TOF hit map after masking

Figure 3.13.: TOF hit map for minimum bias interaction events **a)** before, **b)** after the masking of noisy channels. Plotted are the hits as a function of the ϕ and the z index. The entries are normalised to the number of events. These plots are based on parts of the raw data of run 119859.
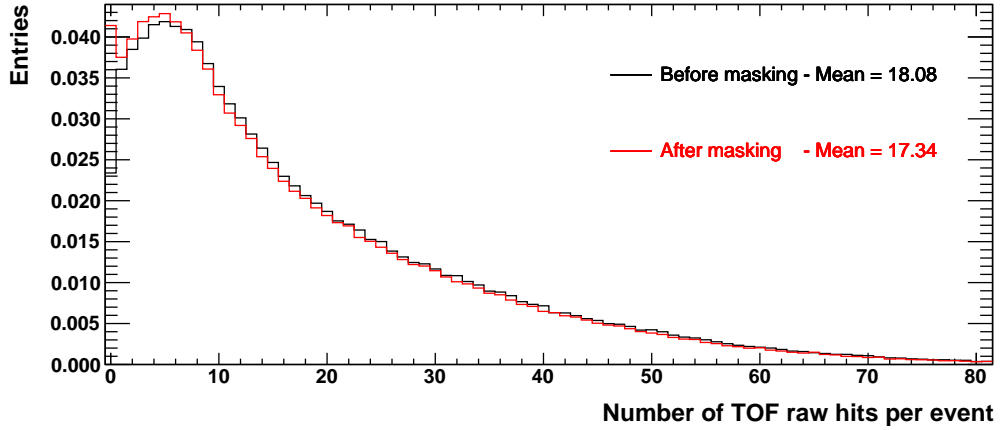
Figure 3.14.: TOF multiplicities for minimum bias interaction events before (black line) and after (red line) the masking of noisy channels. The entries are normalised to the number of events. This plot is based on parts of the raw data of run 119859.

3.5.3. Results

To get a more quantitative result, the background for the trigger can be estimated as follows: It is assumed to have randomly distributed hits with the multiplicities that have been extracted from data (in this case data of run 119859, cf. Fig. 3.14). The multiplicity distribution is normalised to the number of events, thus, each bin gives the probability to get a certain number of hits in an event. This distribution is then convoluted with the probability to get a trigger for a certain number of (uncorrelated) hits, see e.g. Fig. 3.11, p. 50. Finally, after integrating the resulting histogram, this yields the probability for a trigger from background with a fixed tolerance, as shown in Tab. 3.2.

Tolerance	Probability for a trigger from background [%]
0	67
1	78
2	82
3	84

Table 3.2.: Probabilities for a trigger from background for a fixed tolerance. The values have been obtained by considering parts of the raw data of run 119859.

The obtained values correspond to run 119859, but are the same within one percent for the runs 119923 and 120503. The results are discouraging, since the probability for a trigger from background is nearly 70% even for tolerance = 0. This means that the topology trigger would fire in 70% of the events, even if there is no Υ in any of these events.

As expected, the background increases for larger tolerances.

The major goal of the Υ topology trigger is to decrease the L0 trigger rate compared to a minimum bias trigger. However, these results imply that the L0 trigger rate can only be decreased by less than a factor of 2 in the most optimistic case.

3.6. Effects of the *z* Granularity

So far, the TOF detector's *z* segmentation has not been used. The question is if the trigger performance could be improved with the additional *z* information. This would be the case, if there was a useful correlation between $\Delta\phi$ and $\Delta\Theta$ of the Υ daughters. If this is not true, the higher *z* granularity will not improve the signal-to-background ratio. The objection that a 16 times higher granularity would definitely decrease the background for single bins, situated on opposite sites, can be overruled, since this would dramatically decrease the trigger's efficiency as well. This means that both, signal and background, decrease in this case.
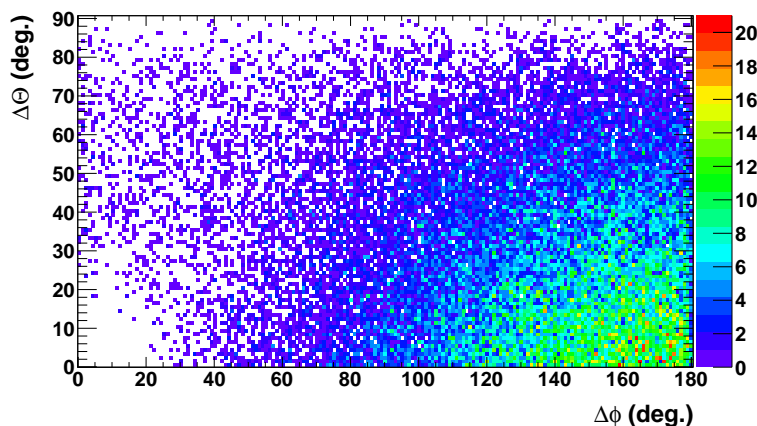
Figure 3.15.: Simulated correlation between $\Delta\phi$ and $\Delta\Theta$ of the Υ daughters at the decay point. Only Υ's with daughters with $45° \leq \Theta \leq 135°$ are taken into account.

A simulation of the correlation between $\Delta\phi$ and $\Delta\Theta$ of the Υ daughters is illustrated in Fig. 3.15. Apparently, there is no correlation that can be used for the topology trigger. Yet, at first sight, it is surprising to find the daughters concentrated at $\Delta\Theta = 0$ for not too low $\Delta\phi$'s. This observation can be traced back to the correlation between η and $\Delta\phi$ of the Υ daughters, which is shown in Fig. 3.16. Besides the plot with the usual cut on Θ (Fig. 3.16b), the same plot without this cut is shown (Fig. 3.16a) in order to see the effect in full glory.

Obviously, the daughters have preferably a pseudo-rapidity η around 0. This can be understood by considering the phase space at some fixed radius *r*:

$$d^3x = r^2 \cdot \sin(\Theta) \cdot dr \cdot d\phi \cdot d\Theta.$$

(a) No Θ cut on Υ daughters (b) With Θ cut on Υ daughters
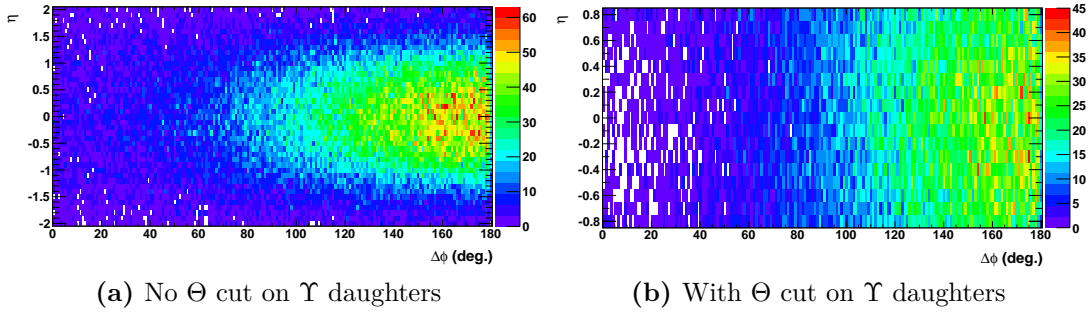
Figure 3.16.: Simulated correlation between η and $\Delta\phi$ of the positrons from Υ decays at the decay point. **a)** No Θ cut has been applied on the Υ daughters, **b)** only Υ's with daughters with $45° \leq \Theta \leq 135°$, i.e. $|\eta| < 0.88$, are taken into account. The correlation is identical to that of electrons.

The key is the factor $\sin(\Theta)$, which is maximal for $\Theta = 90°$. Finally, the relation between the angle Θ and the pseudo-rapidity η is:

$$\eta = -\ln(\tan(\frac{\Theta}{2})).$$

This implies that $\Theta = 90°$ corresponds to $\eta = 0$. As a result, the phase space for each of the daughters is maximal for $\Theta = 90°$, so that the daughters most likely have the same Θ, i.e. $\Delta\Theta = 0$. This phase space argument explains the observation concerning Fig. 3.15.

In conclusion, there seems to be no useful correlation that could improve the trigger performance with the help of better z granularity.

3.7. Conclusion

Section 3.5.1 only dealt with the background from uncorrelated, uniformly distributed hits. This should be a rough estimation for the total background, since there is no preferred direction in the x-y plane. However, uncorrelated hits are not the full story. Also jets will be produced and there will be J/ψ production as well. These J/ψ's can decay via $J/\psi \rightarrow e^+ + e^-$ in a manner close to back-to-back. This kind of background has not been taken into account yet and will worsen the results collected so far — which are already not very promising.

To sum up, the $\Delta\phi$ of the Υ daughters at the decay point is very broadly distributed. For a high efficiency of the Υ trigger, a high tolerance would be required. Furthermore, the p_t dependent bending of the daughters' trajectories in the magnetic field until they reach the TOF detector might force an increased tolerance. However, the background estimation suggests that, even in the most optimistic case, the background is very high. Thus, it is advisable to stick to very

small tolerances or even tolerance = 0 for the sake of a smaller background, even if this decreases the efficiency.

Obviously, it is impossible to get high efficiency and a small background with such a topology trigger. So, this trigger can be at most feasible in triggering on Υ's with low p_t, i.e. Υ's approximately decaying at rest.
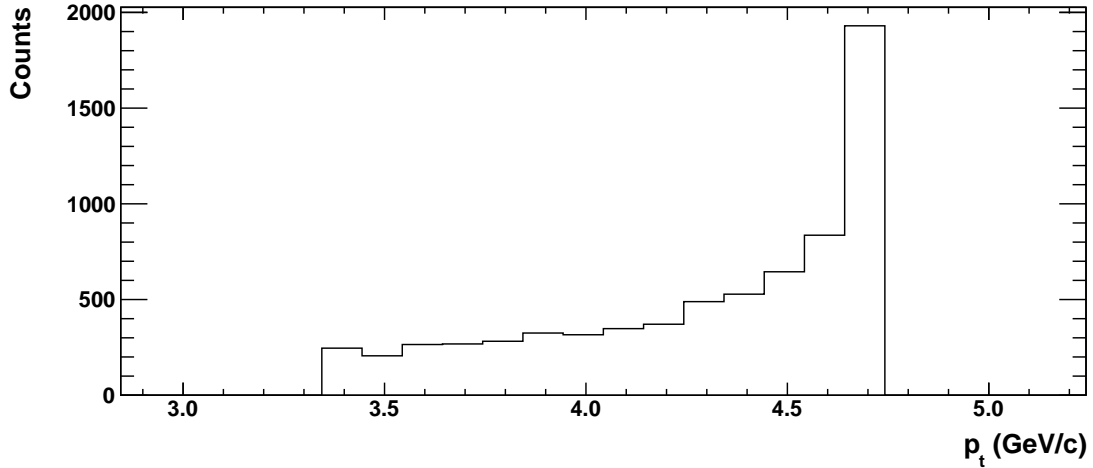
Figure 3.17.: Simulated p_t spectrum of electrons from Υ's decaying at rest and having daughters with $45° \leq \Theta \leq 135°$. Note that the abscissa starts at 2.8 GeV/c.

Simulating Υ's decaying at rest (by setting the total and transverse momentum range in the simulation to zero) yields the electron p_t spectrum shown in Fig. 3.17. The spectrum of the positrons is identical. The upper limit of ≈ 4.7 GeV/c is due to energy conservation ($\Leftrightarrow$ mass of Υ), while the lower limit is introduced by the cut on the polar angle Θ of the daughters.

Evidently, for the daughters, the relation 3.3 GeV/$c < p_t < 4.8$ GeV/c is valid. According to Tab. 3.1 (p. 43), this implies $6° \lesssim \beta \lesssim 10°$ (see Fig. 3.5 (p. 42) for the definition of β), i.e. $\Delta\beta \lesssim 4°$. This is well below $\Delta\phi = 10°$ for the TOF bin size in ϕ.

Thus, tolerance = 0 would be feasible, if one restricts oneself to Υ's decaying at rest. However, even in this case, the reduction of the L0 trigger rate is expected to be less than a factor of 2. As it was checked, the result cannot be improved by making use of a better z granularity.

There is still one important aspect left: Assuming that the TOF detector is able to issue a pretrigger signal for correctly identified Υ events and that the TRD properly detects and identifies the daughters as electrons, can the daughters from this decay be used for an L1 trigger contribution from the TRD?

The answer to this question can be found in Fig. 3.18. For the TRD, only particles with $p_t \geq 3$ GeV/c are used for the evaluation of the L1 trigger condition because their trajectories in the TRD can be reconstructed [60]. This threshold
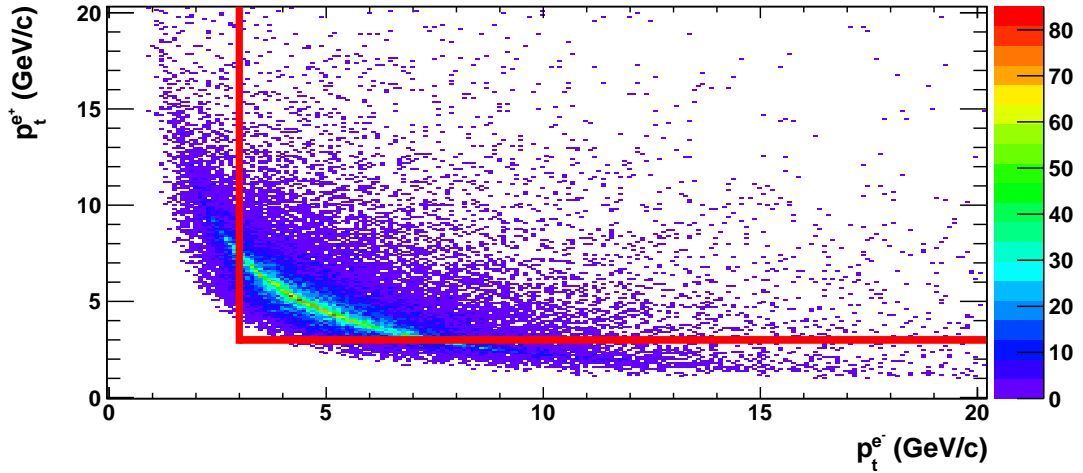
Figure 3.18.: Simulated p_t spectra of Υ daughters with $45° \leq \Theta \leq 135°$. For an evaluation of the L1 trigger condition, trajectories in the TRD (in this case of e^+/e^-) with $p_t \geq p_t^{\text{threshold}} = 3$ Gev/c can be reconstructed [60]. The big red lines mark this threshold, i.e. daughters on the upper right side of this red box can be used for the evaluation of the TRD L1 trigger condition.

is symbolised in the figure by the red lines: Every entry in the histogram which lies above the horizontal and to the right of the vertical red line marks an event in which both daughters fulfil this criterion. Fortunately, as the figure suggests, the major part of the events falls into this category. Under the assumption of a proper electron identification by the TRD, Υ triggering with a TOF pretrigger–TRD L1 trigger combination is, in principle, manageable. But the reduction of the L0 trigger rate compared to a minimum bias trigger is expected to be less than a factor of 2.

4. Online Particle Identification with the ALICE TRD

In this chapter, the principle and performance of the online Particle Identification (PID) with the ALICE TRD are described. Furthermore, the analysis strategy to find the influence of various parameters like gas gain, drift velocity, Tail Cancellation (TC) etc. are introduced. The analysis is based on simulations. In chapter 5, the corresponding results and conclusions will be discussed.

4.1. Basics of PID with the ALICE TRD

4.1.1. Definition of Quantities for PID

First of all, it is necessary to introduce various quantities that allow for quantitative statements with respect to the PID performance. Parts of the following discussion are based on [43], where further details can be found.

The first important quantity is the *electron likelihood* which is defined in this thesis as follows: The electron likelihood is the probability of a particle to be an electron without taking into account any a-priori probabilities. This means that the electron likelihood does not depend on the relative abundance of the observed particle species.

There are two quantities that can be used as a measure of the e/π-separation, namely electron efficiency and pion efficiency. The *electron efficiency* ε_e is the fraction of electrons correctly identified as electrons. Similarly, the *pion efficiency* ε_π gives the fraction of pions misidentified as electrons. Obviously, these quantities are not independent of each other because demanding a high electron efficiency results in a higher pion efficiency. Therefore, the pion efficiency can be considered as a function of the electron efficiency. Usually, the electron efficiency is fixed to some value, generally 90%.

Instead of the pion efficiency, the *pion suppression* $1/\varepsilon_\pi$ can be considered which is the reciprocal of the pion efficiency. It is sometimes also called *pion rejection*. The design goal of the TRD is a pion suppression of 100 for 90% electron efficiency and momenta above 3 GeV/c [42]. In fact, even a pion suppression above 10 or a lower electron efficiency would still considerably improve the PID performance of ALICE.

4.1.2. Principle of Online PID with the ALICE TRD

Before any analysis can be performed, it is required to understand how the PID of the ALICE TRD is implemented online. The idea is to assign an electron likelihood to each tracklet of a track and finally to combine these to yield an electron likelihood for the whole track. As stated in section 2.6.3, Look-Up Tables (LUT) are used to quickly "calculate" the tracklet likelihood online. Thus, the PID performance analysis can be divided into two steps: First, the LUT needs to be created. Second, this LUT is applied to particle data to investigate the PID performance. In this thesis, the data for both steps stems from simulations.

But how are the LUTs created? There are various methods to get tracklet likelihoods, for instance:

- likelihood on total deposited charge (LQ). The total deposited charge is just the sum Q_0 of a certain time bin range (e.g. time bins 2-26) of the pulse height (cf. Fig. 4.1; here, Q_0 and Q_1 together cover the time bins 2-26).

- two-dimensional likelihood on deposited charge in two chamber sectors (2D LQ). As for the previous method, the charge of some time bins is summed. However, there are now two such summation windows Q_0 and Q_1, e.g. Q_0 ranging from time bin 2 to 17 and Q_1 from 18 to 26 (see Fig. 4.1). Note that Q_1 can also start later than Q_0 ends, such that there is a "gap" between the summation ranges of Q_0 and Q_1. Similarly, an overlap of the summation windows can exist.
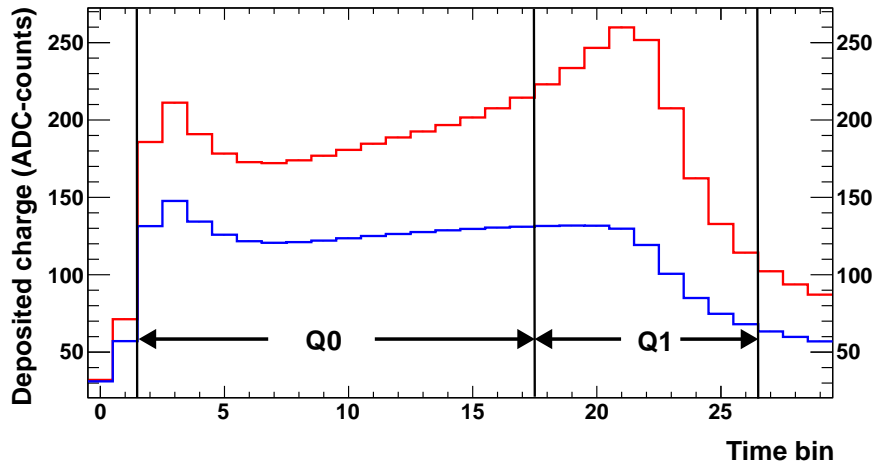
Figure 4.1.: Illustration of the summation windows Q_0 and Q_1 for typical average pulse heights of electrons (red) and pions (blue). The data stems from simulations. In this example, Q_0 covers the time bins 2-17, i.e. mainly the plateau, and Q_1 the TR peak of the electrons around time bins 18-26.

In the following, only the LQ method will be considered. There are several reasons to do so: First, the LQ method and its analysis are easy and comprehensible.

Second, the 2D LQ method requires 2-dimensional LUTs. To get a comparable quality/granularity of the LUT as in the 1-dimensional case, the number of entries is squared. This results in the demand of having a squared number of statistics, which is difficult to achieve in data, especially for electrons (in simulations, it is easily possible, but requires a lot of CPU time). Another important point is that the complexity increases dramatically, since now the start and end points of two summation windows need to be adjusted.
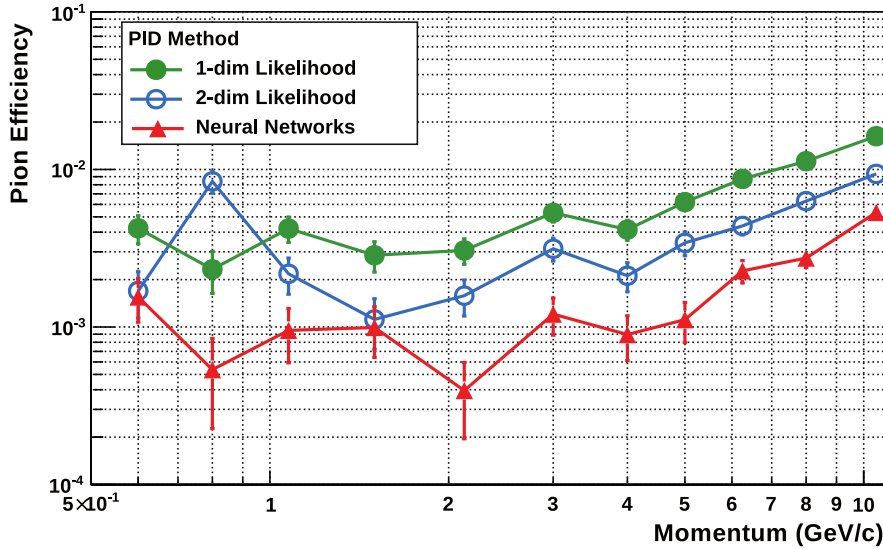
Figure 4.2.: Pion efficiency as a function of momentum for 3 PID methods in simulations for the offline case: 1-dim likelihood (green dots), 2-dim likelihood (blue circles) and neural networks (red triangles) [43].

It is also possible to use Neural Networks (NN) to combine the input of n (with $n \geq 2$) summation windows $Q_0, \ldots, Q_{n-1}$. Indeed, it has been found in the offline case [43] that the best PID performance is achieved with NN, followed by 2D LQ, and is worst for LQ (see Fig. 4.2). For instance, in case of $n = 2$, there would be less statistics required to train the NN than for producing the 2-dimensional LUT as described above. However, it is not well understood how the NNs get to their result. In order to avoid such unknown factors and to keep it as simple and traceable as possible, the LQ method has been chosen for offline PID, until more experience has been gained. The same strategy is used online to have comparability to offline and for the sake of complexity reduction.

In order to create the LUTs and to test the PID performance, the particle identity needs to be known. Thus, the charges Q_0 and Q_1 can be obtained either by simulations, where the real particle identity is available in the Monte Carlo (MC) information, by test beam data, where the real particle identity is also known, or by normal beam data, where the real particle identity can be inferred from the V^0-finder (refer to [58] for further details).

For the LQ method, the LUT is one-dimensional, each entry containing the electron likelihood for a given Q_0. The LUT is calculated as follows: First, the Q_0 distributions of each particle species are normalised such that the sum of all bin contents is unity (see Fig. 4.3). Then, each Q_0 bin of the LUT is the corresponding bin content of the electron's Q_0 distribution divided by the sum of the corresponding bin contents of all considered particle species. An example for the resulting LUT is depicted in Fig. 4.4.

The obtained LUT can be loaded directly into the MCMs (either in the real ones or in the MCM simulation). The MCMs determine the Q_0's of the tracklets and use the LUT to look up the corresponding electron likelihood, that is afterwards stored in the tracklet word. Finally, the GTU (or the GTU simulation) uses this information to combine the electron likelihood of the tracklets to the one of the track. If the track electron likelihood is above some threshold, that can be adjusted at will but is fixed then, the track is flagged as an electron track. Note that these steps can also be done in the simulation: There is a MCM and a GTU simulation, both imitating the hardware as realistic as possible (e.g. same number of decimal places).

There are different ways of how the combination of the tracklet electron likelihoods can be performed. Let L_i be the electron likelihood of the i-th tracklet of a track and L_t the electron likelihood of a track with n tracklets:

The **summation method** uses the average electron likelihood of the tracklets for L_t:

$$L_t := \sum_i L_i/n. \tag{4.1}$$

For the **multiplication method**, L_t is defined as:

$$L_t := \sqrt[n]{\prod_i L_i}. \tag{4.2}$$

Unfortunately, the **likelihood method**, which, in general, gives the best PID performance (see section 5.4), is presumably not feasible online for time reasons. For this method, L_t is:

$$L_t := \frac{\prod_i L_i}{\prod_i L_i + \prod_i (1 - L_i)}. \tag{4.3}$$

This thesis will investigate the online PID performance of all three methods.

4.2. The Analysis Strategy

The primary goal of this thesis is to investigate the influence of several parameters on the PID: gas gain, drift velocity, tail cancellation, summation window (LQ method, cf. section 4.1.2), choice of electron efficiency, choice of GTU combination method (see Eqs. 4.1-4.3) and others.
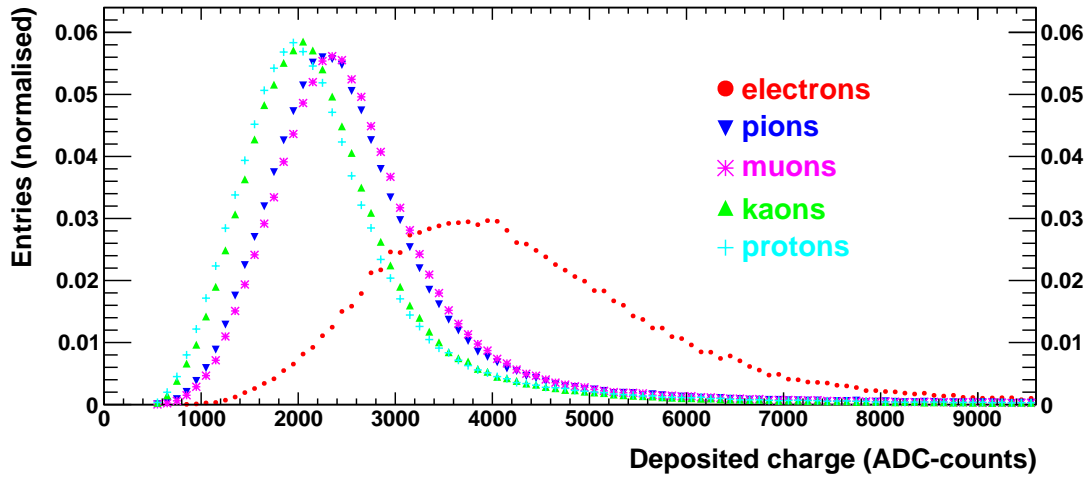
Figure 4.3.: Example for (normalised) Q_0 distributions of different particle species for summation over the time bins 2-26. The data stems from simulations of 3 GeV/c particles. In this case, the tail cancellation is switched off and the standard set of cuts has been applied (see section 4.5). The electrons are shown in red, pions in blue, muons in magenta, kaons in green and protons in cyan. As can be seen, the electrons are separated from the other species.
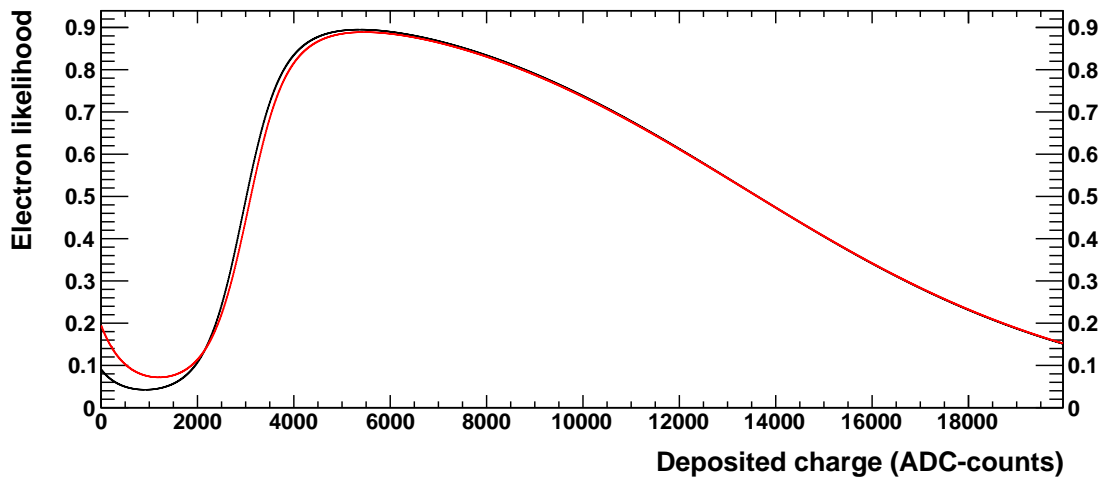
Figure 4.4.: Example for LUTs obtained from the charge distributions in Fig. 4.3[a] taking into account only electrons and pions (red) or all species (black). The charge distributions of non-electrons are very similar, hence the LUTs are almost the same.

_____

[a]Practically, the charge distributions are fitted first (see section 4.6). Then, the fits are used for the calculation of the LUT.

In principle, these parameters could be adjusted and tested at will with the detector (maybe using test beams) to explore their influence on the PID. However, this would be a very involved and time consuming task, since it is required to gather sufficient statistics for every case. That is why it is reasonable to rely on simulations, that have been tuned to reproduce the test beam data [61] pretty well [62]. Furthermore, in simulations, it is possible to investigate the influence of the parameters separately, to clearly identify the influence and to find the relative changes of the PID performance quantities. The analysis of the PID performance for real data will be carried out in [63].

The idea is to divide the analysis in 3 stages: digits, tracklets and GTU tracks stage.

Digits Stage

As explained in section 1.7, the digits are situated almost at the end of the AliRoot simulation chain and are close to the real detector output. In addition, it is possible to use the full Monte Carlo information and relate every digit to the particles that contributed to it.

Since the digits together with the MC information provide the full information, they can be used to perform all desired cuts, even cuts on pad row crossing — this is only possible at this stage, since less information is available at later stages. Pad row crossing means that a tracklet extends over different pad rows. The problem is that the electronics is not capable of merging the charge deposition of both pad rows. This means that the charge deposition in one pad row gets lost for subsequent processing, thus, leading to a reduced tracklet charge.

For this analysis, an individual cluster finder for the digits has been developed in order to be able to handle pad row crossing[1]. The clusters are then used to build tracklets and, finally, tracks. This is done at Monte Carlo level and should not be confused with the reconstruction algorithms of AliRoot. The code for the latter two steps has been developed within the thesis of Uwe Westerhoff [63].

Tracklets Stage

The next step is to get closer to the hardware, i.e. same number of decimal places, same number of bits for each variable and so on. Furthermore, the tail cancellation can be applied to the input data. To do so, the digits are loaded into the MCM simulation, where they are used to find and build tracklets. Additionally, a suitably converted LUT can be loaded, which is then used to store the electron likelihood in the tracklet word.

There are several parameters for the MCM simulator that need to be adjusted. A list of these parameters and a short description can be found in appendix B.

---

[1]Note that the MCM (simulation) is not capable of detecting pad row crossing and merging the deposited charges of the corresponding pad rows.

Besides other settings, the summation windows for Q_0 and Q_1 need to be defined (the latter has not been used so far, but is already implemented to be able to use 2D LQ in future). The information about both charges is included in the tracklet.

The prize to pay for the hardware-like output is that quite some information gets lost. In particular, there is no information about pad row crossing available anymore. As an additional step, the tracklets from the MCM simulation can be assigned to those of the digits and, therefore, to the tracks of the digits by requiring that the tracklets of both stages are close in position.

However, it is possible that the MCM simulation (and this is also true for the real MCMs) finds a tracklet twice in different ADC-channels (cf. section 2.5). To handle this issue, the GTU behaviour is mimicked, i.e. the (first) tracklet with the lowest z value or, if the z values are equal, the tracklet with the lower y value is taken. This is only a simple approximation of the much more complex real GTU behaviour, but should yield similar results. In particular, the results for this simple implementation are easier to understand and the complexity is reduced.

GTU Tracks Stage

Finally, the tracklets from the MCM simulation can be used as input for the GTU simulation. For these tracklets, no cuts except for those performed by the GTU itself are applied. The GTU simulation uses another set of parameters, that can be found in appendix C. Again, this gives a close-to-hardware output, i.e. GTU tracks. Nevertheless, the additional step at the tracklets stage (MCM tracklets assigned to tracks from the digits stage) is reasonable for 3 reasons: First, the complexity is reduced, if the GTU simulation is not used. In particular, the additional analysis step will be independent of the GTU parameters. Second, there is more control on the data set, since the tracklets of each track are selected by controllable cuts instead of the rather complex GTU matching. Finally, it is expected that the results for both analysis steps should agree because there are cuts applied in the additional step at the tracklets stage that are comparable to the matching of the GTU.

In summary, the tracklets together with the information of the digits for advanced cuts are used to create the LUT. This LUT is then used at the following analysis stages. Afterwards, the tracklets are used with fewer cuts for PID performance, namely only with those cuts that can be applied in hardware. In a final step, the PID performance is carried out with the GTU tracks for comparison.

Note that at all analysis stages only primary particles (known from MC information) are taken into account. The impact of secondaries will be discussed in section 5.12.

The code for this analysis has been developed by Uwe Westerhoff [63] and is also capable to handle real data. It has been added to the class package *AliTRDonlinePID* and will be integrated into the AliRoot framework as soon as possible.

4.3. Simulations – Creation of Data Sets

As stated before, simulations are used to produce the data sets for the analysis in this thesis. For these simulations, the following settings have been used:

- 10^4 events for each particle species ($e^\pm$, $\pi^\pm$, $p^\pm$, $\mu^\pm$, $K^\pm$) are generated with 5 particles + 5 anti-particles for each event[2].

- The momentum is fixed to 3 GeV/c and (for another data set) to 5 GeV/c.

- The pseudo-rapidity is limited to $\eta \in [-0.1, +0.1]$.

- 30 time bins are used for the TRD readout.

The idea is to investigate the PID performance for very pure signals with an ideal detector (no malfunctioning chambers, uniform gain and drift velocity for all pads and chambers etc.). For this purpose, only 10 primaries are generated in each event to avoid effects of overlapping tracks and pad sharing. The small η range has been chosen to avoid effects of different tracklet length (this aspect is discussed in section 5.12); especially, almost all tracks will traverse the central stack. This allows for abandoning the tilt correction besides the tracklet length corrections, thus, reducing complexity.

The current (summer 2011) number of time bins for the TRD readout is 27 and this number will possibly further decrease in order to be able to send an L1 trigger signal in time (see section 1.6 and chapter 6). However, 30 time bins have been used for the simulation, since this was the setting for runs in 2010. The latter data is extensively studied at the moment [63], hence, it is very beneficial to be able to compare the simulation results with these analyses.

The nominal gas gain has been chosen to obtain a signal-to-noise ratio above 40 [64]. Test beam measurements [65] showed that this condition is realised for a gas gain around 4000. Therefore, the nominal gas gain has been set to 4000.

To examine the influence of the gas gain on the PID performance, the gas gains 3600, 4000, 4200 and 4400 have been simulated, i.e. 90%, 100%, 105% and 110%, respectively. For these gains, the drift velocity has been set to the nominal value of 1.5 cm/μs [66]. Since the drift velocity may vary between 1.4 cm/μs and

---

[2]It turned out that this statistics did not improve the results that can be obtained for 2000 events. The results agree within the errors. Consequently, 2000 events contain already sufficient statistics to obtain the results that are stated in the following.

1.6 cm/μs in time [66], these three drift velocities (1.4, 1.5 and 1.6 cm/μs) have been simulated for the nominal gas gain 4000 to investigate the impact of the drift velocity on the PID performance.

To understand the choice of the mentioned gas gains, the relation between gas gain, G, and pressure, P, can be considered. According to [67], these quantities are related for the ALICE TRD as:

$$\frac{\Delta G/G}{\Delta P/P} \approx -5. \tag{4.4}$$

Pursuant to [68], the factor should theoretically be in the region -5 to -8. The pressure inside the detector is directly connected to the atmospheric pressure at CERN[3]. Over the year, most of the pressure changes are covered by $\Delta P/P = \pm 3\%$ [69]. This implies that the gas gain may vary by $\pm 15\%$ or (with respect to the theoretical value) even higher. Hence, it is reasonable to study gas gains in the $\pm 10\%$ region around 4000 and maybe extrapolate to stronger fluctuations.

The justification for the choice of 3.0 GeV/c particles is given by the following deliberation: As mentioned in chapter 2, the yield of transition radiation photons starts to saturate at 3.0 GeV/c for electrons. On the other hand, the dE/dx is rather flat for electrons at this momentum, but increases for other particles, in particular for pions (cf. Fig. 1.7, p. 14). This means that the e/π-separation is expected to be very good at 3.0 GeV/c and to get worse for higher momenta. Fig. 4.2 (p. 61) suggests an even better e/π-separation for lower momenta, which is mostly related to the dE/dx trends. Yet, the TRD becomes important for momentum regions where dE/dx alone is not sufficient anymore, i.e. somewhere around 3 GeV/c (cf. Fig. 1.7, p. 14). With respect to a rare TRD L1 trigger, e.g. on single electrons, it makes sense to trigger on not too low momenta. Therefore, 3.0 GeV/c appears to be a reasonable choice.

The second data set with 5.0 GeV/c particles is important for extrapolations to higher momenta. For Υ physics, the electrons from the corresponding decays will be in the region of 5 GeV/c. Consequently, it is advantageous to investigate the PID performance for particles with such momenta.

Finally, it must be taken into account that the central stack is missing in sectors 13, 14 and 15 (see section 2.2). Due to the η restriction, almost all particles will traverse the central stacks. As a result, at most a fraction of $15/18 \approx 83\%$ of the generated particles can be detected by the TRD. Due to scattering and some quality cuts, roughly $7 \cdot 10^4$ particles (including anti-particles) are available for the analysis for each particle species.

---

[3]The pressure difference between inside and outside of the detector is kept constant, but not the absolute value of the pressure.

4.4. Correlation between ADC-signal and Gas Gain

In this section, it will be demonstrated that the simulation of the discrete gas gains mentioned earlier is indeed sufficient to get estimates for the PID performance in the whole gas gain range from 90% to 110%, where 100% corresponds to the nominal gas gain 4000. Another purpose is to justify that the simulations really yield reasonable results. For such a demonstration, it is convenient to study the correlation between the ADC-signal and the gas gain. This is possible by comparing the average pulse heights of the particle species for different gas gains. Of course, it is desired to find this correlation only for particles that fulfil some quality criteria. Therefore, the same cuts as for the data sets for the PID performance (see section 4.5) are used. The analysis is carried out for the digits stage with these cuts, since the clean signal of primary particles without introducing any (hardware) inefficiencies or impurities is of interest. Another reason is to reduce the complexity as much as possible in order to keep the interpretation of the results simple.
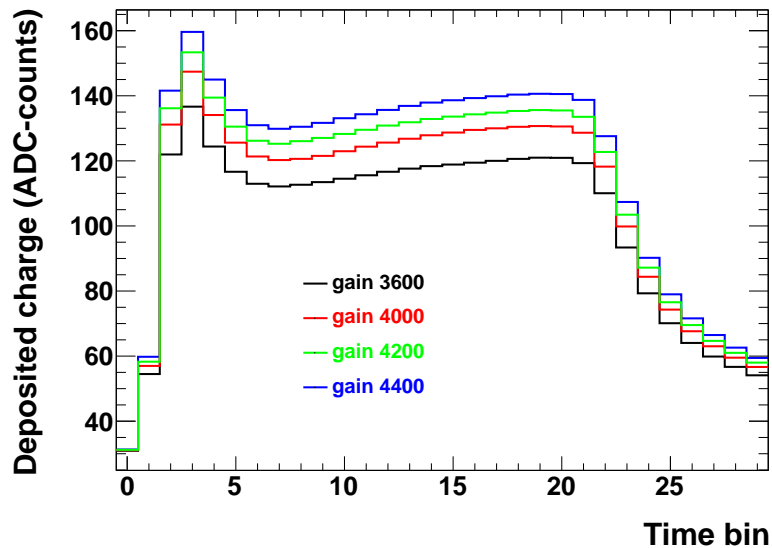
Figure 4.5.: Average pulse height of pions for different gas gains. The amplification peak and the plateau region are clearly visible.

The average pulse height of pions for different gas gains is depicted in Fig. 4.5. A naive expectation is a linear correlation between the ADC-signal and the gas gain. If this is true, it will be possible to scale the average pulse heights for the various gas gains such that they lie on top of each other. To calculate the scale factors, the following steps are performed:

1. To increase the statistics, the signal is summed over a range of time bins for each gas gain. This range is chosen to cover the plateau, i.e. time bins 6 to 20, because the signal is expected to be rather stable there.

2. The plot of the summed ADC-signal as a function of the gas gain is fitted with a linear function. The obtained fit parameters can be interpreted relatively easily. They can be used to check, if the results are reasonable and if the hypothesis of a linear correlation holds.

3. The ratios of the ADC-signals of gas gain 4000 with respect to those of other gas gains are calculated to obtain the scale factors and the inverse scale factors. To get extrapolations for all gas gains in the considered range, i.e. to get the inverse scale factor as a function of the (relative) gas gain, the obtained inverse scale factors are fitted.

   Note that this function can also be calculated with the help of the parameters resulting from the previous step. However, this method requires a more complicated error propagation. As has been checked, the results for both methods agree within the errors obtained in the third step.
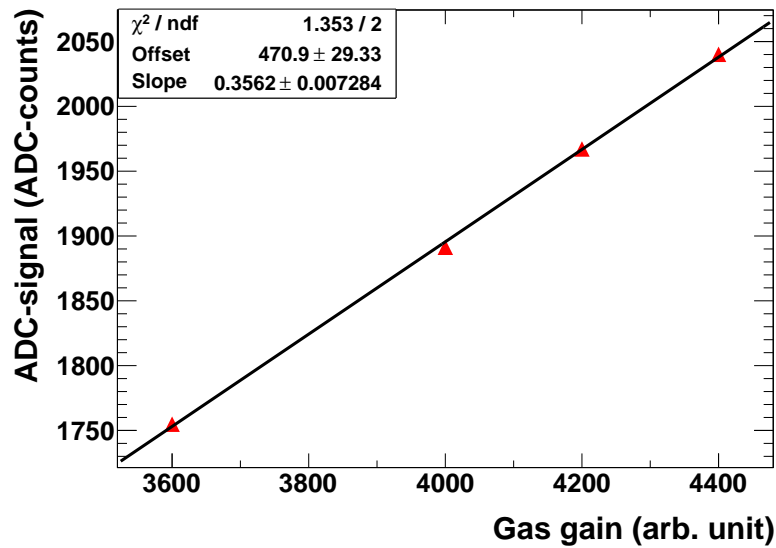
Figure 4.6.: Linear fit of the summed ADC-signal as a function of the gas gain for pions. The red triangles indicate the data points and the black line shows the fit through these points. The (small) statistical error bars are not visible. The fit results for other species can be found in Tab. 4.1.

The results of the second step are shown in Fig. 4.6 for pions and Tab. 4.1 lists the corresponding results for all particle species. According to the relatively small reduced χ^2's, the assumption of a linear correlation between ADC-signal and gas gain is confirmed, but the errors seem to be a bit overestimated.

Species	Offset	Slope	χ^2 / NDF
Electrons	483 ± 41	0.615 ± 0.010	$1.08/2$
Muons	476 ± 27	0.3598 ± 0.0066	$0.13/2$
Pions	471 ± 29	0.3562 ± 0.0073	$1.35/2$
Kaons	459 ± 29	0.3178 ± 0.0072	$0.20/2$
Protons	426 ± 29	0.3259 ± 0.0073	$0.08/2$

Table 4.1.: Summary of the results for the fits of the summed ADC-signal as a function of the gas gain for different species.

Furthermore, the obtained slopes and offsets look quite reasonable: The gas gain is a measure of the signal amplification. At zero gas gain, i.e. there is no amplification, it is naively expected to see no signal from particles, but only the baseline (cf. section 2.3: *pedestal correction*). The baseline is 10 for every pad, the signals of 3 pads are summed for every time bin and, for this analysis, the sum of 15 time bins (time bins 6 to 20) is considered. Consequently, an ADC-signal of about $10 \cdot 3 \cdot 15 = 450$ is expected, which is indeed observed within the errors.

Next, the slope is proportional to the number of primarily ionised gas particles. The more of these particles are created, the more the signal can be amplified. As a result, the slope gets steeper with increasing number of primarily ionised gas particles. A glance back on Fig. 1.7 (p. 14) gives a rough estimate for the dE/dx at 3 GeV/c for different species. Taking into account the TR in case of electrons, the steepest slope is expected for electrons and similar, but smaller slopes for muons (not shown in the figure, but similar mass as pions) and pions. Kaons and protons should have the smallest slope. Obviously, the found values in Tab. 4.1 are in agreement with this anticipation.

Turning to the next point of the procedure, the ADC-signal at gas gain 4000 can be divided by the ADC-signal at gas gain x to obtain the corresponding Scale Factor (SF) for gas gain x:

$$SF(x) \equiv ADC_{\text{summed}}(4000)/ADC_{\text{summed}}(x). \tag{4.5}$$

Afterwards, the average pulse heights for the different gas gains can be scaled with these factors, as shown in Fig. 4.7a. Qualitatively, the scaling holds. Finally, the relative deviation from the ADC-signal of gas gain 4000 depicted in Fig. 4.7b shows the quantitative agreement with the scaling assumption. The figure also suggests that the signals are indeed more or less stable in the plateau region (denoted by the magenta lines), i.e. the relative deviation of the ADC-signal from that of the reference gas gain 4000 is smaller than 1%. At the very first and very last time bins, the relative deviations strongly increase because the ADC-signal gets small and is close to the baseline (cf. Fig. 4.7a).

To sum up, the simulations yield reasonable results.
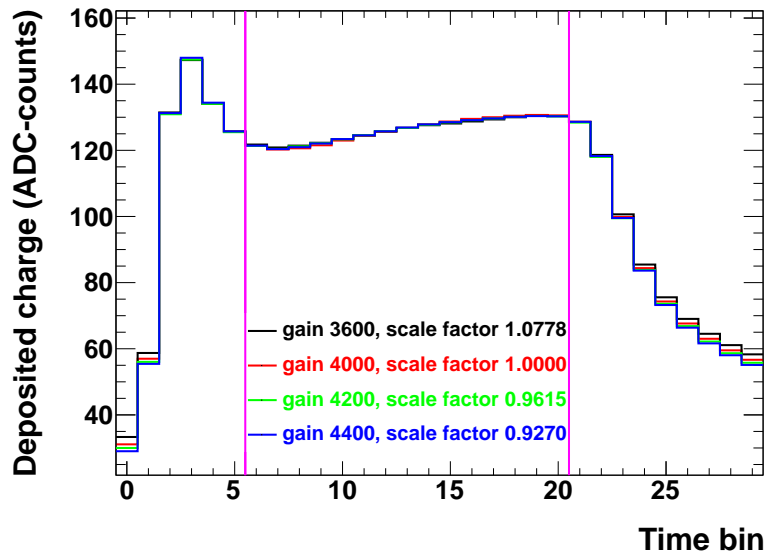
(a) Scaled average pulse heights
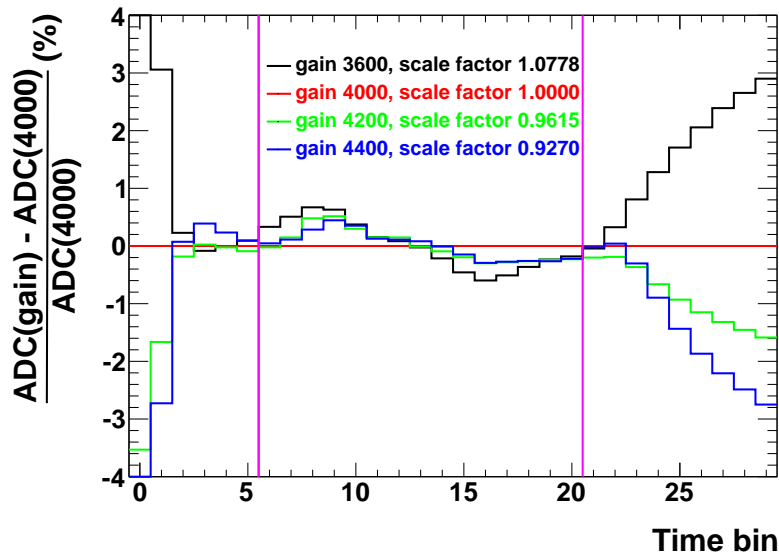
(b) Relative deviation of the scaled average pulse heights with respect to nominal gas gain 4000

Figure 4.7.: Scaled average pulse heights of pions for different gas gains. The magenta lines show the limits of the time bin range (time bins 6-20) that have been used to calculate the scale factors. The nominal gas gain 4000 has been chosen as reference. Note that the large relative deviations at early and late time bins are caused by the small signal in these regions.

However, there is still an open issue: How can the PID performance in a range around the nominal gas gain be estimated? The idea is to consider the Inverse Scale Factors (ISF) as a function of the relative gas gain, $SF^{-1}(x)$. The ISF at gas gain fraction x with respect to gas gain 4000 states the corresponding fraction of the ADC-signal. Taking into account the previous results, the ISF should be a linear function of the relative gas gain. If the slopes of the ISFs of all species are not too different, this would mean that the deposited charge in each time bin changes in a similar way with the gas gain for each species. In this case, it would be sufficient to simulate only one gas gain in the considered region. Afterwards, at the digits stage, the deposited charge in each time bin can be scaled and used to investigate a different gas gain at all 3 analysis stages. It will be shown in the following that the scaling is approximately satisfied.
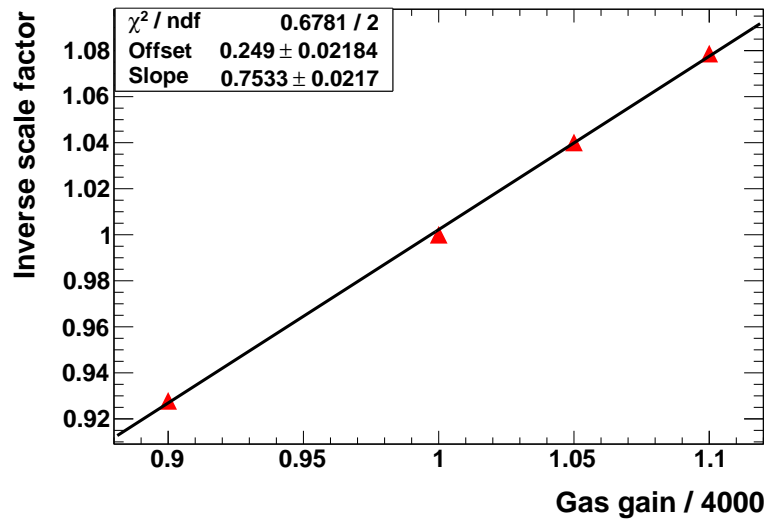
Figure 4.8.: Inverse scale factor as a function of the relative gas gain for pions. The red triangles are the calculated inverse scale factors from the data, the black line is a linear fit through these points. The (small) statistical error bars are not visible. The fit results for other species are listed in Tab. 4.2

Fig. 4.8 shows the result for the ISF fit for pions. The errors of the data points (red triangles) are calculated using the following strategy: The error of the average pulse height's bin content is just the statistical error. Due to ion tails, the ADC-signal of different time bins is correlated and, thus, the error as well. That is why for the summed ADC-signal, ADC_{summed}, the errors of the contributing bins are just added up instead of taking the square root of the sum of squares. The corresponding errors are referred to as $\Delta ADC_{\mathrm{summed}}$ in the following. Applying error propagation (cf. [70]) to Eq. 4.5 yields for the errors of the (inverse) scale factor:

$$\Delta SF(x) = SF(x) \cdot \sqrt{\left(\frac{\Delta ADC_{\text{summed}}(x)}{ADC_{\text{summed}}(x)}\right)^2 + \left(\frac{\Delta ADC_{\text{summed}}(4000)}{ADC_{\text{summed}}(4000)}\right)^2}, \quad (4.6)$$

$$\Delta SF^{-1}(x) = (SF^{-1}(x))^2 \cdot |\Delta SF(x)|,$$

where $SF(x)$ and $SF^{-1}(x)$ are considered as functions of the gas gain x.

Species	Offset	Slope	χ^2 / NDF
Electrons	0.164 ± 0.020	0.836 ± 0.020	$0.54/2$
Muons	0.249 ± 0.020	0.751 ± 0.020	$0.06/2$
Pions	0.249 ± 0.022	0.753 ± 0.022	$0.68/2$
Kaons	0.265 ± 0.024	0.734 ± 0.024	$0.10/2$
Protons	0.246 ± 0.024	0.754 ± 0.024	$0.04/2$

Table 4.2.: Summary of the results for the fits of the inverse scale factor as a function of the relative gas gain for the different species.

As listed in Tab. 4.2, the slopes of all particle species agree within 10%. They are not exactly the same because, due to different dE/dx (and TR), the relative contribution of the baseline to the ADC-signal of the particle species is different. This finally leads to a slope of the ISF smaller than 1 because the fraction of the deposited charge in numerator and denominator of Eq. 4.5 (p. 70) decreases with increasing baseline, which results in a weaker dependence of the (I)SF on the gas gain. It was checked that these slopes are all in agreement with 1, if the baseline is subtracted from the average pulse height. All this is another indicator that the simulations fit the expectations.

The approximate agreement of the slopes justifies the scaling assumption in the examined range of $\pm 10\%$ gas gain change. Note that these conclusions have been confirmed for 5.0 GeV/c data.

4.5. Cuts for Clean Samples

As stated before, the aim is a good PID performance for particles that are interesting for triggering: The PID should work for particles that have not been scattered too much and that have sufficiently high momentum. This means that the LUT should be tuned to handle such "good" particles. In the simulation, the tuning can be achieved by using the digits together with MC information to perform cuts.

For each interaction of a track, a track reference point is created with the full set of information. In general, there is a pair of track reference points for a particle traversing a TRD chamber: one at the first and another one at the last

energy deposition. Looping over the track reference points of a track starting at the vertex and respecting the chronological order, the following cuts can be applied:

- only primary particles (via MC ID)

- $p \geq 1.0$ GeV/c

- radius of track reference points must increase

- track reference must belong to the TRD

- angle between momentum vectors of subsequent track reference points must be $\leq 3.35°$

- the local distance in x, Δx_{local}, of two track reference points in the same chamber must be 0.5 cm $\leq \Delta x \leq 5$ cm

- the deflection length $(\Delta y_{\text{local}}/\Delta x_{\text{local}}) \cdot 3$ must be ≤ 1 cm (the factor 3 corresponds to the drift length of 3 cm)
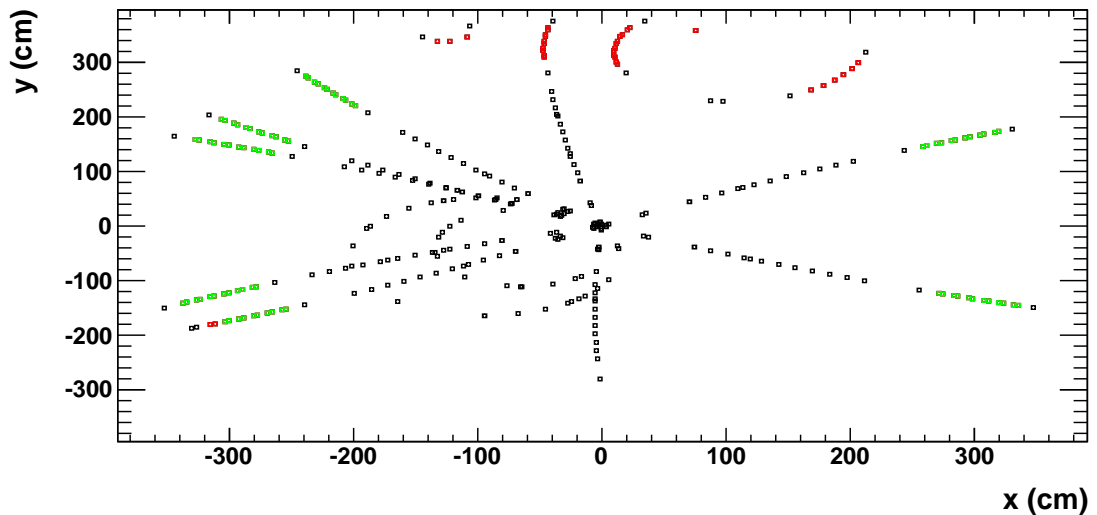
Figure 4.9.: Effect of cuts on the track reference points. The figure displays the projection of the track reference points onto the x-y plane for a single (simulated) event. All colours together give the full set of track reference points for all tracks, the green and red points depict track reference points in the TRD. Only the green points are accepted by the quality cuts.

Altogether, these cuts ensure that, on MC basis, only "good" tracklets are selected via the corresponding pair of track reference points. The threshold for the angle between the momentum vectors (fifth cut of the list) has been chosen such that a particle with minimum momentum of 1 GeV/c flying radially outwards

exactly passes the cut. But particles that underwent scattering will be rejected. The effect of this list of cuts can be clearly seen in Fig. 4.9: It shows the projection of the position of the track reference points onto the x-y plane. The green points are accepted by the cuts, the red ones are rejected and the black points belong to detector parts different from the TRD. It can be seen in the upper part of the figure that some particles scatter, loose energy, leave the detector, are then bent back into the detector by the magnetic field and again interact with the detector. Actually, it was checked that this happens rather frequently, namely in about 5% of the cases (confirmed in [71]). It is not desired to do PID for such particles or particles that have already been scattered much before reaching the TRD. It is expected that the GTU will sort out these particles anyway because the matching should fail for these. Therefore, these particles are removed completely from this analysis, i.e. the first list of cuts is used for the digits and the tracklets stage, while, at the third analysis stage, it is "replaced" by the GTU simulation. In conclusion, the figure shows that a reasonable set of track reference point pairs is selected by the cuts.

Finally, a second set of cuts is applied to select the candidates for the LUT creation:

- only clusters that originate uniquely from one particle (no shared clusters)

- only tracklets for which the corresponding tracklet of the MCM simulation has been found

- only tracklets without pad row crossing

- only tracks with at least 4 tracklets passing the cuts in the same stack

Note that the MCM simulation already demands a minimum number of clusters for a tracklet (cf. appendix B). Thus, the second cut is also an implicit cut on the number of clusters per tracklet.

For the PID performance, the second list of cuts consists only of the second and the fourth cut, namely those cuts that can (and are) also be applied in hardware. In addition, the full first list of cuts is used.

For the analysis stage using the GTU tracks, there are even no further cuts applied (i.e. neither the first nor the second list of cuts), except for those performed directly in the GTU simulation. Basically, this is a cut on at least 4 matched tracklets in the same stack.

4.6. Look-Up Table Creation

After the data sets have been cleaned up with the quality cuts, it is now possible to use them for the LUT creation. As stated in section 4.1.2, this thesis will only discuss the one-dimensional likelihood method (LQ). Consequently, only one

summation window needs to be adjusted. As Fig. 4.1 (p. 60) suggests, time bins 0 and 1 mainly contain noise[4] and, therefore, will be excluded from the summation window Q_0. At the time of writing this thesis, the number of time bins has been 27, i.e. time bin 26 would be the last one[5]. Thus, one examined summation window is that ranging from time bin 2 to 26. In order to investigate the influence of the summation window on the PID, the range 2 to 21 will also be analysed, i.e. only a fraction of the signal is taken into account. This window corresponds to the time bin range that is used in the MCM simulation to fit the tracklets (see appendix B).
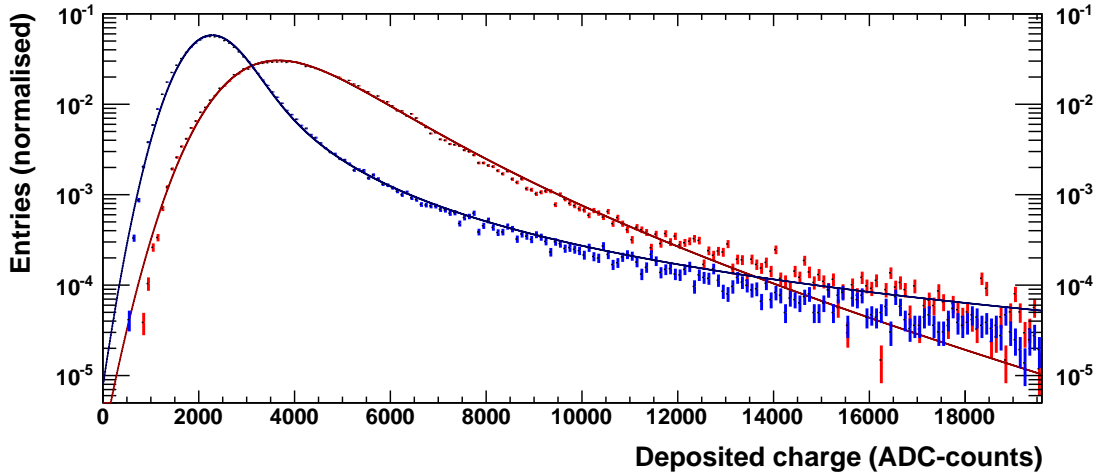
Figure 4.10.: Fits of the (normalised) Q_0 distributions of electrons (red) and pions (blue) for summation over time bins 2-26. In this case, the tail cancellation is switched off and the standard set of cuts has been applied (see section 4.5). The fits are indicated by the dark red line for electrons and by the dark blue line for pions, respectively.

After adjusting the summation window and performing the cuts, a histogram with the deposited charge distribution can be created and normalised (see Fig. 4.3, p. 63). However, there will be a lot of fluctuations and no smooth shape due to poor statistics for high charge depositions (this is, in particular, true for real data sets) — fortunately, high charge depositions are rather rare and have only a small influence on the PID. To get a smooth distribution, a complex fitting procedure has been developed [72]. The final fitting function is a Landau distribution multiplied by an exponential factor convoluted with a Gaussian and normalised by a factor n:

$$(n \cdot \mathrm{Exp} \cdot \mathrm{Landau}) \otimes \mathrm{Gauss}. \tag{4.7}$$

---

[4]Note that the baseline contributes 30 to each time bin because the ADC-signals of 3 pads are summed.

[5]The same strategy is pursued for 2010 data, where also, as in the simulation, 30 time bins are available. The last time bins mainly contain the baseline.

The Landau distribution describes the fluctuation of the particle's energy loss around a given expected value. Here, it is normalised (divided by sigma) and has 2 parameters: the width and the most probable value. The expected value of the energy loss is calculated with the exponential factor (with one parameter), while the Gaussian smears out the energy loss distribution. The Gaussian in the convolution is normalised (divided by sigma) and has only sigma as a parameter. Finally, there is a normalisation constant n as an additional parameter. Overall, there are 5 parameters used for the fitting.

The fitting procedure is divided into 3 steps: First, only the Landau distribution is used to fit a small region around the peak of the deposited charge distribution. The obtained parameter values are then used as initial values for the second step of the fitting, where a Landau distribution convoluted with a Gaussian and a slightly broader fit range are used. Finally, in the third step, the values of step 2 are taken as initial values for the fit with Eq. 4.7. The result is shown in Fig. 4.10 for electrons and pions in case of no tail cancellation and summation over time bins 2-26.

The stepwise fitting allows for an automatic determination of proper initial values of the fit parameters and results in a relatively robust fitting procedure. However, especially in real data the statistics gets pretty low for high charge depositions (e.g. around 12000 in Fig. 4.10). In some cases, the fit does not describe the data well in this high-charge region, but with respect to the low statistics, it is anyway questionable if the fit is trustful there. Fortunately, this does not pose too much harm, since, in general, less than 1% of the particles lie in this region. The same holds for very low charge depositions (for instance < 1000 for electrons and < 600 for pions in Fig. 4.10).

4.7. Comparison of the Data at Different Analysis Stages

Before the results for the PID performance are presented in chapter 5, a few expectations concerning the special properties of the different analysis stages are discussed in this section.

First of all, the difference between the pure digits and the tracklets from the MCM simulation can be inferred from Fig. 4.11: The ADC-signal (from the digits) is encoded by the colours and shown as a function of the time bin and the ADC-channel. The MCM simulation finds hits (black stars) for this input and, finally, performs a straight line fit for the tracklet (red line). As stated in section 2.3, only two channels can contribute to a tracklet, in this case, the channels 3 and 4. However, the figure shows a short fluctuation of the signal and, therefore, the hits in time bins 20 to 24 are shifted to channel 5. In detail, there will be two tracklets found, one in channels 3 and 4 and another in channels 4 and 5. The GTU will select only one of these tracklets (see section 2.5), in this case, the one in channels
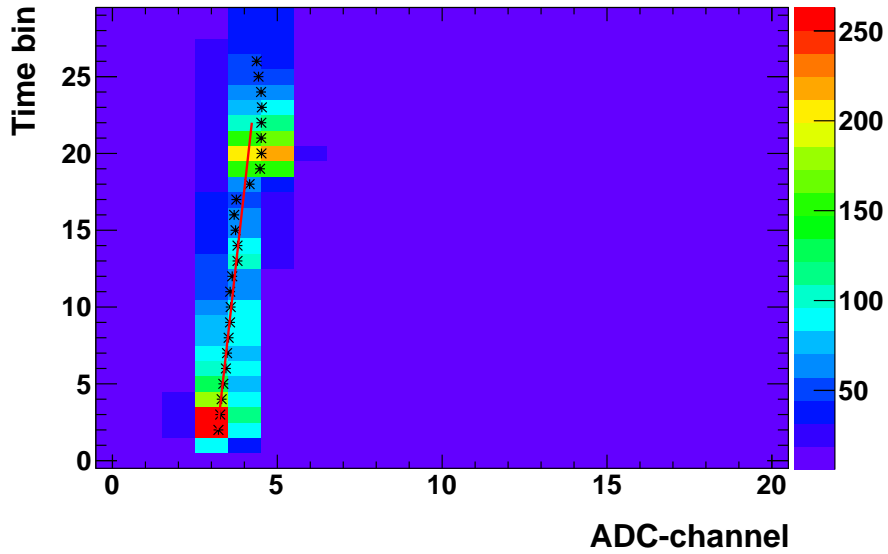
Figure 4.11.: Example for MCM hits for a given ADC-signal. The colours indicate the ADC-signal at a given time bin (ordinate) and for the corresponding ADC-channel (abscissa). The black stars visualise the found hits and the red line shows the straight line fit of the tracklet (time bins 2 to 21). Only 2 ADC-channels can contribute to a tracklet, in this case, the channels 3 and 4. Hence, the hits of the short fluctuation to channel 5 in time bins 20 to 24 are declined.

3 and 4. This results in a "loss" of hits and deposited charge compared to the digits stage, in which no restriction on channels exists. An immediate implication is that the digits stage cannot be used for PID performance studies, since it does not respect the hardware structure. Hence, the need of the tracklets stage is justified[6]. However, the digits can perfectly be used for cuts, where the readout details are not that important.

Furthermore, pad row crossing (cf. section 4.2) can be detected at the digits stage and the charge of both affected pad rows can be taken into account. On the contrary, the charge of one pad row is "lost" at the tracklets stage, since there is no information shared between pad rows.

Fig. 4.12a schematically illustrates a similar case as in Fig. 4.11, but without the fluctuation of the signal to channel 5. The big red dots symbolise hits along the detected particle trajectory (black line) and the dotted red lines indicate that the slowly drifting ion tails of these hits contribute to the signal in later time bins of the same channel. It is possible that there is a sufficient number of hits in channel 4 to find a tracklet in channels 4 and 5 (orange) besides that in channels 3 and 4 (cyan). If the "wrong" tracklet, namely that in channels 4 and 5 (orange),

---

[6]In addition, this stage is needed to explore the effects of the tail cancellation filter, that is applied in the (simulation of the) MCMs.
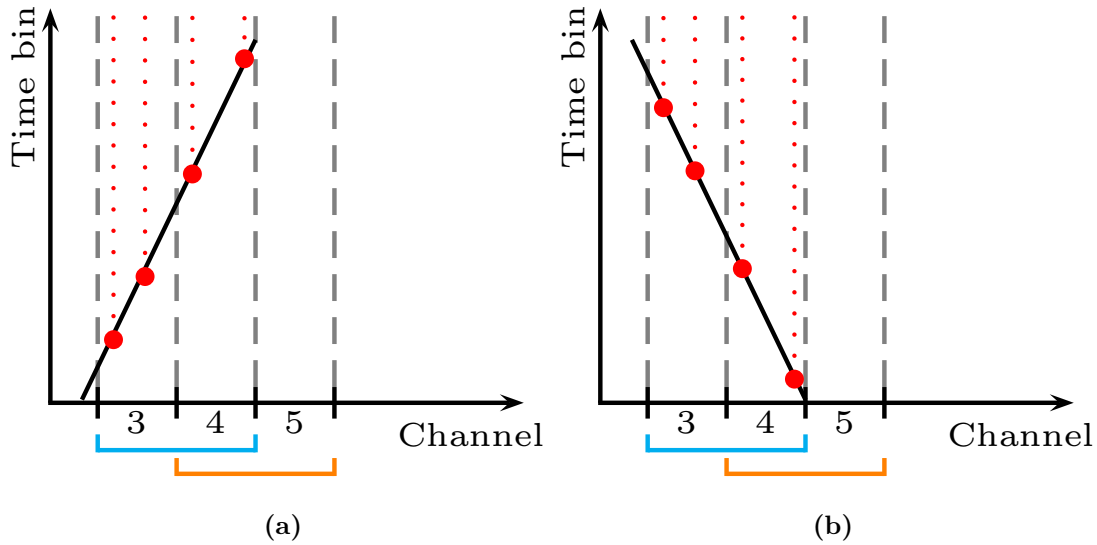
Figure 4.12.: Schematic view of the asymmetric effect of doubly found tracklets. **a)** and **b)** show detected particle trajectories (black lines) with a different sign of the slope. The hits (big red dots) are used to reconstruct the trajectory and the corresponding ion tails of the hits contribute to the signal in later time bins of the same channel (red dotted lines). For a sufficient number of hits in channels 3 and 4, a tracklet can be found in 2 different channel pairs: 3 and 4 (cyan) or 4 and 5 (orange). In the latter case, the hits in channel 3 are missing. However, the ion tails give rise for an asymmetry, which is discussed in the text. Note that effects of the magnetic field are not taken into account in this figure for simplicity.

is selected for the analysis, the hits in early time bins are not taken into account. This means that such *doubly found tracklets* result in a rejection of clusters in early time bins.

A rejection of clusters implies that deposited charge is "lost", which influences the PID performance. This aspect will be discussed in detail in section 5.11.

Vice versa, clusters in the last time bins are rejected due to doubly found tracklets, if the sign of the tracklet's slope is different, as shown in Fig. 4.12b: If the "wrong" channel pair (orange) is selected, the hits of channel 3 are not taken into account. Anyway, the ion tails in channel 4 give some signal in later time bins, so that there might be clusters found in the whole time bin range in channel 4. This gives rise for an asymmetry: *Doubly found tracklets* most likely lead to a cluster rejection in early time bins, but do hardly or not at all affect later ones. Indeed, it was observed that the selection of the wrong tracklets of doubly found pairs leads to a cluster rejection only in time bins 2 to 11, whereby the fraction of rejected clusters decreases approximately linearly from time bin 2 to time bin 11. The asymmetry is enforced by the Lorentz angle introduced by the presence of a magnetic field (see section 2.1), which changes the distributions of the (detected)

tracklet angles (cf. discussion at the end of this section). For the used magnetic field in the simulations, the case in Fig. 4.12a will appear more frequently than that in Fig. 4.12b.

Three methods of handling doubly found tracklets have been compared: the simple GTU imitation as used at the tracklets stage (see section 4.2), the real GTU behaviour from the GTU simulation, and an *ideal* tracklet selection, where the tracklet with the most deposited charge is selected. The rejection of clusters was found to be minimal for the *ideal* selection, as expected. The other two methods exhibit only different results in time bins 2 to 11. Thereby, the cluster rejection is roughly a factor 2 smaller for the real GTU method than for the simple GTU imitation, but still larger than for the *ideal* selection. Hence, the GTU simulation provides a better (but not perfect) handling of doubly found tracklets than the simple GTU imitation.

Returning to Fig. 4.12, the following point is crucial with respect to PID performance: Every cluster contains the baseline in its charge, but this charge is only attributed to the tracklet, if it exceeds some threshold q_t. In Fig. 4.12a, the channel pair indicated in orange does not contain any clusters for early time bins, i.e. these time bins do not contribute any charge (especially no baseline) to the tracklet. In Fig. 4.12b, the ion tails potentially result in cluster charges above the threshold in later time bins of the pair of channels indicated in orange. For these time bins, at least the charge q_t (including the baseline) is attributed to the tracklet. Although this yields a smaller charge than for the channel pair indicated in cyan, the "loss" of charge due to the "wrong" selection is smaller than in Fig. 4.12a.

In conclusion, doubly found tracklets mainly adulterate the deposited charge and, therefore, the PID performance in early time bins for the chosen magnetic field.

This effect is strongly enforced by the impact of the Lorentz angle (cf. Fig. 2.3, p. 24). In the simulation, the magnetic field has been set to -0.5 T, such that the magnetic field and, thus, the Lorentz angle are exactly opposite to those in Fig. 2.3. Note that the y direction of Fig. 2.3 indicates the position, whereas the ordinate in Fig. 4.12 shows the time bin. This means that the situation in Fig. 2.3 qualitatively corresponds to Fig. 4.12b, but with Lorentz angle and magnetic field in the opposite direction.

In summary, the Lorentz deflection for a negative magnetic field causes that situation (a) in Fig. 4.12 occurs much more frequently than situation (b).

5. Online PID Performance Results

In this chapter, the most important analysis results are summarised and discussed. First, the analysis technique is described and some preliminary considerations are presented that are needed for the understanding of the results. Afterwards, the impact of the parameters on the PID performance is investigated for the tracklets stage. The comparison and cross-check with the GTU tracks stage is carried out subsequently. The complete collection of results can be found in appendix D. Ultimately, the simulations are compared to real data.

If not stated otherwise, all results in this chapter have been obtained by taking into account only electrons and pions. This will be indicated by the phrase *only pions*, whereas the phrase *all* means that the 5 most abundant particle species (electrons, pions, muons, kaons and protons) have been considered.

Note that "SW *x-y*" will be used as an abbreviation for the Summation Window (SW) Q_0 ranging over time bins *x-y*.

5.1. The Analysis Technique

The definitions of electron efficiency ε_e and pion efficiency ε_π in section 4.1.1 can be expressed by the following formulas:

$$\varepsilon_e = \frac{\int\limits_{t_e(\varepsilon_e=90\%)}^{1} f^e(p_e)dp_e}{\int\limits_{0}^{1} f^e(p_e)dp_e} \overset{!}{=} 90\%, \tag{5.1}$$

$$\varepsilon_\pi = \frac{\int\limits_{t_e(\varepsilon_e=90\%)}^{1} f^\pi(p_e)dp_e}{\int\limits_{0}^{1} f^\pi(p_e)dp_e}. \tag{5.2}$$

In these formulas, f^e and f^π are the track likelihood distributions to be an electron for electrons and pions[1], respectively. p_e indicates the electron likelihood

---

[1] The phrase *pion* is used as a synonym for *non-electron*. If also other non-electron species are to be considered, f^π has to be replaced by the overall likelihood distribution of these non-electrons. Note that pions are the most abundant particle species in ALICE [58].

of a track, which is integrated over. The lower limit t_e of the integral in the numerator of Eq. 5.1 is chosen such that the electron efficiency ε_e is 90%, i.e. 90% of all electrons are correctly identified as electrons. With this threshold, the pion efficiency ε_π can be calculated with Eq. 5.2 and the pion suppression by taking the inverse.

Practically, the electron likelihoods for the tracks are filled into a histogram, whereby tracks that are known to be electrons and those originating from non-electrons are treated separately. Examples for such histograms for the three different combination methods (summation, multiplication, likelihood, see Eqs. 4.1-4.3 on p. 62) are shown in Fig. 5.1. The electron tracks are plotted in red and those of pions in blue. On the abscissa, the electron likelihood p_e is displayed. Therefore, the histograms represent the binned versions of the likelihood distributions f^e and f^π. The area between the threshold t_e and the upper end of the f^e spectrum, which contains 90% of all electron tracks, is hatched in red. The fraction of pions above the threshold t_e compared to the total number of pions is the pion efficiency ε_π.

To determine t_e, the contents of the bins are summed up for electrons, starting at 100% electron likelihood and stopping, if at least 90% of the electron tracks have been summed up. This bin is then the threshold t_e. Due to the finite bin width, the electron efficiency is usually not exactly 90%. Hence, an uncertainty is introduced by the binning. To estimate this error, the determined threshold is moved one bin to the left and one bin to the right and the corresponding PID performance is calculated. By this method, asymmetric errors are obtained for the electron efficiency and the pion suppression.

Only a single LUT can be loaded into the TRAP chips and only one threshold t_e can be chosen at the same time. Both, threshold and LUT, can be optimised for certain conditions, as drift velocity, gas gain and momentum. For this analysis, the nominal gas gain 4000 and drift velocity 1.5 cm/μs have been chosen for this purpose and the momentum 3.0 GeV/c has been declared as the reference momentum. As in the experiment, LUT and threshold are then kept fixed, even if parameters as e.g. the gas gain and/or the drift velocity change[2], i.e. the same LUT and threshold are applied to various data samples that have been obtained (simulated) for different parameter sets. This allows for the determination of the PID performance under changing conditions. However, LUT and threshold are calculated separately for TC on/off, for the different summation windows and for each combination method, since these settings can be regulated and the corresponding LUT and threshold adjusted, when the detector electronics are configured before data taking[3].

---

[2]Such changes might be caused by outer observables, like the atmospheric pressure, that cannot be controlled.

[3]Of course, the combination method is implemented in hardware and will be chosen only once, if the optimal method has been found.

(a) Likelihood

(b) Summation
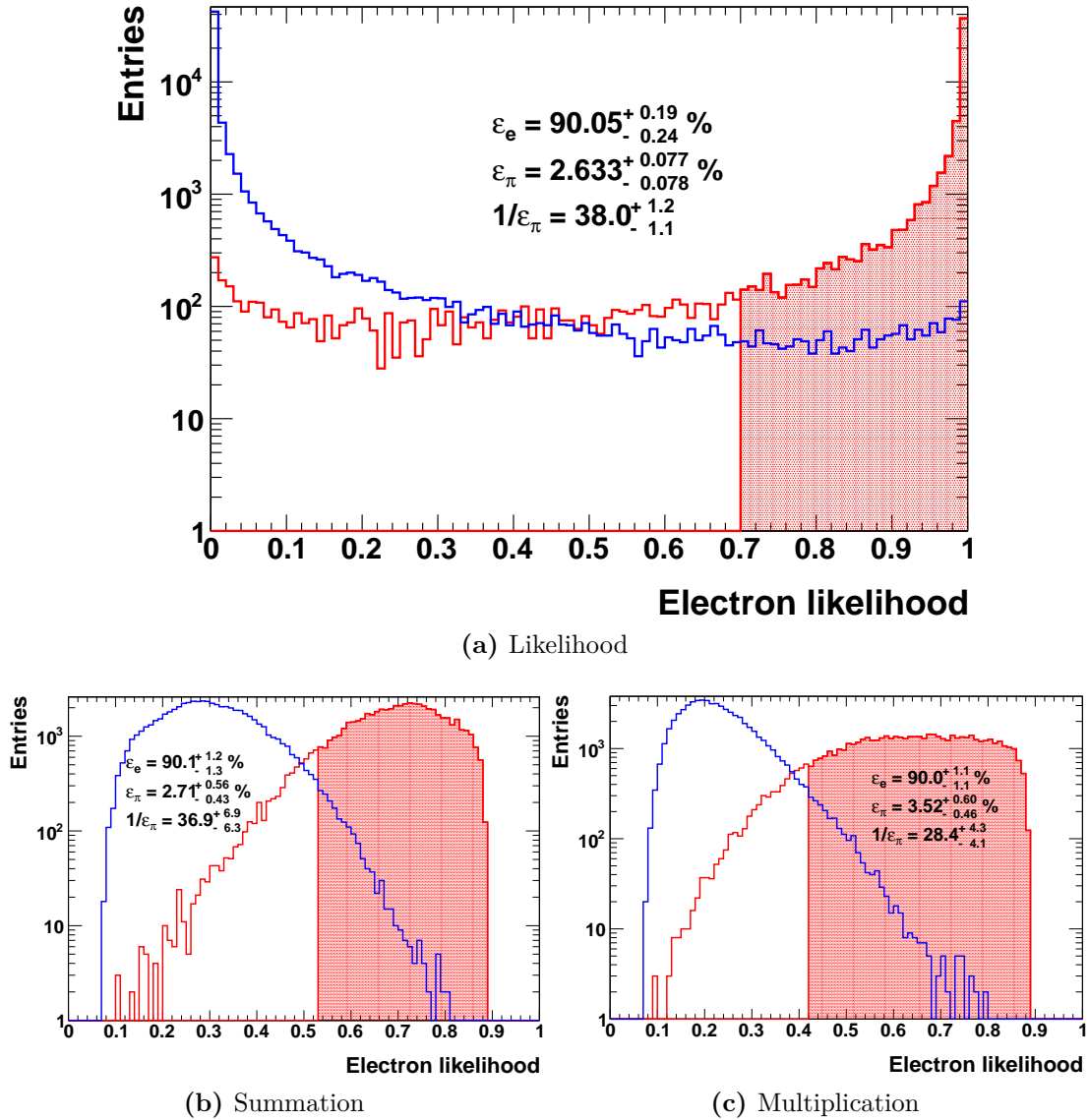
(c) Multiplication

Figure 5.1.: PID performance example plots for different combination methods: **a)** likelihood, **b)** summation, **c)** multiplication. The electron likelihood of a track is plotted on the abscissa and the ordinate indicates the number of tracks with such a likelihood. The pions are plotted in blue, the electrons in red. The hatched area marks the region in which 90% of all electrons lie. The left boundary of this region (e.g. at 0.7 in **a)**) is the threshold t_e of the electron efficiency above which a track is considered to belong to an electron.

For these plots, the data set for momentum 3 GeV/c at the tracklets stage has been used with the following settings: only electrons and pions are taken into account, TC is off, nominal drift velocity and gas gain, SW 2-26.

5.2. Preliminary Considerations

Once LUT and threshold have been fixed for specific conditions, a change of these conditions will directly influence the PID performance. As the typical total charge distributions (cf. Fig. 4.3, p. 63) show, non-electrons are most probably located at lower charges, whereas electrons in most cases have a higher charge deposition. By design, non-electrons are located in the minimum and electrons at the peak of a LUT (see Fig. 4.4, p. 63, for a typical LUT). However, the charge deposition depends on parameters like drift velocity and gas gain. If these parameters change, the charge deposition and, thus, the PID performance will do so, as well.

For instance, if the charge deposition is enhanced (for all particle species), the tracklet charges are shifted to the right in the LUT (that is kept fixed). Pion tracklets experience the steep rise of the LUT. Hence, the tracklets of a pion track are much more likely to be misidentified as electron tracklets. This yields a smaller pion rejection because pion tracks are able to exceed the threshold t_e and are wrongly identified as electrons. The electron peak of the LUT is asymmetric: It is very steep at small charge depositions, but levels off smoothly to higher charges. With some probability, electron tracklets are located on the left and on the right side of the peak. As the pion tracklets, the electron tracklets on the left side are pushed to the peak, resulting in electron tracks that are more likely to exceed the threshold. For the tracklets on the right side of the peak, the electron likelihood is decreased. However, due to the rather flat shape of the LUT in this region, the latter effect is relatively small, but partially compensates the impact of the electron tracklets on the left side of the peak.

Altogether, keeping LUT and threshold fixed, a higher charge deposition implies a higher electron efficiency and a smaller pion suppression, whereby the latter aspect is expected to be more pronounced.

5.3. Relevance of the Limited Precision of Decimal Places

In principle, the LUTs can be loaded directly into the MCM simulation and be used to calculate the electron likelihood of the tracklets. The GTU simulation combines these likelihoods to the track electron likelihood with the actual precision of decimal places. Yet, the GTU simulation is very time-consuming and only one combination method for the tracklet likelihoods is implemented in the GTU simulation at the moment. Furthermore, the rounding strategies are still under development.

Therefore, it was decided to use a different approach to determine the track PID: For each track (either build from MC data (tracklets stage) or by the GTU simulation (GTU tracks stage)), the charge of the tracklets is used to obtain the

electron likelihood from a LUT histogram. The LUT histogram exhibits a slightly higher granularity than a LUT that can be stored in the MCMs. This is due to the limited amount of memory of the MCMs. Afterwards, the tracklet likelihoods are combined to the electron likelihood of the track with the full precision of decimal places available offline.

To justify this method, parts of the PID performance have been carried out in parallel with the LUT of the MCMs and the real number of decimal places for the tracklet likelihood combination. It was found that the effect of the mentioned aspects is negligible. The only difference, that might occur, is that the threshold t_e can be shifted. Such a shift is already taken into account by the error estimation. As a consequence, the results of both methods are consistent within the errors. This legitimates the use of the alternative method, but it must be kept in mind that the threshold t_e slightly depends on the precision of decimal places.

5.4. Importance of Electron Efficiency and Combination Method

The effect of various choices of the electron efficiency on the pion suppression is shown in Fig. 5.2 for different combination methods. The data points correspond to 3 GeV/c particles and SW 2-26. The same basic trends are found for SW 2-21 and for 5 GeV/c[4].

As the plot shows, giving up some electrons leads to a significant improvement of the pion suppression. For example, lowering the electron efficiency from 90% to 80% enhances the pion suppression by a factor 2-3. This is expected because lowering the electron efficiency is equivalent to shifting the threshold t_e to higher electron likelihoods (cf. Fig. 5.1). It is also visible in this plot that the summation and the likelihood combination method yield very similar results, whereas the multiplication method is always worse (typically by 20-30% for TC off and by 40-50% for TC on).

At first sight, it is peculiar that the solid blue line stops around electron efficiency 0.6. Though, this can be explained by the shape of the likelihood distribution, as shown in Fig. 5.1a: The bin with the electron peak on the very right side contains already about 60% of all electrons. Hence, it is neither possible to determine the pion suppression for smaller electron likelihoods, nor to calculate its upper error by shifting the threshold one bin to the right.

The following conclusions can be drawn[5]:

- The pion suppression is best for the likelihood combination method, a little bit worse for the summation and worst for the multiplication method.

---

[4]For details, refer to Fig. D.1 (3 GeV/c, SW 2-21) on p. 114 and to Figs. D.3 (p. 128) and D.4 (p. 129) for 5 GeV/c.
[5]Details can be found in Tabs. D.1-D.3 (p. 116 ff.).

- The errors of electron efficiency and pion suppression at 90% electron efficiency are smallest for the likelihood combination method, larger for the multiplication and largest for the summation method.
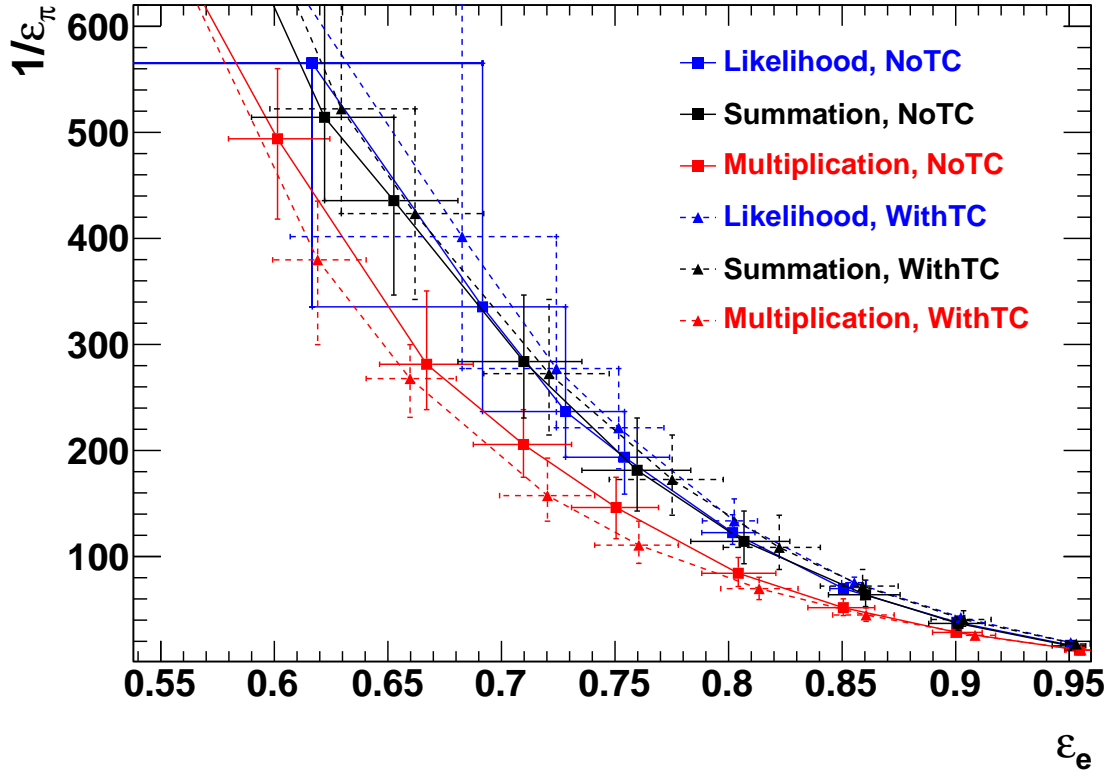
Figure 5.2.: Pion suppression as a function of electron efficiency for the tracklets stage, 3 GeV/c, only pions, SW 2-26 and normal gas gain and drift velocity. The curves are just trend lines (no fits!) through the data points and are coloured differently for the different combination methods: likelihood (blue), summation (black), multiplication (red). Data for TC off is illustrated by solid lines and squares, data for TC on by broken lines and triangles. Note that the upper error of the very left point of the solid blue curve cannot be estimated with the used error estimation method. The reason is that the threshold is already at the very right side of the spectrum and cannot be moved further to the right.

The latter aspect is plausible because the shape of the likelihood distributions is rather flat for the likelihood method around the threshold t_e and steeper for the other combination methods (see Fig. 5.1, p. 83). As a result, the likelihood method would be the best choice. Unfortunately, it presumably cannot be used in hardware due to time constraints. The next best choice is the summation method, although the errors are large, i.e. this method is very sensitive to the determination of the threshold t_e.

Since the results are very similar for the summation and the likelihood method, but the errors are much smaller for the latter, the following discussion will be based on the results for the likelihood method.

The results of the analysis are summed up in Tabs. 5.1-5.4 for the tracklets stage and in Tabs. D.25-D.28 (p. 144 f.) for the GTU tracks stage. In these tables, the relative change of the pion suppression and/or the electron efficiency under certain conditions is stated. The errors of the electron efficiency and the pion suppression are asymmetric. For an estimation of the error of the relative changes, the maximum of the upper and lower errors has been used for a Gaussian error propagation. So, the resulting errors can be considered as the order of magnitude of the uncertainty.

The results will be discussed in the following sections.

5.5. PID Performance for Different Gas Gains

The important trends of electron efficiency and pion suppression for changes of the gas gain are summarised in Tab. 5.1. The gas gain

- has some effect on the electron efficiency, but the relative changes are roughly within 11%.

- tremendously influences the pion suppression.

- leads to similar relative changes of pion suppression and electron efficiency for both summation windows.

Relative change of gas gain [%]	Relative change of electron efficiency [%]		Relative change of pion suppression [%]	
	SW 2-21	SW 2-26	SW 2-21	SW 2-26
-10%	-11.04 ± 0.39	-10.0 ± 0.48	$+191 \pm 14$	$+227 \pm 17$
$+5\%$	$+3.24 \pm 0.29$	$+3.36 \pm 0.35$	-34.8 ± 2.6	-36.9 ± 3.0
$+10\%$	$+5.79 \pm 0.28$	$+5.47 \pm 0.35$	-57.2 ± 1.6	-60.1 ± 1.9

Table 5.1.: Relative changes of electron efficiency and pion suppression with gas gain for 3.0 GeV/c particles, tracklets stage, only pions, no tail cancellation, likelihood method. Gas gain 4000 is the reference gas gain. Taking into account the errors, the results of all three combination methods (other methods not shown) are consistent.

This can easily be understood by glancing back on Fig. 4.5 (p. 68): A higher gas gain increases the deposited charge of all particle species. As discussed before, this improves the electron efficiency, but diminishes the pion suppression, with

the latter effect being more pronounced. Since the ADC-signal of every time bin can be scaled with the gas gain (cf. section 4.4) by the same factor, the relative changes are indeed expected to be similar for both summation windows (third observation).

Another point is crucial: As Tab. 5.1 suggests, a relative gas gain change of 10% is already far too much for a reasonable PID. Hence, there is no need for simulations with $> 10\%$ gas gain changes because the PID performance will evidently be worse. This justifies the chosen gas gain range for the simulations.
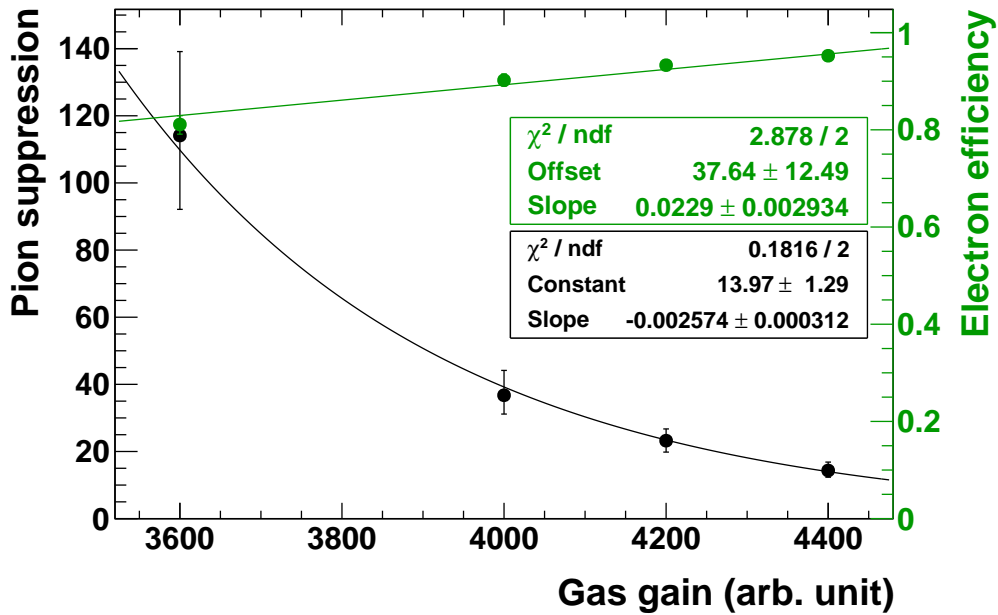
Figure 5.3.: Impact of the gas gain on the PID. The data points are for the tracklets stage, 3 GeV/c, only pions, no TC, SW 2-26. The used combination method is "summation" as currently used by the GTU. The figure shows the dependence of the electron efficiency (green, right axis) and the pion suppression (black, left axis) on the gas gain. The shown curves are fit results. Obviously, in the considered gas gain region, the electron efficiency exhibits a linear behaviour, whereas the pion suppression is described reasonably well by an exponential function. The equivalent results can be obtained for the GTU tracks stage. The fit parameters of both stages are in agreement within the errors (see Fig. D.6 (p. 143) for detailed results for the GTU tracks stage).

Fig. 5.3 shows the dependence of the electron efficiency (green) and the pion suppression (black) on the gas gain for SW 2-26. The electron efficiency has been fitted with a linear function and the pion suppression by an exponential one. The χ^2 per degree of freedom of both fits looks very reasonable. Therefore, the fits allow to estimate the PID performance in the $\pm 10\%$ gas gain region and to extrapolate to larger gas gain changes.

From the obtained fit parameters it can be calculated which relative change of the gas gain $\Delta G/G$ (with $G = 4000$) is at most possible if a relative decrease of the pion suppression y is tolerable:

$$(1 - y) \overset{!}{=} \frac{\exp(-0.002574 \cdot (1 + \Delta G/G) \cdot 4000 + 13.97)}{\exp(-0.002574 \cdot 4000 + 13.97)}$$
$$\Rightarrow \Delta G/G = \frac{\ln(1 - y)}{4000 \cdot (-0.002574)} \tag{5.3}$$

For example, if $y = 10\%$ is assumed, Eq. 5.3 yields $\Delta G/G \approx +1\%$. Consequently, a maximal decrease of the pion suppression by 10% requires the gas gain not to increase more than 1%, which is a rather tight bound.

5.6. Influence of Drift Velocity and Choice of Summation Window

Tab. 5.2 contains the most important results for a change of the drift velocity compared to 1.5 cm/μs for two summation windows.

TC	Change of drift velocity [cm/μs]	Relative change of electron efficiency [%]	
		SW 2-21	SW 2-26
Off	-0.1	-6.96 ± 0.43	$+0.21 \pm 0.39$
	$+0.1$	$+3.87 \pm 0.38$	-0.12 ± 0.38
On	-0.1	-7.31 ± 0.39	$+2.03 \pm 0.37$
	$+0.1$	$+3.23 \pm 0.29$	-3.16 ± 0.38
TC	Change of drift velocity [cm/μs]	Relative change of pion suppression [%]	
		SW 2-21	SW 2-26
Off	-0.1	$+57.2 \pm 6.2$	$+10.0 \pm 5.3$
	$+0.1$	-28.0 ± 2.4	-7.4 ± 4.3
On	-0.1	$+48.8 \pm 6.1$	-21.4 ± 4.3
	$+0.1$	-23.2 ± 3.0	$+19.3 \pm 5.7$

Table 5.2.: Relative changes of electron efficiency and pion suppression with drift velocity for 3.0 GeV/c particles, tracklets stage, only pions, likelihood method. The reference drift velocity is 1.5 cm/μs. Respecting the errors, the results of all three combination methods (other methods not shown) are consistent.

The impact on the PID performance can be summarised as follows:

5. Online PID Performance Results

- With smaller drift velocity, the electron efficiency decreases and the pion suppression increases. The only exception is the case with TC on, SW 2-26, where these trends are exactly inverted (this exception will be explained within the discussion of the effect of the tail cancellation in section 5.7).

- The effects of the last point are much more pronounced for the SW 2-21 case. In particular, the relative change of the electron efficiency is consistent with zero for SW 2-26, TC off.

- Having more time bins (2-26) available for the summation, the pion suppression is improved by approximately a factor of 2. At the same time, for nominal drift velocity and a fixed gas gain, the electron efficiency is almost left untouched by changes of the summation window (for details, cf. Tab. D.3 p. 118).
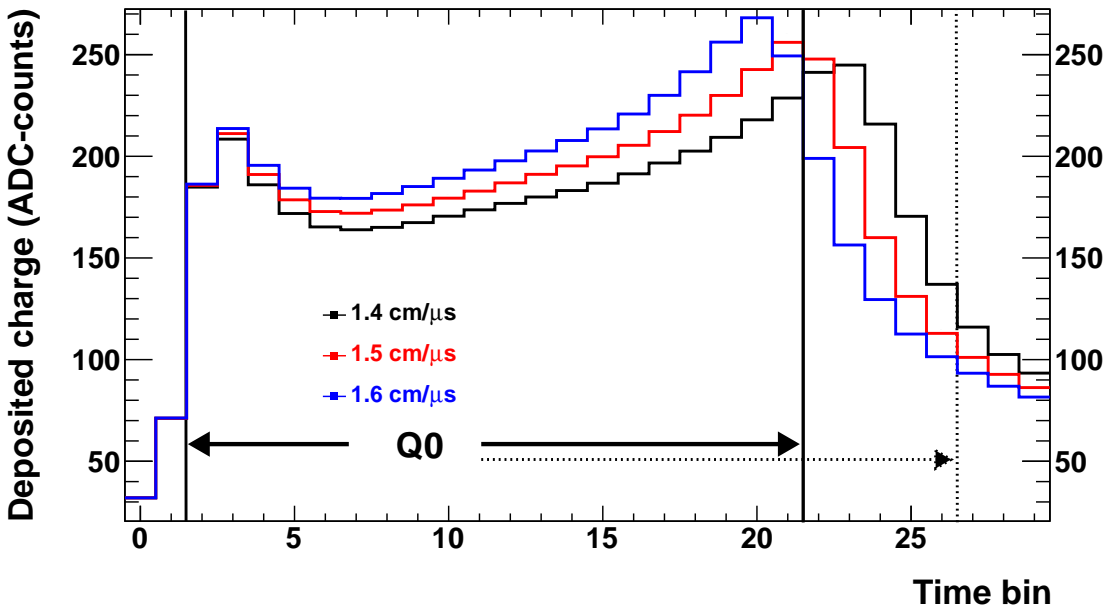
Figure 5.4.: Average pulse height of electrons for different drift velocities. The black line corresponds to 1.4 cm/μs, red to 1.5 cm/μs and blue to 1.6 cm/μs. The vertical black lines indicate the border of the two considered summation windows for Q_0: SW 2-21 (solid on the right side) and SW 2-26 (dotted on the right side). The higher the drift velocity, the more the signal shape gets compressed in time.

The general trend mentioned in the first point is explained in Fig. 5.4, where the average pulse height of electrons for different drift velocities and the summation window Q_0 (vertical, black lines) are shown. The higher the drift velocity, the more the shape of the signal gets compressed in time. This implies that for a fixed summation window, more charge is pulled into (pushed out of) this window for higher (lower) drift velocities. It was checked that the Q_0 spectrum is indeed

slightly shifted to higher (lower) deposited charges for increased (decreased) drift velocity. In particular, if the summation window ends at time bin 21, the whole TR peak can be shifted in or out with changing drift velocity, which strongly affects Q_0. As discussed before, more charge for both, pions and electrons, leads to a higher electron efficiency and a smaller pion suppression.

However, for SW 2-26, the edge of the average pulse height and the TR peak lie safely inside the summation window. Therefore, the mentioned effect is rather small, what explains the second observation in the above list.

Finally, the more time bins are available for Q_0, the more a different dE/dx of pions and electrons is reflected in this summed charged. In addition, the TR peak is with quite some probability in time bins later than 21. Altogether, this explains why more time bins allow for a better e/π-separation (last observation in the list).

The bottom line of all this is that the PID performance suggests to sample over the whole drift time in order not to cut into the signal.

5.7. Effects of the Tail Cancellation

In Tab. 5.3, an overview of the impact of the tail cancellation on the PID performance depending on gas gain and drift velocity is given. Further impacts can be deduced from Tab. 5.2. The influence of the tail cancellation on the PID performance can be described as follows:

- The tail cancellation reverses the trends of pion rejection and electron efficiency with changes of the drift velocity for SW 2-26.

- In case of SW 2-26, the TC enhances the sensitivity to changes of the drift velocity.

- The electron efficiency is almost the same for TC on and off[6]. The relative change is approximately 1% or often less, with one exception: For SW 2-26, the deviation might be a few percent for fluctuating drift velocities.

- For SW 2-26, the pion suppression is improved, if TC is enabled.

- On the contrary, the TC diminishes the pion suppression slightly for SW 2-21.

The explanation of these observations is pretty involved. First, it needs to be understood how the TC acts on the input signals: Fig. 5.4 shows that higher drift velocities correspond to sharper/shorter signal shapes, changing the amount of charge inside the summation window with varying drift velocity. This effect will be called "charge shifting" in the following. In case of SW 2-26, the "charge

---

[6]For details, refer to Tab. D.3 (p. 118).

Gas gain	Relative change of pion suppression [%]	
[arb. unit]	SW 2-21	SW 2-26
3600	-16.9 ± 4.0	$+5.4 \pm 5.5$
4000	-8.5 ± 3.7	$+18.1 \pm 6.5$
4200	-7.5 ± 3.1	$+10.9 \pm 4.4$
4400	-4.4 ± 2.9	$+14.7 \pm 4.4$
Drift velocity	Relative change of pion suppression [%]	
[cm/μs]	SW 2-21	SW 2-26
1.4	-9.1 ± 3.9	-20.1 ± 4.2
1.5	-4.0 ± 3.6	$+11.8 \pm 5.5$
1.6	$+2.5 \pm 3.6$	$+44.0 \pm 6.5$

Table 5.3.: Relative changes of pion suppression for TC on compared to TC off for 3.0 GeV/c particles, tracklets stage, only pions, likelihood method. Taking into account the errors, the results of all three combination methods (other methods not shown) are consistent. Note that the electron efficiency is, in general, different for TC on and TC off.

shifting" is rather small and for enabled TC, another effect dominates: The tail cancellation suppresses sharper signals with respect to broader ones. This is shown in Fig. 5.5: A sharp signal (red broken line) and a broad one (blue broken line) with equal integral over all time bins are fed into the TC filter. The solid lines indicate the filtered signals. Obviously, the integral of the filtered, sharp signal is smaller than that of the filtered, broad signal.

This implies that sharper signals of higher drift velocities are more suppressed than those of lower drift velocities. As mentioned above, the "charge shifting" gives a smaller effect for SW 2-26 than this suppression, which explains the inverted trends of electron efficiency and pion suppression in the first observation.

Furthermore, the suppression of sharper signals leads to larger changes of the summed charge with varying drift velocity than they occur due to the "charge shifting" for SW 2-26. This clarifies the second observation and the exception in the third observation. Another aspect contributing to these observations will be discussed below.

For SW 2-21, the impact of the suppression of sharper signals is rather small and, after adjusting the electron efficiency to 90% for nominal conditions, there is no reason why the electron efficiency should behave differently under gas gain or drift velocity changes compared to the case without TC. So, the whole third observation seems to be reasonable, if the previous explanation for the exception is respected.
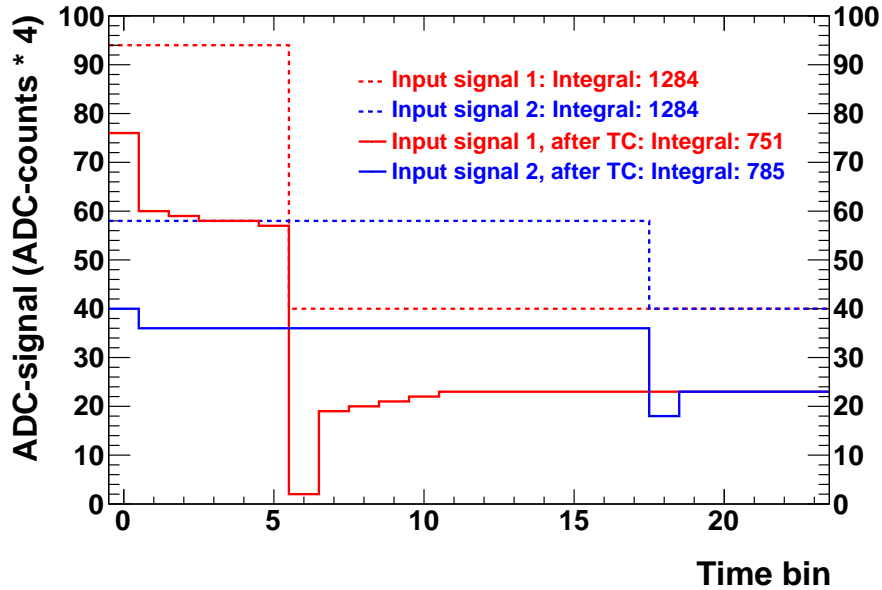
Figure 5.5.: Effect of the tail cancellation on different signal shapes. The broken lines show the pulse heights of the input signals for one ADC-channel, multiplied by a factor 4 (this corresponds to the MCM-internal representation of the amplitude): Red is a short/sharp signal, blue a longer/broader one. The amplitude of 40 at the end is the baseline. The amplitudes and durations of the signals have been chosen such that the integrals of these signals over all time bins are equal. The solid lines illustrate the corresponding signals after application of the tail cancellation filter. As can be read off from their integrals over all time bins, sharper signals get more suppressed by the tail cancellation than broader ones.

However, how can the other observations be explained? The TC is designed to cut away the ion tails, i.e. mainly the later time bins of the pulse height are affected by it. It happens that the TC decreases the charge in a time bin so much that it falls below a threshold and is rejected, i.e. the charge of the corresponding cluster is not attributed to the tracklet. This is always a loss, since the charge is at least the baseline, which is not subtracted online.

Considering the average pulse height of pions (same behaviour as in Fig. 5.4, but no TR peak), two things happen, when the drift velocity gets smaller: First, the signal shape gets broader and, thus, less suppressed by the TC. Second, the charge distribution is stretched to later time bins. Both aspects lead to a higher probability that the cluster charge is above the threshold in later time bins. As a consequence, pion tracklets have a higher total charge that is more similar to that of electron tracklets. Hence, the pion rejection gets worse. On the other hand, if the drift velocity is increased, an analogue argumentation shows that this results in a lower probability that a cluster in later time bins is accepted. However, in the time bin range 2-21 or in the no TC case, the signal is usually above the threshold for all considered drift velocities. As a result, this cluster rejection explains why

TC enlarges the sensitivity to drift velocity only for SW 2-26.

On the other hand, the cluster rejection also explains the improved pion rejection for the SW 2-26 case: Most likely, clusters of pions are rejected in later time bins, whereas for electrons, the TR peak keeps the signal above the threshold. Hence, the total charge is decreased for pions by the TC, but stays almost the same for electrons. As a consequence, a better e/π-separation is possible in case of TC on (second to last observation).

So, only one question remains: Why does TC decrease the pion suppression for SW 2-21 slightly (last observation)? As it was checked, it is rather unlikely that pion clusters are rejected due to TC before time bin 21 for nominal drift velocity. As an implication, no benefit can be drawn from the cluster rejection. However, the TR peak in the electron spectrum has a relatively sharp shape, meaning that it is suppressed by the TC. With a certain probability, the TR peak is located in the time bin range 2-21, so that the TC causes a suppression of the total deposited charge of electrons compared to that of pions. Both charges become more similar, which causes a worse pion suppression. This effect is, of course, also present for SW 2-26, but there the benefit from the cluster rejection dominates, since the TR peak is more likely at time bins later than 21 and these electron clusters then survive in contrast to those of pions.

The validity of this train of thought can be checked with, for instance, the data for 3.0 GeV/c, tracklets stage, only pions, likelihood method and SW 2-21 (details can be found in Tab. D.3, p. 118): For a drift velocity of 1.5 cm/μs, the TC worsens the pion suppression a bit. There is only the suppression of the TR peak present, reducing the pion suppression from 17.95 (TC off) to 17.23 (TC on). When changing the drift velocity to 1.6 cm/μs, this suppression is still present, but due to the compressed shape compared to before, pion clusters are rejected to some extend. In total, this improves the pion rejection slightly. Indeed, it is found that the pion rejection increases from 12.92 (TC off) to 13.24 (TC on).

5.8. Impact of Cuts for the Look-Up Table

It was checked if the PID performance can be improved by applying a different set of cuts for the creation of the LUTs (cf. section 4.5). In this case, LUTs with the same cuts as applied for the PID performance have been generated. In particular, the cut on pad row crossing has been abandoned. The idea is that the PID performance might be better, if the LUT is created with data that already exhibits inadequateness, such as pad row crossing. However, these LUTs do not improve the PID performance, but, on the contrary, worsen the pion suppression. Note that the utilised data sets are limited to the central stacks of the TRD, where pad row crossing is less important than in outer stacks. Yet, other data sets with particles passing the outer stacks have also been generated. For these data sets, the same conclusion was found. So, this statement is valid for all stacks.

5.9. Influence of other Particle Species

For the results considered so far, only electrons and pions have been taken into account (abbreviated by the phrase *only pions*). In Tab. 5.4, these results are compared to the *all* case, where also muons, kaons and protons are respected. Again, the complete set of results has been added to appendix D.

Settings		Pion suppression		Relative change of
TC	SW	only pions	all	pion suppression *only pions → all* [%]
Off	2-21	$17.95^{+0.42}_{-0.38}$	$22.59^{+0.55}_{-0.62}$	$+25.8 \pm 4.5$
On		$17.23^{+0.51}_{-0.40}$	$20.65^{+0.47}_{-0.47}$	$+19.8 \pm 4.5$
Off	2-26	$38.0^{+1.2}_{-1.1}$	$46.7^{+1.9}_{-1.6}$	$+22.9 \pm 6.3$
On		$42.5^{+1.2}_{-1.6}$	$51.8^{+2.7}_{-2.2}$	$+21.9 \pm 7.8$

Table 5.4.: Impact of other particle species on the PID performance demonstrated for 3.0 GeV/c particles, drift velocity 1.5 cm/μs, nominal gas gain, tracklets stage, likelihood method. *Only pions* means that only electrons and pions are taken into account, whereas in case of *all*, also muons, protons and kaons (with 1:1:1:1 relative abundance) are considered. By design, the electron efficiencies are consistent with 90% for all cases and not shown for this reason. In the right column, the relative change of the pion suppression from *only pions* to *all* is stated.
Note that "pion suppression" is used as a synonym for "non-electron suppression" in case of *all*, since it is the commonly used phrase.

As Fig. 4.4 (p. 63) suggests, other particle species have only a very small influence on the LUT. This is confirmed, when e.g. the electron efficiencies for *only pions* and *all* are compared[7]: The data for the electrons is the same and the LUTs are similar, which implies similar electron efficiencies. Indeed, the electron efficiencies are found to be almost the same for all parameter settings.

In case of *all*, every species other than electrons is treated as non-electrons. From Tab. 5.4 it can be seen that the pion suppression, or rather "non-electron suppression", increases by about 20%, if other particle species are also taken into account. This can be understood with the help of Fig. 1.7 (p. 14), which allows for a rough estimation of the particles' dE/dx in the momentum region above 2 GeV/c. Obviously, kaons and protons have a smaller dE/dx than pions, while that of muons (not shown in the figure) is similar to the one of electrons and, thus, larger. In section 4.1.1, it was mentioned that no a-priori probabilities concerning the relative particle abundance are taken into account. Consequently, in the *all* case, a pion is replaced by a "non-electron" that is some kind of average of pion,

---

[7]For details, compare Tabs. D.3 (p. 118) and D.6 (p. 121).

muon, proton and kaon with equal weights (1:1:1:1). This average "non-electron" has a smaller dE/dx than a pion, so that a better e/π-separation is expected. This agrees with the obtained results.

In ALICE, pions are by far the most abundant particles [58]. Therefore, the *only pions* case is more realistic and, as the impact of other species shows, gives a conservative estimation of the pion suppression.

5.10. Results for 5 GeV/c

The whole analysis of the PID performance was repeated for data sets with 5.0 GeV/c particles. This is important to get extrapolations of the 3 GeV/c results to higher momenta and to check, whether the e/π-separation is reasonable for such high momenta. The latter aspect is interesting with respect to di-electron decays of the Υ.

The results have been obtained by using the LUTs and thresholds for the 3.0 GeV/c case. The reason is that only one LUT and only one threshold can be defined at the same time in hardware. As explained in section 4.3, a momentum of 3.0 GeV/c has been chosen as a reference. Furthermore, due to the exponential fall-off of the p_t-spectrum, there are many more 3 GeV/c than 5 GeV/c particles. So, this strategy allows to explore the PID performance for particles with higher momenta. The full collection of the results is presented in appendix D.

For the same reasons as for the 3.0 GeV/c case, the results for the likelihood combination method are considered to obtain conclusions. Compared to the 3 GeV/c case, the results are[8]:

- The electron efficiency is higher (relative change at most +5%).

- The pion rejection is lower by roughly a factor of 2 in all cases, i.e. for different summation windows, drift velocities and gas gains, TC on/off.

Both observations can be explained by the higher charge deposition of all particle species. According to Fig. 1.7 (p. 14), a slight increase in dE/dx for electrons and a much larger one for pions can be expected, if the momentum increases from 3 to 5 GeV/c. In case of electrons, there is also a small rise of the probability for transition radiation, but the TR yield already saturates in this momentum region. Altogether, the pion charge deposit increases more than that of electrons, so that these charge deposits become more similar. After all, this yields a worse e/π-separation. It was verified that the pion suppression is also worse than at 3 GeV/c, if a special 5 GeV/c LUT with its own threshold is used. This strongly supports the above argumentation.

---

[8]For details, compare for example D.3 (p. 118) and D.15 (p. 133).

It was checked that the charge Q_0 indeed increases for both, electrons and pions. Anyway, the change of the Q_0 distributions and, thus, of the LUT is very small.

The almost constant factor 2 in the pion rejection for all considered cases implies that the qualitative trends of the PID performance with respect to the considered parameters are the same for both particle momenta.

Although the pion rejection is worse, the absolute value is sufficiently high for a trigger on 5 GeV/c electrons, especially, if some electron fraction is given up by decreasing the electron efficiency. For instance, choosing an electron efficiency of 80%, using the summation method, taking into account only electrons and pions and turning off the TC, the pion suppression is around 90 for SW 2-26 and around 35 for SW 2-21, respectively. Hence, triggering on electrons from Υ decays with good pion suppression is feasible.

5.11. Results for the GTU Tracks Stage

All results presented up to this point have been obtained for the tracklets stage. It is a very beneficial cross-check to compare with the GTU tracks stage. The detailed results for the GTU tracks stage are collected in appendix D, in particular in section D.3. In this section, the most important findings are briefly discussed.

Comparing the results for the tracklets stage with those of the GTU tracks stage, the following points are noticeable:

- As a very rough estimation for 3 GeV/c, only pions, the GTU stage exhibits an improved pion suppression by approximately 50% for SW 2-21 compared to the tracklets stage and by 10-20% for SW 2-26.

- The impact of all investigated parameters on the PID performance, as shown in the last sections, are very similar for both stages and coincide within the errors[9], i.e. the relative changes of PID performance quantities are consistent for the two stages.

- The electron efficiencies of both stages are very similar. For nominal conditions, this is clear by definition (the electron efficiency is demanded to be 90%) and for other conditions, this happens due to the approximately equal relative changes mentioned in the previous point.

- All preceding statements have been confirmed for the 5 GeV/c data set.

The last 3 points are very pleasant because they confirm the validity of the obtained observations for different analysis methods. Evidently, the error caused

---

[9]This observation can be made by comparing Tabs. 5.1-5.4 (p. 87 ff.) for the tracklets stage with Tabs. D.25-D.28 (p. 144 f.) for the GTU tracks stage.

by the uncertainty of the choice of the threshold bin t_e is sufficient to cover the slight differences of the results of the two analysis stages. Nevertheless, the first point of the list needs to be understood. Why does the GTU tracks stage yield a better PID performance than the tracklets stage?

Tracklet selection strategy	Electron efficiency [%]	Pion suppression
Simple GTU imitation	$90.21^{+0.25}_{-0.28}$	$36.4^{+1.4}_{-0.9}$
GTU simulation	$90.11^{+0.29}_{-0.32}$	$43.9^{+1.8}_{-1.4}$
Most charge (ideal)	$91.2^{+0.9}_{-1.2}$	79^{+19}_{-10}

Table 5.5.: Comparison of various methods to handle doubly found tracklets. *Simple GTU imitation* is the method used for the tracklets stage, where the selection is based on simple geometrical arguments. *GTU simulation* indicates the case, in which the complex and close-to-hardware GTU simulation is used for the selection, whereas *most charge (ideal)* describes a more or less ideal selection, for which the tracklet with the most charge is used in case of ambiguous tracklets. All methods use the same LUT, but the threshold has been adjusted for every case separately. The values have been obtained with the settings for the case: 3 GeV/c, only pions, SW 2-26, no TC, nominal gas gain and drift velocity and the likelihood combination method.

By design of the cuts and the chosen methods, the only differences between the tracklets and GTU tracks stage should be the treatment of doubly found tracklets (see section 4.7) and the number of tracklets per track[10]. It was checked that the number of tracklets per track is almost the same at both analysis stages and cannot explain the different pion suppression. However, the treatment of doubly found tracklets has a strong influence on the PID performance and causes the observed deviation, as presented in Tab. 5.5.

The table shows the comparison of three different methods for doubly found tracklets handling. The *ideal* method, where the tracklet with the most charge is selected, gives by far the best pion suppression. The method in the real *GTU simulation* (used at the GTU tracks stage) is worse, but still better than the *simple GTU imitation*, that has been used for the tracklets stage. The only difference between the *ideal* method and the *simple GTU imitation* is the handling of doubly found tracklets. This has been ensured by using the same set of cuts at the tracklets stage. Apparently, the handling of doubly found tracklets strongly influences the PID performance. So, when respecting the conclusions drawn in section 4.7, the train of thought ends up in the insight that this handling is the reason for the improved pion suppression at the GTU tracks stage.

It must be stressed that the effect of doubly found tracklets on the PID performance has been tested and identified with the help of the tracklets stage, where

---

[10]Fewer tracklets per track lead to a decrease of the pion suppression, see Fig. 5.6 (p. 101).

it is perfectly known and controllable which tracklets are used for the analysis. Again, this points out the power of such an intermediate analysis stage.

Next, it needs to be clarified why the handling of doubly found tracklets affects the PID performance. It can be deduced from Fig. 4.3 (p. 63) that non-electron tracklets are relatively sharply located at lower deposited charges, whereas electron tracklets have a rather broad distribution around a higher most probable charge. Doubly found tracklets cause a "loss" of charge, if the "wrong" tracklet is selected (cf. section 4.7). This shifts tracklets to lower charge values in the LUT. However, non-electron tracklets are most likely in the minimum of the LUT and are even shifted to higher electron likelihoods, if charge gets "lost" by this mechanism (see Fig. 4.4, p. 63). On the contrary, the most probable charge for electron tracklets is the peak of the LUT. If such tracklets "loose" charge, they experience the steep fall of the LUT and run the risk of being wrongly identified as non-electron tracklets. All in all, this shifts the threshold t_e to lower electron likelihoods and, thus, deteriorates the pion suppression. The size of this effect can be understood by the following consideration: Typically, there are about 5.7 tracklets per track and roughly 30% doubly found tracklets. As a consequence, every track contains on average one or two tracklets that are affected by this ambiguity. Thus, a large effect is expected and, indeed, observed.

The case with SW 2-21 is much stronger influenced by the treatment of doubly found tracklets than the case with SW 2-26 for the following reason: As explained in section 4.7, clusters and charge get "lost" due to doubly found tracklets mainly in early time bins, i.e. mainly up to time bin 11. The fraction of the "lost" charge compared to the total one is much larger, if only the time bins 2-21 are used for summation, since the total charge is smaller and only parts of the TR peak are inside the summation window.

In summary, the GTU tracks stage shows a better pion suppression than the tracklets stage due to a better handling of doubly found tracklets. Fortunately, the relative changes of PID performance quantities for varying parameters are consistent for both stages within the errors, which implies a successful cross-check. Since the handling of doubly found tracklets is the main difference between both stages, the cuts at the tracklets stage seem to be very similar to the matching of the GTU. This is expected and strengthens the confidence that both, cuts and GTU matching, behave in the desired manner.

5.12. Caveats in more Realistic Situations

This section discusses what deteriorates the PID performance in more realistic situations compared to the rather idealistic simulation:

- In the experiment, the pseudo-rapidity η is solely restricted by the acceptance of the TRD, which is $\eta \in [-0.9, +0.9]$. This introduces issues with the tracklet length, which are tried to be overcome by correction factors: If a

particle flies from the vertex through a stack on the outside of the detector, the tracklet length and, thus, the deposited charge will be larger than if it would pass the central stack. For each pad of a chamber, a correction factor for the deposited charge can be calculated using the pad's angle with respect to the ALICE global x-y plane.

However, there are many more tracklets with pad row crossing in the outer stacks. This influence has been investigated in simulations. According to first results, pad row crossing has a dramatic effect on the PID performance: Only the charge of one pad row is attributed to a tracklet, that of the other row is lost. This reduces the total charge of tracklets for both, electrons and pions. The result is electron tracklets with the typical (low) total charge of pions and, hence, a rather small electron likelihood. So, to get a 90% electron efficiency, the threshold t_e needs to be small. This results in a tremendous decrease of the pion suppression by about a factor 3 or larger. The investigation of this issue and possible solutions is still ongoing [63].

- In the simulation, secondaries have been excluded. Especially, such particles have different momenta than primaries. This would spoil the analysis of the PID performance, that is intended to be carried for a fixed momentum. In the experiment, secondaries increase the total number of tracks. The PID performance can then suffer from the same problems discussed in the last point of this list.

  Another aspect with respect to secondaries is the tracklet length correction factor discussed in the previous point: A secondary particle might be created some distance apart from the vertex and fly perpendicularly through the layers of a stack on the outside of the detector. Then, the tracklet length correction would be applied. But, in contrast to a particle coming from the vertex, the tracklet length should not be corrected for this particle. Therefore, the tracklet length correction can be wrong for secondaries, which will downgrade the PID performance.

- In the experiment, there is not only one sharp momentum as in the simulation. Rather, the momenta will follow approximately an exponential distribution, on which cuts can be applied to select a certain range, e.g. p $\geq$ 2.5 GeV/c. Different momenta lead to different deposited charge distributions (this can be understood from Fig. 1.7, p. 14), but there is only one LUT stored in the MCMs, which cannot be tuned on all momenta simultaneously. Thus, the PID performance will deteriorate.

- In the simulations, detector inefficiencies have not been taken into account, i.e. an ideal detector geometry has been used. Yet, missing or malfunctioning chambers result in fewer tracklets per track. As can be read off from Fig. 5.6, this worsens the PID performance.

- In Pb–Pb collisions, the particle multiplicities are considerably higher than those in the almost "empty" simulated events. This implies that tracks will overlap, so that their deposited charges will add up on the detector pads. In particular, tracks of different particle species will overlap. Consequently, such effects will worsen the PID performance (also see [42]).
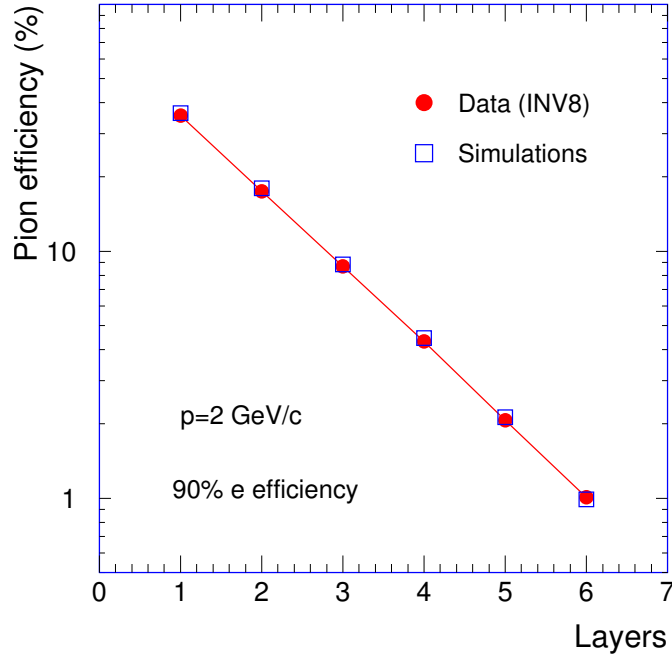
Figure 5.6.: Pion efficiency as a function of the number of layers at momentum 2 GeV/c. The data points stem from test beam measurements [61]. As a rule of thumb, each layer reduces the pion efficiency by roughly a factor 2 [58].

5.12.1. Comparison to Real Data

The PID performance results have been compared with those obtained from real data [71] from 2010. Regrettably, real data shows a worse PID performance. A pion suppression of about 5 for 90% electron efficiency and about 11 for 80% electron efficiency was found for the following settings: no tail cancellation, SW 2-26, summation method, only pions and cut on momenta ≥ 1.5 GeV/c[11]. On average, the drift velocity has been about 1.42 cm/μs for the used runs, but quite some fluctuations are expected. The LUT and the threshold t_e have been adjusted to this situation. Also, the tracklet length and tilt correction have been applied.

In more detail, the fully reconstructed data of the offline analysis has been used, where e.g. the tail cancellation has already been applied. Next, these corrections have been undone to get as close as possible to raw data. The reason

---

[11]Note that the particles are taken from V^0's, which exhibit a slightly different p_t spectrum.

why raw data has not been used directly is statistics: There is only a very small fraction of electrons in the events and it would require too much memory and time to find a sufficient number of electrons in raw data. In contrast, the reconstructed data is much more compact and, hence, can be used instead of raw data to study the PID performance. The disadvantage is that the undo steps mentioned above have to be performed. However, note that the PID performance methods for real data are still under development [71].

It must be emphasized that the methods used for real data are different to that of the simulations. As a consequence, the results are not directly comparable and deviations are expected. Yet, the observed deviations seem to be too big, so that they presumably originate from another source. A long study has been carried out to find the reason for these discrepancies. Recent investigations [53] have shown that gas composition, gas gain and drift velocity exhibit strong fluctuations for the 2010 data. Hence, a strong decrease of the PID performance can be expected. Some further checks indicate that the worse pion rejection also seems to be related to pad row crossing, which is mainly present in non-central stacks. The simulations have been restricted to the central stack for the sake of complexity reduction. However, for the comparison, new simulations without restriction to the central stack have been carried out. In addition, a flat momentum distribution ranging from 1.5 to 5.0 GeV/c and a drift velocity of 1.42 cm/μs with corresponding LUT and threshold have been used in the simulation. Finally, the tracklet length and tilt correction have been enabled (as done in the hardware).

Indeed, the pion suppression was found to be about 10 for the same settings as used for the real data and for 90% electron efficiency. This is in acceptable agreement with the real data results, if the fluctuations in gas composition, gas gain and drift velocity for the real data are taken into account as well. When the same set of cuts as for the LUT creation is used for the PID performance, i.e. tracklets with pad row crossing are removed, a pion suppression of about 30 is reached, which is a factor of 3 better.

To sum up, pad row crossing seems to be one of the most important effects responsible for the much worse pion suppression in real data. Other possible reasons, besides fluctuations in gas composition, gas gain and drift velocity, are listed in section 5.12. Though, the investigation of this issue is still ongoing and there might be other effects.

In any case, it seems that the simulation yields similar results as found for real data, if all mentioned caveats are taken into account. These caveats should affect the results for all kind of settings (TC on/off, different summation windows, etc.) in the same way: Although the absolute values of the PID performance might be different for real data, the relative changes with the parameters should be the same (similar to the observations for the tracklets stage and the GTU tracks stage). As a result, the qualitative and quantitative impacts of the parameters, that have been explored in this thesis, can be related to real data with confidence.

6. Conclusion

The LHC has ushered in a new era of particle physics. With ALICE a detailed study of the quark-gluon plasma and its properties is possible. To enhance rare probes that are important to investigate, the ALICE Transition Radiation Detector (TRD) can be used as a dedicated trigger on high-p_t electrons and jets. The former trigger relies on a proper electron identification, which is based on the deposited charge of a particle in the TRD: A particle that traverses the TRD deposits energy due to the ionisation of the gas in the drift chambers. In addition, electrons traversing the radiator can produce transition radiation, that is absorbed in the drift region creating further clusters. These clusters significantly increase the total deposited charge. In this thesis, the likelihood method on total deposited charge (LQ) has been used to identify electrons. For this method, the deposited charge is summed over a defined interval of the total drift time. A typical summation window extends over the time bin range 2-26. Using Monte Carlo simulations, it can be determined how frequently a certain summed charge occurs for electrons and non-electrons. This allows for the definition of an electron likelihood as a function of the summed charge. The gathered information is stored in a Look-Up Table (LUT), which is used by the detector hardware (or the simulation of it) to quickly determine the Particle Identification (PID) information. With this method and using Monte Carlo simulations combined with hardware simulations, the best achievable pion suppression is found to be typically around 40 for an electron efficiency of 90%.

The summed charge depends on parameters like gas gain and drift velocity. However, a LUT can only be created for one fixed parameter set. The impact of parameter changes on the electron identification has been systematically studied in this thesis with Monte Carlo simulations. The results can be used to determine the trigger rates and how these change with parameters. For this, the particle abundance must be known. The corresponding estimations will be carried out in [63].

What else can be learnt from the results of this thesis? It was found that the gas gain changes dominate the impact on the PID performance and that a change in the drift velocity gives also quite some effect. Since the pressure inside the TRD chambers relative to the ambient one is kept constant, unavoidable changes of the atmospheric pressure lead to absolute pressure and, thus, gas gain variations in the chambers. According to Monte Carlo simulations, a relative change of the gas gain of +5% causes a relative change of the pion suppression of about −36%. As

6. Conclusion

a result, this increases the fake rate of the TRD trigger. In order not to increase the fake rate too much, the relative gas gain change should not exceed a threshold of about +5% or smaller.

It was demonstrated that a drift velocity change by ±0.1 cm/μs, i.e. about ±7% relative change with respect to 1.5 cm/μs, leads to a relative change of the pion suppression by approximately 10-20% for a summation window ranging over time bins 2-26. Hence, the drift velocity has been found to be less critical for the PID performance than the gas gain, but has still a considerable impact.

Fortunately, the high-voltage can be adjusted to compensate the pressure changes. There are two high-voltages: one determining the drift velocity and another one affecting the gas gain. Fig. 6.1 shows how the latter high-voltage setting is related to the gas gain.
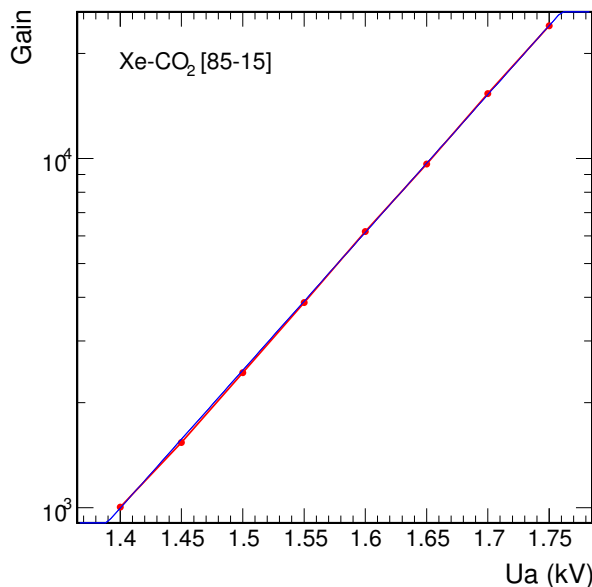
Figure 6.1.: Gain as a function of the anode voltage for a gas mixture of 85% Xenon and 15% CO_2. The red dots are the data points from the measurement connected with a trend line (red), while the blue line is a fit through these points. Note that this measurement was performed for a slightly different wire geometry than that of the ALICE TRD [64] (see [73] for further information).

During summer 2011 a high-voltage adjustment for the drift velocity has been introduced and an adjustment of the high-voltage for the amplification is also planned [74]. The idea is that these adjustments help to keep the electron identification as stable as possible. The adjustment for the drift voltage stabilises the drift velocity to the nominal value of 1.5 cm/μs, whereas the high-voltage adjustment for the amplification is designed to keep all chambers at the same constant gas gain.

Though, the overall gain for single pads of a chamber might be different. This issue is foreseen to be solved by the use of online gain tables. These tables contain gain correction factors for each ADC-channel and can be loaded into the TRAPs to obtain a corrected summed charge. The correction factors were obtained during a run in which ^{83m}Kr, that emits electrons with a well-known energy spectrum, is added to the gas. A detailed description of the Krypton calibration is provided in [75, 76].

Whether the Tail Cancellation (TC) will be used, is still unclear. It is known that the TC yields better results for the determination of the tracklet inclination because the ion tails distort the result. In turn, this allows for a better tracklet matching by the Global Tracking Unit. Concerning PID performance, there are reasons for and against TC, that also depend on the chosen summation window. However, if the drift velocity can be kept stable and the summation window ranging over time bins 2-26, i.e. the whole drift time, can be used, the Monte Carlo simulations suggest to activate the tail cancellation. If for any reason only a summation over a time bin interval smaller than the drift time is chosen, the simulations favour running without tail cancellation.

In general, the PID performance obtained by Monte Carlo simulations suggests to sample over the whole drift time. However, the time for a level 1 trigger contribution is very limited. Despite of the optimisation of the calculation algorithms in the hardware, the required total processing time for the calculation of the tracks is at the upper limit. It might happen that fewer than 27 time bins (time bins 0-26) will be used in future. Note that the drift high-voltage will be adjusted to achieve a sufficiently high and stable drift velocity, such that there will be no cut into the signal.

It was also shown that the likelihood combination method would give the best PID performance. Unfortunately, the time argument from above also forbids the use of the likelihood combination method. That is why the summation method has been chosen instead, which exhibits a similar processing time as the multiplication method, but has a much better PID performance than the latter.

An advanced application of the electron identification at trigger level could be the measurement of the Υ — an important probe for the study of the quark-gluon plasma. To gather adequate statistics for Υ physics with ALICE, a trigger on Υ decays is needed. The di-electron decay channel is suitable for this purpose because the TRD can be used to identify and trigger on the daughter particles at level 1. Yet, to achieve a reasonable level 1 trigger rate requires a good input sample. Such an input sample could be obtained by a suitable pre-selection at level 0. In the first part of the thesis, the feasibility of an Υ topology level 0 trigger with data from the TOF detector has been studied. It was found that such a trigger yields only reasonable rates, if it is configured to respond only to

Υ's decaying at rest. But even in this case and under very optimistic assumptions, the level 0 trigger rate is expected to be reduced only by a factor 2 compared to a minimum bias trigger.

It was also discussed that a trigger on Υ's in a rather broad transverse momentum region, e.g. $0 \text{ GeV}/c \leq p_t \leq 2 \text{ GeV}/c$, requires a tolerance > 0 for the topology trigger. However, it was demonstrated that uncorrelated hits cause a background of about 80% in this case. This means that there is almost no reduction of the trigger rate compared to a minimum bias trigger.

In summary, an Υ topology level 0 trigger with data from the TOF detector is, if at all, only feasible for Υ's decaying at rest.

Appendix A.

The ALICE Coordinate System

The ALICE coordinate system is defined as a right-handed orthogonal Cartesian coordinate system with point of origin $(x, y, z = 0)$ at the nominal beam interaction point (IP) [77], see Fig. A.1.
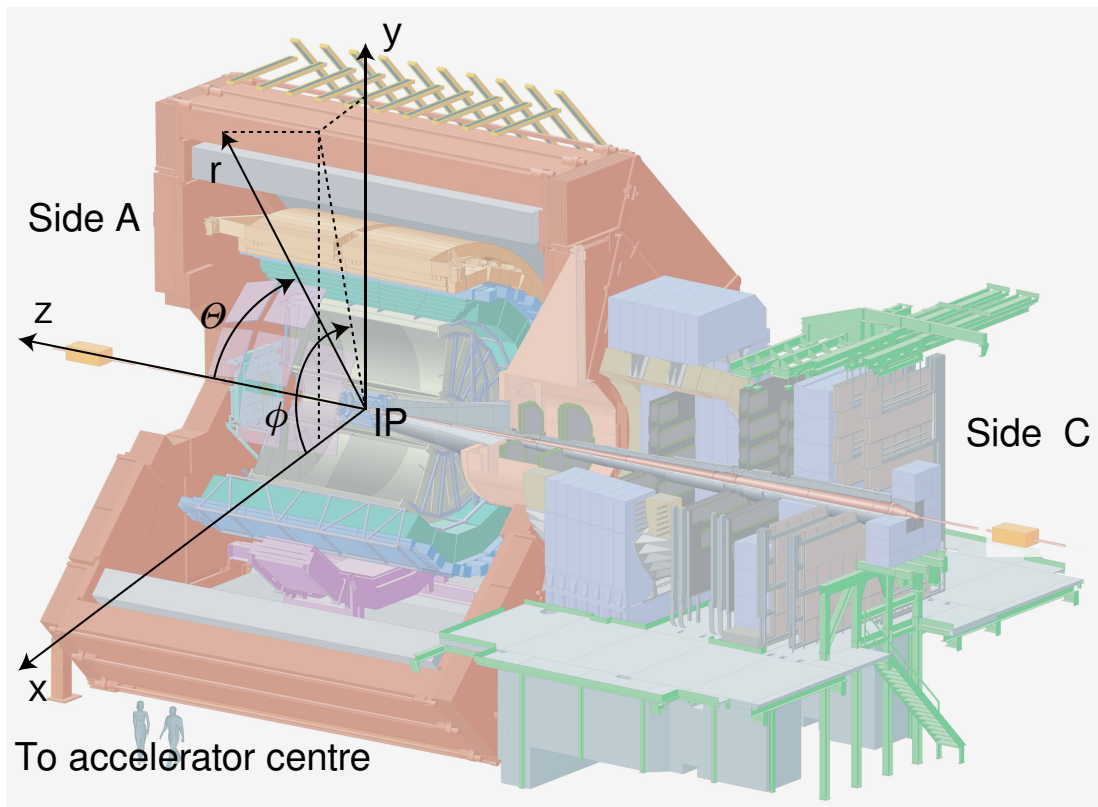
Figure A.1.: Definition of the ALICE Coordinate System: The origin sits at the nominal beam interaction point (IP). The axes are defined in the text [77].

The axes and angles are defined as follows:

- x-**axis**: axis in the horizontal plane perpendicular to the mean beam direction and pointing towards the accelerator centre

Appendix A. The ALICE Coordinate System

- y-**axis**: axis perpendicular to the x-axis and the mean beam direction pointing upwards

- z-**axis**: axis parallel to the beam direction with positive z from the point of origin towards side A. The muon arm is located at negative z

- **azimuthal angle** ϕ: increases counter-clockwise from x ($\phi = 0$) to y ($\phi = \pi/2$) with the observer standing at positive z and looking towards side C

- **polar angle** Θ: increases from z ($\Theta = 0$) passing the x-y plane ($\Theta = \pi/2$) to $-z$ ($\Theta = \pi$)

Appendix B.

Settings for the MCM Simulation

In the MCM simulation, the following settings have been used:

- The magnetic field has been configured to 0.5 T.

- $\omega \cdot \tau$ (this equals the tangent of the Lorentz angle) is calculated with this field using the class *AliTRDCommonParam* and assuming a nominal drift velocity of 1.5 cm/μs.

- Tilt and tracklet length correction have been disabled, since they are not needed for the central stack and would introduce unnecessary complexity.

- The DMEM was accessed directly to adjust the number of drift time bins used for the calculation of the deflection (fgkDmemAddrNdrift):

  $24 \cdot 2^5$ (no TC), $20 \cdot 2^5$ (with TC)[1]. In case of TC turned off, the number of drift time bins is increased to (partially) resolve the problem with ion tails for the fit. This is a kind of heuristic solution because it was observed that the ion tails lead to tracklets that are too perpendicular to the chamber and that the presented values yield better results.

Tab. B.1 summarises the values of the TRAP registers used for the simulation. All registers that are not listed here have been set to their initialisation value.

---

[1]The factor 2^5 corresponds to a bit shift to get the correct digit precision.

Register	Value	Description
C13CPUA	30	Number of time bins
FTAL	200	Weight of the long component for TC
FTLS	0	Decay constant of the short component for TC
FTLL	200	Decay constant of the long component for TC
TPCL	2	Hit number threshold for the left channel
TPCT	10	Total hit number threshold for both channels
TPFS	2	Start time bin for the preprocessor's linear fit
TPFE	22	End time bin for the preprocessor's linear fit plus 1 time bin
TPQS0	2	Time bin with start of summation window for charge Q_0
TPQE0	22 (SW 2-21) 27 (SW 2-26)	Time bin with end of summation window for charge Q_0 plus 1 time bin
TPQS1	22 (SW 2-21) 27 (SW 2-26)	Time bin with start of summation window for charge Q_1
TPQE1	27	Time bin with end of summation window for charge Q_1 plus 1 time bin
FPBY	0	Pedestal correction filter bypass (active low)
TPVBY	0	Cluster Verification bypass (active low)
FTBY	0 (no TC) 1 (with TC)	TC filter bypass (active low)
TPFP	40 (no TC) 23 (with TC)	Filtered pedestal
TPHT	200 (no TC) 150 (with TC)	Cluster charge threshold

Table B.1.: Used values for the TRAP registers in the simulation. All registers not listed here have been set to their initialisation value. *SW 2-21* indicates the case, where the time bins 2 to 21 have been used to sum up the charge Q_0. Respectively, *SW 2-26* uses the time bins 2 to 26 for this summation. In the former case, the remaining time bins are added to Q_1. However, Q_1 has not been used for the analysis. A more detailed description of the TRAP registers is provided in [47].

Appendix C.

Settings for the GTU Simulation

For the GTU simulation, the search windows have been adjusted using the class *AliTRDgtuParam* as follows [78]:

- The Y window *deltaY* is set to $9 \cdot 4$. This is 4 times the originally assumed value for *pp* collisions and corresponds to a window size of $0.011625 \cdot 4$ m.

- For the deflection angle window *deltaAlpha*, the value $11 \cdot 2$ has been used. Again, this window is enlarged by a factor of 2 compared to the original suggestion. This defines a deflection angle window of size $0.05 \cdot 2$ rad.

The stated parameters correspond to the search windows in the projection plane mentioned in section 2.5. The values are equal to those that are used in the experiment for *pp* collisions at the moment. The search windows have been opened by the given factors because as many tracklets as possible shall be matched. Later, if the matching has proven to work, the size of the windows can be decreased again.

Appendix D.

Collection of all PID Performance Results

The PID performance results for different combination methods (multiplication, summation and likelihood) are shown in the following figures and tables grouped by particle momenta. The column SW of the tables states which time bin range is used for the summation of the charge Q_0. Further details, a discussion of the results and the error estimation is presented in chapter 5.

The LUT and the threshold are always those for normal gas gain 4000 and drift velocity 1.5 cm/μs. But LUT and threshold are calculated separately for TC on/off, for different summation windows and for each combination method for these nominal conditions.

Each table shows the PID performance results compared for different drift velocities and various gas gains. In both cases, the results are presented for different summation windows and for TC on/off.

To save some space, the captions of the tables have been kept as short as possible. Each table lists the PID performance results for:

- a certain particle momentum.

- the stage for which the results have been obtained (see section 4.2). This can either be the stage of *tracklets* or that of *GTU tracks*.

- the species that have been taken into account besides electrons. In case of *only pions*, only pions are used as non-electrons, whereas in case of *all*, pions, muons, kaons and protons are used.

- the combination method that has been used to combine the tracklet electron likelihoods to the one of a track (cf. section 4.1.2): *multiplication*, *summation*, *likelihood*.

The table's caption contains this information in exactly this order, for instance: 5.0 GeV/c, tracklets, only pions, summation.

D.1. Results for 3.0 GeV/c Particles
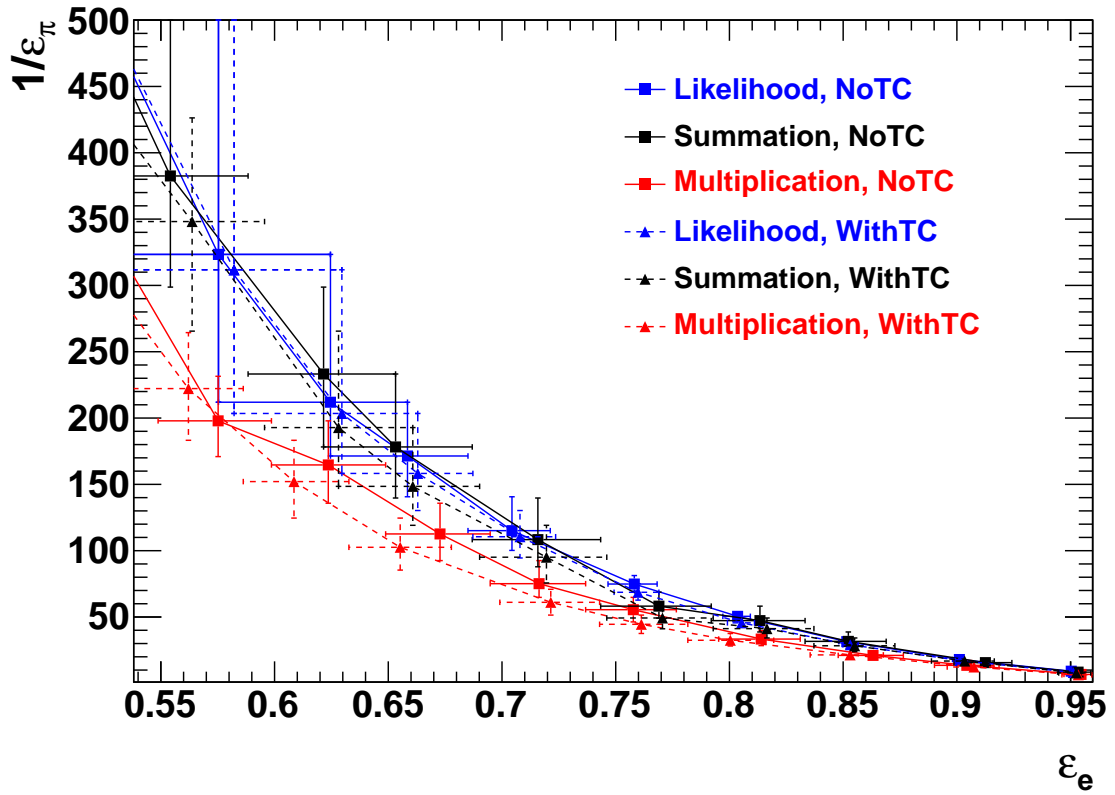
Figure D.1.: Pion suppression as a function of electron efficiency for the tracklets stage, 3 GeV/c, only pions, SW 2-21 and normal gas gain and drift velocity. The curves are just trend lines (no fits!) through the data points and are coloured differently for the different combination methods: likelihood (blue), summation (black), multiplication (red). Data for TC off is illustrated by solid lines and squares, data for TC on by broken lines and triangles. For further details, refer to Fig. 5.2 (p. 86) and to the discussion in the text.
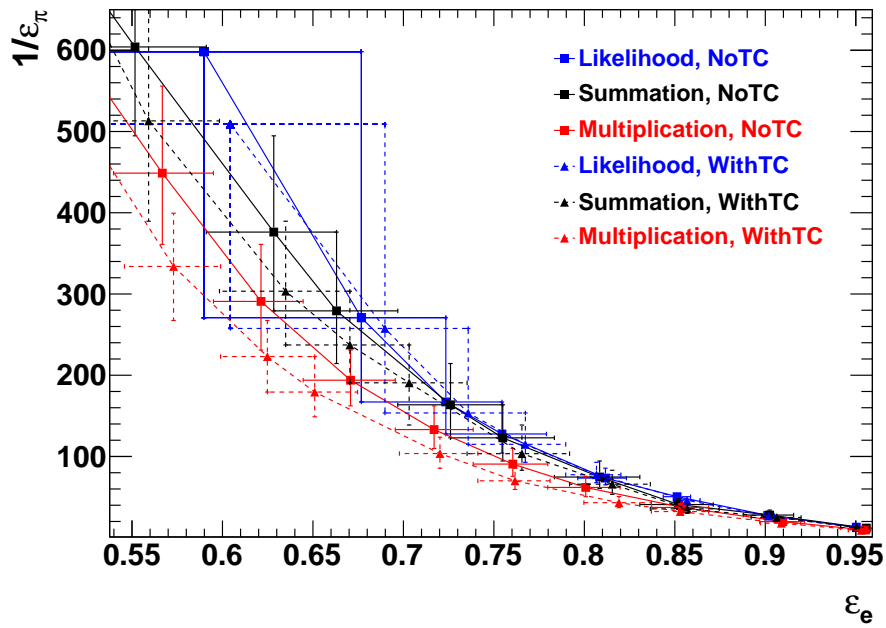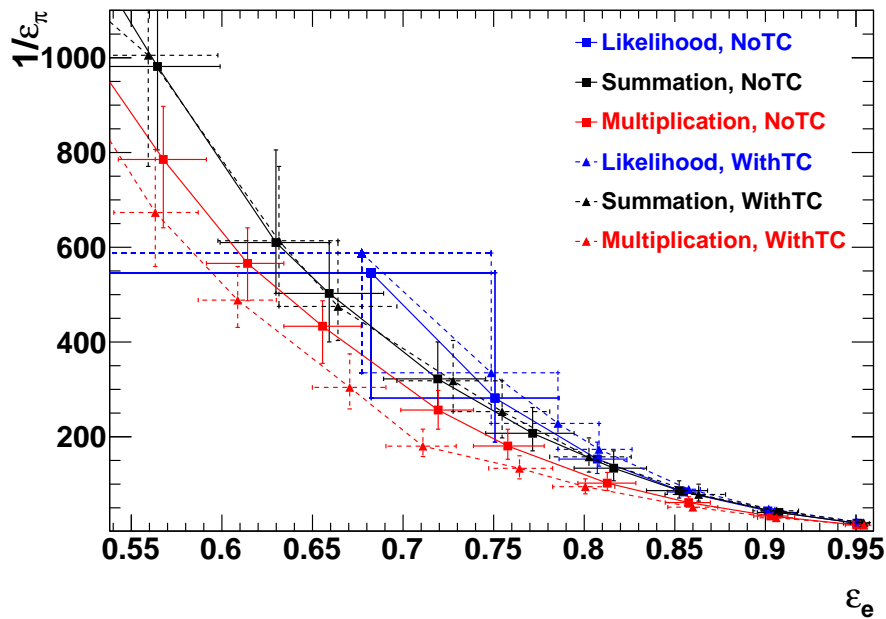
(a) SW 2-21

(b) SW 2-26

Figure D.2.: Pion suppression as a function of electron efficiency for the GTU tracks stage, 3 GeV/c, only pions, normal gas gain and drift velocity and **a)** SW 2-21 and **b)** SW 2-26. The curves are just trend lines (no fits!) through the data points and are coloured differently for the different combination methods: likelihood (blue), summation (black), multiplication (red). Data for TC off is illustrated by solid lines and squares, data for TC on by broken lines and triangles. For further details, refer to Fig. 5.2 (p. 86) and to the discussion in the text.

Settings		Drift velocity	Effective electron	Pion suppression
TC	SW	[cm/μs]	efficiency [%]	
Off	2-21	1.4	$84.7^{+1.6}_{-1.7}$	$21.1^{+4.1}_{-3.2}$
		1.5	$90.4^{+1.2}_{-1.4}$	$13.6^{+2.0}_{-1.9}$
		1.6	$93.45^{+0.89}_{-0.95}$	$9.7^{+1.5}_{-1.2}$
On	2-21	1.4	$84.8^{+1.6}_{-1.5}$	$18.2^{+2.9}_{-2.5}$
		1.5	$90.8^{+1.1}_{-1.2}$	$12.3^{+1.7}_{-1.5}$
		1.6	$93.09^{+0.91}_{-0.90}$	$9.4^{+1.3}_{-1.1}$
Off	2-26	1.4	$90.5^{+1.0}_{-1.1}$	$31.8^{+5.3}_{-5.0}$
		1.5	$90.0^{+1.1}_{-1.1}$	$28.4^{+4.3}_{-4.1}$
		1.6	$89.9^{+1.1}_{-1.1}$	$27.1^{+3.9}_{-3.6}$
On	2-26	1.4	$92.93^{+0.80}_{-0.94}$	$20.5^{+2.9}_{-2.7}$
		1.5	$90.9^{+0.9}_{-1.1}$	$25.7^{+3.8}_{-3.0}$
		1.6	$87.9^{+1.1}_{-1.2}$	$31.7^{+5.0}_{-3.9}$

Settings		Gas gain	Effective electron	Pion suppression
TC	SW	[arb. unit]	efficiency [%]	
Off	2-21	3600	$82.3^{+1.7}_{-2.0}$	$39.2^{+7.9}_{-6.2}$
		4000	$90.6^{+1.2}_{-1.2}$	$13.1^{+2.2}_{-1.7}$
		4200	$93.37^{+0.84}_{-0.98}$	$8.9^{+1.2}_{-1.2}$
		4400	$95.23^{+0.73}_{-0.72}$	$5.89^{+0.76}_{-0.61}$
On	2-21	3600	$82.5^{+1.7}_{-1.8}$	$33.2^{+6.3}_{-5.0}$
		4000	$90.5^{+1.1}_{-1.3}$	$12.6^{+1.6}_{-1.5}$
		4200	$93.01^{+0.98}_{-0.87}$	$8.4^{+1.1}_{-1.0}$
		4400	$94.63^{+0.69}_{-0.81}$	$5.87^{+0.70}_{-0.57}$
Off	2-26	3600	$82.0^{+1.8}_{-1.7}$	100^{+21}_{-14}
		4000	$90.1^{+1.2}_{-1.2}$	$29.0^{+4.3}_{-4.2}$
		4200	$93.29^{+0.85}_{-0.93}$	$17.7^{+2.8}_{-2.3}$
		4400	$94.80^{+0.64}_{-0.70}$	$11.0^{+1.6}_{-1.4}$
On	2-26	3600	$82.0^{+1.5}_{-1.6}$	89^{+15}_{-13}
		4000	$90.2^{+1.1}_{-1.1}$	$28.0^{+4.5}_{-3.6}$
		4200	$93.12^{+0.71}_{-0.88}$	$17.5^{+2.4}_{-2.2}$
		4400	$94.63^{+0.63}_{-0.64}$	$11.2^{+1.5}_{-1.2}$

Table D.1.: 3.0 GeV/c, tracklets, only pions, multiplication.

Settings		Drift velocity	Effective electron	Pion suppression
TC	SW	[cm/μs]	efficiency [%]	
Off	2-21	1.4	$85.5^{+1.8}_{-1.9}$	$24.0^{+5.2}_{-4.2}$
		1.5	$91.3^{+1.2}_{-1.4}$	$15.6^{+3.0}_{-2.3}$
		1.6	$94.33^{+0.84}_{-0.88}$	$11.4^{+1.9}_{-1.5}$
On	2-21	1.4	$83.9^{+1.8}_{-1.9}$	$24.5^{+4.9}_{-3.9}$
		1.5	$90.3^{+1.3}_{-1.5}$	$16.8^{+3.1}_{-2.6}$
		1.6	$93.2^{+0.9}_{-1.1}$	$13.0^{+2.3}_{-1.9}$
Off	2-26	1.4	$90.4^{+1.3}_{-1.4}$	$40.7^{+7.6}_{-7.2}$
		1.5	$90.1^{+1.2}_{-1.3}$	$36.9^{+6.9}_{-6.3}$
		1.6	$90.2^{+1.1}_{-1.3}$	$33.4^{+6.7}_{-4.7}$
On	2-26	1.4	$92.4^{+1.0}_{-1.2}$	$31.6^{+6.3}_{-5.0}$
		1.5	$90.3^{+1.2}_{-1.4}$	$40.6^{+8.3}_{-6.4}$
		1.6	$87.9^{+1.4}_{-1.5}$	$48.9^{+9.7}_{-8.0}$

Settings		Gas gain	Effective electron	Pion suppression
TC	SW	[arb. unit]	efficiency [%]	
Off	2-21	3600	$80.3^{+2.0}_{-2.2}$	54^{+11}_{-11}
		4000	$90.2^{+1.1}_{-1.5}$	$18.6^{+3.2}_{-3.1}$
		4200	$93.0^{+1.0}_{-1.1}$	$12.1^{+2.1}_{-1.8}$
		4400	$95.42^{+0.58}_{-0.91}$	$8.1^{+1.2}_{-1.0}$
On	2-21	3600	$81.3^{+2.0}_{-2.1}$	$44.4^{+8.8}_{-8.1}$
		4000	$90.2^{+1.3}_{-1.4}$	$17.0^{+3.3}_{-2.4}$
		4200	$93.1^{+0.9}_{-1.2}$	$11.1^{+1.8}_{-1.6}$
		4400	$94.90^{+0.78}_{-0.79}$	$7.6^{+1.2}_{-1.0}$
Off	2-26	3600	$81.1^{+1.8}_{-2.0}$	114^{+25}_{-22}
		4000	$90.2^{+1.3}_{-1.2}$	$36.7^{+7.4}_{-5.6}$
		4200	$93.30^{+0.86}_{-0.94}$	$23.1^{+3.5}_{-3.4}$
		4400	$95.24^{+0.58}_{-0.81}$	$14.3^{+2.5}_{-2.0}$
On	2-26	3600	$81.3^{+1.8}_{-2.2}$	117^{+24}_{-20}
		4000	$90.6^{+1.1}_{-1.4}$	$42.1^{+7.5}_{-6.9}$
		4200	$93.5^{+0.9}_{-1.1}$	$25.1^{+3.9}_{-3.7}$
		4400	$95.16^{+0.73}_{-0.75}$	$16.2^{+2.6}_{-2.4}$

Table D.2.: 3.0 GeV/c, tracklets, only pions, summation.

Settings		Drift velocity	Effective electron	Pion suppression
TC	SW	[cm/μs]	efficiency [%]	
Off	2-21	1.4	$83.84^{+0.27}_{-0.27}$	$28.22^{+0.89}_{-0.67}$
		1.5	$90.11^{+0.19}_{-0.30}$	$17.95^{+0.42}_{-0.38}$
		1.6	$93.60^{+0.15}_{-0.12}$	$12.92^{+0.31}_{-0.28}$
On	2-21	1.4	$83.54^{+0.30}_{-0.25}$	$25.64^{+0.73}_{-0.61}$
		1.5	$90.13^{+0.19}_{-0.19}$	$17.23^{+0.51}_{-0.40}$
		1.6	$93.04^{+0.15}_{-0.17}$	$13.24^{+0.34}_{-0.27}$
Off	2-26	1.4	$90.24^{+0.22}_{-0.26}$	$41.8^{+1.3}_{-1.5}$
		1.5	$90.05^{+0.19}_{-0.24}$	$38.0^{+1.2}_{-1.1}$
		1.6	$89.94^{+0.20}_{-0.25}$	$35.2^{+1.2}_{-0.9}$
On	2-26	1.4	$92.06^{+0.22}_{-0.22}$	$33.4^{+1.3}_{-1.1}$
		1.5	$90.23^{+0.17}_{-0.25}$	$42.5^{+1.2}_{-1.6}$
		1.6	$87.38^{+0.24}_{-0.22}$	$50.7^{+1.4}_{-1.5}$

Settings		Gas gain	Effective electron	Pion suppression
TC	SW	[arb. unit]	efficiency [%]	
Off	2-21	3600	$80.12^{+0.29}_{-0.28}$	$54.5^{+1.4}_{-1.9}$
		4000	$90.06^{+0.16}_{-0.22}$	$18.72^{+0.60}_{-0.47}$
		4200	$92.98^{+0.11}_{-0.12}$	$12.20^{+0.28}_{-0.24}$
		4400	$95.277^{+0.095}_{-0.086}$	$8.02^{+0.17}_{-0.17}$
On	2-21	3600	$81.29^{+0.28}_{-0.30}$	$45.3^{+1.0}_{-1.5}$
		4000	$90.22^{+0.18}_{-0.24}$	$17.13^{+0.41}_{-0.32}$
		4200	$93.01^{+0.14}_{-0.12}$	$11.28^{+0.28}_{-0.27}$
		4400	$94.91^{+0.10}_{-0.09}$	$7.67^{+0.17}_{-0.12}$
Off	2-26	3600	$81.17^{+0.30}_{-0.35}$	$119.0^{+4.4}_{-3.7}$
		4000	$90.21^{+0.25}_{-0.28}$	$36.4^{+1.4}_{-0.9}$
		4200	$93.25^{+0.13}_{-0.13}$	$22.97^{+0.66}_{-0.63}$
		4400	$95.14^{+0.12}_{-0.10}$	$14.54^{+0.36}_{-0.40}$
On	2-26	3600	$81.07^{+0.33}_{-0.38}$	$125.4^{+4.7}_{-1.7}$
		4000	$90.25^{+0.19}_{-0.26}$	$43.0^{+1.4}_{-1.7}$
		4200	$93.30^{+0.18}_{-0.22}$	$25.48^{+0.61}_{-0.69}$
		4400	$95.06^{+0.13}_{-0.15}$	$16.68^{+0.44}_{-0.40}$

Table D.3.: 3.0 GeV/c, tracklets, only pions, likelihood.

Settings		Drift velocity	Effective electron	Pion suppression
TC	SW	[cm/μs]	efficiency [%]	
Off	2-21	1.4	$85.3^{+1.5}_{-1.4}$	$23.5^{+3.7}_{-3.1}$
		1.5	$90.9^{+1.0}_{-1.2}$	$15.2^{+2.1}_{-1.9}$
		1.6	$93.57^{+0.71}_{-0.88}$	$11.1^{+1.4}_{-1.2}$
On	2-21	1.4	$84.4^{+1.3}_{-1.6}$	$21.7^{+3.1}_{-2.7}$
		1.5	$90.3^{+1.0}_{-1.1}$	$14.7^{+1.8}_{-1.7}$
		1.6	$92.55^{+0.86}_{-0.87}$	$11.5^{+1.3}_{-1.2}$
Off	2-26	1.4	$91.2^{+1.1}_{-1.0}$	$32.2^{+4.8}_{-4.3}$
		1.5	$90.9^{+1.0}_{-1.0}$	$29.1^{+4.0}_{-3.8}$
		1.6	$90.61^{+0.87}_{-0.98}$	$28.2^{+4.0}_{-3.5}$
On	2-26	1.4	$92.43^{+0.82}_{-0.81}$	$23.8^{+2.8}_{-2.6}$
		1.5	$90.2^{+0.9}_{-1.1}$	$29.9^{+3.7}_{-3.3}$
		1.6	$87.1^{+1.1}_{-1.2}$	$36.8^{+4.8}_{-4.2}$

Settings		Gas gain	Effective electron	Pion suppression
TC	SW	[arb. unit]	efficiency [%]	
Off	2-21	3600	$83.2^{+1.6}_{-1.7}$	$40.8^{+7.3}_{-6.0}$
		4000	$90.9^{+1.0}_{-1.1}$	$14.7^{+2.0}_{-1.8}$
		4200	$93.50^{+0.79}_{-0.92}$	$10.0^{+1.3}_{-1.1}$
		4400	$95.29^{+0.62}_{-0.72}$	$7.03^{+0.77}_{-0.67}$
On	2-21	3600	$83.5^{+1.5}_{-1.6}$	$30.3^{+4.1}_{-3.9}$
		4000	$90.9^{+0.9}_{-1.2}$	$12.6^{+1.5}_{-1.3}$
		4200	$93.22^{+0.78}_{-0.82}$	$9.02^{+0.95}_{-0.88}$
		4400	$94.67^{+0.62}_{-0.65}$	$6.56^{+0.62}_{-0.58}$
Off	2-26	3600	$83.8^{+1.4}_{-1.6}$	95^{+16}_{-13}
		4000	$90.9^{+1.1}_{-1.0}$	$28.8^{+4.4}_{-3.6}$
		4200	$93.74^{+0.75}_{-0.82}$	$18.1^{+2.4}_{-2.1}$
		4400	$95.07^{+0.56}_{-0.55}$	$11.9^{+1.4}_{-1.3}$
On	2-26	3600	$82.9^{+1.5}_{-1.5}$	76^{+11}_{-10}
		4000	$90.5^{+1.0}_{-1.1}$	$27.0^{+3.4}_{-3.1}$
		4200	$93.12^{+0.74}_{-0.88}$	$17.7^{+2.1}_{-1.9}$
		4400	$94.44^{+0.69}_{-0.59}$	$11.9^{+1.3}_{-1.1}$

Table D.4.: 3.0 GeV/c, tracklets, all, multiplication.

Settings		Drift velocity	Effective electron	Pion suppression
TC	SW	[cm/μs]	efficiency [%]	
Off	2-21	1.4	$85.4^{+1.7}_{-1.8}$	$31.9^{+6.5}_{-5.1}$
		1.5	$90.9^{+1.3}_{-1.2}$	$20.5^{+3.6}_{-3.0}$
		1.6	$94.06^{+0.85}_{-0.82}$	$15.0^{+2.4}_{-2.1}$
On	2-21	1.4	$83.7^{+1.8}_{-1.9}$	$31.2^{+5.8}_{-5.0}$
		1.5	$90.1^{+1.4}_{-1.4}$	$21.1^{+3.3}_{-3.2}$
		1.6	$93.0^{+0.9}_{-1.1}$	$16.3^{+2.9}_{-2.3}$
Off	2-26	1.4	$90.4^{+1.3}_{-1.3}$	$52.2^{+9.7}_{-8.5}$
		1.5	$90.1^{+1.1}_{-1.2}$	$47.0^{+8.9}_{-7.4}$
		1.6	$90.1^{+1.1}_{-1.3}$	$44.2^{+8.4}_{-6.6}$
On	2-26	1.4	$92.6^{+1.1}_{-1.1}$	$37.2^{+7.0}_{-5.5}$
		1.5	$90.6^{+1.1}_{-1.2}$	$47.2^{+8.9}_{-7.2}$
		1.6	$88.1^{+1.4}_{-1.5}$	58^{+12}_{-9}

Settings		Gas gain	Effective electron	Pion suppression
TC	SW	[arb. unit]	efficiency [%]	
Off	2-21	3600	$82.3^{+1.9}_{-2.0}$	56^{+12}_{-10}
		4000	$91.2^{+1.0}_{-1.2}$	$20.3^{+3.7}_{-2.9}$
		4200	$93.73^{+0.84}_{-0.87}$	$13.5^{+2.2}_{-1.8}$
		4400	$95.82^{+0.55}_{-0.70}$	$9.2^{+1.3}_{-1.1}$
On	2-21	3600	$81.5^{+2.0}_{-2.0}$	50^{+10}_{-8}
		4000	$90.3^{+1.3}_{-1.5}$	$20.0^{+3.6}_{-2.8}$
		4200	$92.9^{+1.0}_{-1.1}$	$13.6^{+2.2}_{-1.8}$
		4400	$94.88^{+0.70}_{-0.92}$	$9.5^{+1.4}_{-1.2}$
Off	2-26	3600	$81.3^{+1.9}_{-2.0}$	147^{+34}_{-27}
		4000	$90.1^{+1.2}_{-1.3}$	$46.8^{+9.5}_{-7.3}$
		4200	$93.3^{+0.8}_{-1.0}$	$29.1^{+5.0}_{-4.4}$
		4400	$95.00^{+0.65}_{-0.65}$	$18.5^{+3.1}_{-2.5}$
On	2-26	3600	$82.1^{+1.9}_{-2.1}$	126^{+29}_{-22}
		4000	$90.6^{+1.3}_{-1.3}$	$45.4^{+9.6}_{-7.6}$
		4200	$93.7^{+1.0}_{-1.1}$	$29.0^{+5.3}_{-4.6}$
		4400	$95.25^{+0.64}_{-0.94}$	$18.9^{+3.2}_{-2.7}$

Table D.5.: 3.0 GeV/c, tracklets, all, summation.

Settings		Drift velocity	Effective electron	Pion suppression
TC	SW	[cm/μs]	efficiency [%]	
Off	2-21	1.4	$83.99^{+0.30}_{-0.26}$	$35.8^{+1.1}_{-0.9}$
		1.5	$90.02^{+0.20}_{-0.23}$	$22.59^{+0.55}_{-0.62}$
		1.6	$93.44^{+0.16}_{-0.15}$	$16.31^{+0.39}_{-0.38}$
On	2-21	1.4	$83.70^{+0.25}_{-0.26}$	$31.36^{+0.84}_{-0.93}$
		1.5	$90.19^{+0.18}_{-0.25}$	$20.65^{+0.47}_{-0.47}$
		1.6	$92.94^{+0.16}_{-0.13}$	$16.00^{+0.40}_{-0.35}$
Off	2-26	1.4	$90.33^{+0.21}_{-0.24}$	$51.7^{+1.9}_{-1.8}$
		1.5	$90.04^{+0.26}_{-0.22}$	$46.7^{+1.9}_{-1.6}$
		1.6	$89.86^{+0.21}_{-0.27}$	$44.8^{+1.7}_{-1.5}$
On	2-26	1.4	$92.06^{+0.29}_{-0.38}$	$41.5^{+2.4}_{-2.2}$
		1.5	$90.11^{+0.37}_{-0.38}$	$51.8^{+2.7}_{-2.2}$
		1.6	$87.20^{+0.39}_{-0.42}$	$63.1^{+2.8}_{-2.9}$

Settings		Gas gain	Effective electron	Pion suppression
TC	SW	[arb. unit]	efficiency [%]	
Off	2-21	3600	$80.66^{+0.28}_{-0.30}$	$65.1^{+2.2}_{-1.8}$
		4000	$90.06^{+0.16}_{-0.16}$	$22.86^{+0.52}_{-0.56}$
		4200	$92.97^{+0.19}_{-0.20}$	$14.95^{+0.33}_{-0.31}$
		4400	$95.18^{+0.10}_{-0.08}$	$10.09^{+0.20}_{-0.19}$
On	2-21	3600	$81.40^{+0.25}_{-0.26}$	$50.7^{+1.4}_{-1.3}$
		4000	$90.05^{+0.22}_{-0.18}$	$19.84^{+0.46}_{-0.45}$
		4200	$92.88^{+0.16}_{-0.17}$	$13.48^{+0.27}_{-0.28}$
		4400	$94.69^{+0.10}_{-0.09}$	$9.37^{+0.20}_{-0.18}$
Off	2-26	3600	$81.85^{+0.34}_{-0.39}$	$142.4^{+5.6}_{-6.1}$
		4000	$90.27^{+0.29}_{-0.28}$	$44.8^{+1.6}_{-1.5}$
		4200	$93.31^{+0.21}_{-0.20}$	$27.56^{+0.84}_{-0.83}$
		4400	$95.05^{+0.12}_{-0.15}$	$17.69^{+0.52}_{-0.51}$
On	2-26	3600	$81.33^{+0.36}_{-0.40}$	$142.1^{+6.6}_{-5.0}$
		4000	$90.00^{+0.21}_{-0.33}$	$47.2^{+2.0}_{-1.8}$
		4200	$93.03^{+0.14}_{-0.18}$	$29.91^{+0.94}_{-0.84}$
		4400	$94.70^{+0.12}_{-0.15}$	$19.42^{+0.58}_{-0.54}$

Table D.6.: 3.0 GeV/c, tracklets, all, likelihood.

Settings		Drift velocity	Effective electron	Pion suppression
TC	SW	[cm/μs]	efficiency [%]	
Off	2-21	1.4	$85.1^{+1.6}_{-1.8}$	$32.9^{+5.6}_{-4.8}$
		1.5	$91.0^{+1.2}_{-1.3}$	$19.8^{+3.3}_{-2.7}$
		1.6	$94.00^{+0.77}_{-0.89}$	$13.5^{+2.1}_{-1.8}$
On	2-21	1.4	$85.0^{+1.7}_{-1.8}$	$28.7^{+4.6}_{-3.8}$
		1.5	$90.9^{+1.1}_{-1.2}$	$17.9^{+2.6}_{-2.3}$
		1.6	$93.16^{+0.81}_{-0.98}$	$13.2^{+1.9}_{-1.6}$
Off	2-26	1.4	$89.7^{+1.1}_{-1.0}$	$36.9^{+6.4}_{-5.3}$
		1.5	$90.29^{+0.95}_{-0.94}$	$32.8^{+5.3}_{-4.5}$
		1.6	$90.8^{+0.9}_{-1.0}$	$30.5^{+5.2}_{-4.3}$
On	2-26	1.4	$92.11^{+0.89}_{-0.90}$	$23.5^{+3.5}_{-3.0}$
		1.5	$90.6^{+1.0}_{-1.0}$	$29.0^{+4.4}_{-3.4}$
		1.6	$89.0^{+1.1}_{-1.1}$	$34.4^{+5.5}_{-3.8}$

Settings		Gas gain	Effective electron	Pion suppression
TC	SW	[arb. unit]	efficiency [%]	
Off	2-21	3600	$81.9^{+1.8}_{-1.9}$	68^{+13}_{-11}
		4000	$91.0^{+1.1}_{-1.1}$	$19.6^{+3.7}_{-2.7}$
		4200	$93.64^{+0.76}_{-0.91}$	$12.1^{+1.8}_{-1.4}$
		4400	$95.40^{+0.57}_{-0.65}$	$7.8^{+1.2}_{-1.0}$
On	2-21	3600	$82.2^{+1.7}_{-1.9}$	56^{+11}_{-9}
		4000	$90.8^{+1.1}_{-1.2}$	$17.8^{+2.8}_{-2.2}$
		4200	$93.16^{+0.87}_{-0.90}$	$11.6^{+1.7}_{-1.4}$
		4400	$94.94^{+0.69}_{-0.71}$	$7.61^{+0.96}_{-0.85}$
Off	2-26	3600	$81.7^{+1.6}_{-1.6}$	121^{+23}_{-19}
		4000	$90.3^{+0.9}_{-1.0}$	$33.3^{+5.0}_{-4.6}$
		4200	$92.73^{+0.70}_{-0.80}$	$19.0^{+3.2}_{-2.4}$
		4400	$94.43^{+0.55}_{-0.67}$	$12.0^{+1.7}_{-1.6}$
On	2-26	3600	$82.3^{+1.6}_{-1.6}$	96^{+18}_{-15}
		4000	$90.8^{+0.8}_{-1.0}$	$29.3^{+4.5}_{-3.7}$
		4200	$93.17^{+0.70}_{-0.74}$	$17.9^{+2.7}_{-1.9}$
		4400	$94.69^{+0.60}_{-0.64}$	$11.5^{+1.5}_{-1.4}$

Table D.7.: 3.0 GeV/c, GTU tracks, only pions, multiplication.

Settings		Drift velocity	Effective electron	Pion suppression
TC	SW	[cm/μs]	efficiency [%]	
Off	2-21	1.4	$82.9^{+2.1}_{-2.2}$	$46.5^{+9.8}_{-8.0}$
		1.5	$90.2^{+1.3}_{-1.5}$	$27.9^{+6.2}_{-4.7}$
		1.6	$93.89^{+0.85}_{-0.94}$	$19.1^{+3.6}_{-3.0}$
On	2-21	1.4	$83.9^{+1.9}_{-2.1}$	$40.1^{+8.1}_{-7.3}$
		1.5	$90.6^{+1.3}_{-1.4}$	$24.9^{+4.9}_{-4.0}$
		1.6	$93.4^{+0.9}_{-1.1}$	$18.6^{+3.5}_{-3.0}$
Off	2-26	1.4	$90.0^{+1.3}_{-1.4}$	$46.0^{+8.3}_{-7.6}$
		1.5	$90.7^{+1.0}_{-1.2}$	$40.2^{+8.0}_{-6.9}$
		1.6	$91.4^{+1.0}_{-1.0}$	$37.3^{+7.4}_{-6.6}$
On	2-26	1.4	$91.9^{+1.1}_{-1.2}$	$35.7^{+7.5}_{-5.8}$
		1.5	$90.6^{+1.2}_{-1.3}$	$43.8^{+8.7}_{-7.1}$
		1.6	$89.1^{+1.3}_{-1.4}$	$53.6^{+9.4}_{-9.2}$

Settings		Gas gain	Effective electron	Pion suppression
TC	SW	[arb. unit]	efficiency [%]	
Off	2-21	3600	$79.2^{+2.3}_{-2.5}$	93^{+21}_{-20}
		4000	$90.3^{+1.4}_{-1.5}$	$27.1^{+6.2}_{-4.1}$
		4200	$93.4^{+0.8}_{-1.1}$	$17.3^{+3.1}_{-2.8}$
		4400	$95.32^{+0.72}_{-0.84}$	$11.0^{+1.9}_{-1.6}$
On	2-21	3600	$80.7^{+2.2}_{-2.4}$	75^{+18}_{-14}
		4000	$90.6^{+1.3}_{-1.5}$	$24.6^{+4.6}_{-3.9}$
		4200	$93.4^{+0.9}_{-1.1}$	$16.1^{+2.8}_{-2.4}$
		4400	$95.25^{+0.78}_{-0.85}$	$10.3^{+1.8}_{-1.5}$
Off	2-26	3600	$81.5^{+1.9}_{-2.0}$	132^{+32}_{-23}
		4000	$90.7^{+1.1}_{-1.2}$	$39.1^{+8.0}_{-5.9}$
		4200	$93.26^{+0.71}_{-0.84}$	$23.2^{+4.3}_{-3.2}$
		4400	$94.96^{+0.53}_{-0.67}$	$15.0^{+2.7}_{-2.1}$
On	2-26	3600	$81.3^{+1.9}_{-2.2}$	133^{+27}_{-25}
		4000	$90.5^{+1.1}_{-1.3}$	43^{+10}_{-6}
		4200	$93.5^{+0.9}_{-1.0}$	$27.1^{+5.4}_{-4.5}$
		4400	$94.96^{+0.83}_{-0.73}$	$17.3^{+2.9}_{-2.7}$

Table D.8.: 3.0 GeV/c, GTU tracks, only pions, summation.

Settings		Drift velocity	Effective electron	Pion suppression
TC	SW	[cm/μs]	efficiency [%]	
Off	2-21	1.4	$83.27^{+0.46}_{-0.51}$	$45.7^{+2.2}_{-2.1}$
		1.5	$90.13^{+0.35}_{-0.34}$	$27.5^{+1.2}_{-1.0}$
		1.6	$93.75^{+0.24}_{-0.22}$	$18.81^{+0.79}_{-0.68}$
On	2-21	1.4	$83.30^{+0.42}_{-0.49}$	$44.0^{+2.2}_{-1.4}$
		1.5	$90.19^{+0.32}_{-0.27}$	$26.7^{+1.1}_{-1.1}$
		1.6	$92.98^{+0.23}_{-0.25}$	$19.69^{+0.77}_{-0.82}$
Off	2-26	1.4	$89.50^{+0.35}_{-0.33}$	$50.5^{+2.5}_{-1.9}$
		1.5	$90.14^{+0.29}_{-0.34}$	$43.5^{+2.3}_{-1.5}$
		1.6	$90.66^{+0.24}_{-0.31}$	$40.5^{+1.9}_{-1.9}$
On	2-26	1.4	$91.41^{+0.24}_{-0.26}$	$40.2^{+2.0}_{-1.8}$
		1.5	$90.18^{+0.34}_{-0.28}$	$47.7^{+2.1}_{-2.1}$
		1.6	$88.45^{+0.35}_{-0.34}$	$56.9^{+2.4}_{-2.5}$

Settings		Gas gain	Effective electron	Pion suppression
TC	SW	[arb. unit]	efficiency [%]	
Off	2-21	3600	$79.46^{+0.45}_{-0.48}$	$91.3^{+3.4}_{-3.1}$
		4000	$90.22^{+0.33}_{-0.31}$	$26.9^{+1.2}_{-0.9}$
		4200	$93.28^{+0.19}_{-0.24}$	$16.78^{+0.58}_{-0.54}$
		4400	$95.13^{+0.20}_{-0.21}$	$10.69^{+0.39}_{-0.36}$
On	2-21	3600	$80.11^{+0.46}_{-0.49}$	$85.6^{+3.6}_{-4.1}$
		4000	$90.12^{+0.37}_{-0.26}$	$26.6^{+1.0}_{-0.9}$
		4200	$93.05^{+0.22}_{-0.26}$	$16.93^{+0.56}_{-0.58}$
		4400	$94.84^{+0.20}_{-0.18}$	$10.83^{+0.38}_{-0.37}$
Off	2-26	3600	$80.61^{+0.47}_{-0.52}$	$147.4^{+6.6}_{-6.3}$
		4000	$90.11^{+0.29}_{-0.32}$	$43.9^{+1.8}_{-1.4}$
		4200	$92.71^{+0.25}_{-0.22}$	$25.2^{+1.0}_{-1.1}$
		4400	$94.39^{+0.20}_{-0.17}$	$16.00^{+0.68}_{-0.51}$
On	2-26	3600	$81.02^{+0.48}_{-0.47}$	148^{+10}_{-11}
		4000	$90.23^{+0.30}_{-0.29}$	$47.6^{+1.8}_{-2.0}$
		4200	$93.17^{+0.16}_{-0.25}$	$27.7^{+1.2}_{-1.1}$
		4400	$94.82^{+0.16}_{-0.14}$	$17.61^{+0.75}_{-0.69}$

Table D.9.: 3.0 GeV/c, GTU tracks, only pions, likelihood.

Settings		Drift velocity	Effective electron	Pion suppression
TC	SW	[cm/μs]	efficiency [%]	
Off	2-21	1.4	$85.4^{+1.4}_{-1.6}$	$39.4^{+6.3}_{-5.2}$
		1.5	$90.8^{+1.1}_{-1.2}$	$22.9^{+3.4}_{-2.9}$
		1.6	$93.64^{+0.77}_{-0.82}$	$15.3^{+2.2}_{-1.9}$
On	2-21	1.4	$85.1^{+1.5}_{-1.5}$	$31.2^{+4.9}_{-3.8}$
		1.5	$90.6^{+1.0}_{-1.1}$	$20.4^{+2.8}_{-2.5}$
		1.6	$92.90^{+0.76}_{-0.89}$	$14.6^{+1.8}_{-1.6}$
Off	2-26	1.4	$90.0^{+0.9}_{-1.2}$	$42.8^{+6.4}_{-5.7}$
		1.5	$90.4^{+0.9}_{-1.1}$	$36.3^{+5.2}_{-4.6}$
		1.6	$90.66^{+0.83}_{-0.84}$	$33.3^{+5.1}_{-4.1}$
On	2-26	1.4	$92.03^{+0.80}_{-0.91}$	$26.7^{+3.1}_{-2.9}$
		1.5	$90.3^{+0.9}_{-1.0}$	$32.0^{+3.9}_{-3.6}$
		1.6	$88.6^{+1.0}_{-1.0}$	$38.7^{+5.1}_{-4.6}$

Settings		Gas gain	Effective electron	Pion suppression
TC	SW	[arb. unit]	efficiency [%]	
Off	2-21	3600	$82.4^{+1.7}_{-1.7}$	75^{+12}_{-11}
		4000	$90.9^{+0.9}_{-1.1}$	$22.1^{+3.4}_{-2.7}$
		4200	$93.31^{+0.86}_{-0.79}$	$14.0^{+1.9}_{-1.6}$
		4400	$94.98^{+0.67}_{-0.62}$	$9.6^{+1.2}_{-1.0}$
On	2-21	3600	$82.3^{+1.6}_{-1.8}$	$54.2^{+8.8}_{-7.0}$
		4000	$90.6^{+1.1}_{-1.1}$	$19.4^{+2.4}_{-2.2}$
		4200	$93.00^{+0.82}_{-0.90}$	$12.7^{+1.6}_{-1.3}$
		4400	$94.74^{+0.58}_{-0.78}$	$8.88^{+0.99}_{-0.87}$
Off	2-26	3600	$82.5^{+1.4}_{-1.5}$	127^{+26}_{-20}
		4000	$90.31^{+0.88}_{-0.96}$	$36.6^{+5.7}_{-4.5}$
		4200	$92.63^{+0.68}_{-0.76}$	$21.5^{+3.0}_{-2.6}$
		4400	$94.24^{+0.54}_{-0.61}$	$13.6^{+1.7}_{-1.5}$
On	2-26	3600	$82.2^{+1.3}_{-1.5}$	95^{+16}_{-12}
		4000	$90.49^{+0.89}_{-0.97}$	$31.8^{+3.5}_{-3.4}$
		4200	$92.80^{+0.74}_{-0.72}$	$20.2^{+2.4}_{-2.1}$
		4400	$94.45^{+0.57}_{-0.66}$	$13.1^{+1.4}_{-1.3}$

Table D.10.: 3.0 GeV/c, GTU tracks, all, multiplication.

Settings		Drift velocity	Effective electron	Pion suppression
TC	SW	[cm/μs]	efficiency [%]	
Off	2-21	1.4	$83.6^{+2.1}_{-2.3}$	59^{+12}_{-10}
		1.5	$90.3^{+1.5}_{-1.4}$	$35.4^{+7.0}_{-5.8}$
		1.6	$93.86^{+0.86}_{-0.95}$	$23.6^{+4.4}_{-3.7}$
On	2-21	1.4	$84.0^{+1.8}_{-2.3}$	50^{+10}_{-9}
		1.5	$90.6^{+1.4}_{-1.5}$	$32.5^{+6.3}_{-5.3}$
		1.6	$93.3^{+0.9}_{-1.1}$	$23.3^{+4.4}_{-3.6}$
Off	2-26	1.4	$90.1^{+1.3}_{-1.3}$	60^{+13}_{-10}
		1.5	$90.7^{+1.0}_{-1.0}$	51^{+10}_{-8}
		1.6	$91.4^{+1.0}_{-1.1}$	$46.4^{+8.9}_{-7.2}$
On	2-26	1.4	$92.3^{+0.9}_{-1.2}$	$42.6^{+8.4}_{-6.6}$
		1.5	$91.0^{+1.1}_{-1.2}$	$51.7^{+9.7}_{-8.2}$
		1.6	$89.4^{+1.2}_{-1.3}$	63^{+12}_{-10}

Settings		Gas gain	Effective electron	Pion suppression
TC	SW	[arb. unit]	efficiency [%]	
Off	2-21	3600	$80.0^{+2.2}_{-2.3}$	115^{+26}_{-22}
		4000	$90.6^{+1.3}_{-1.4}$	$33.2^{+6.7}_{-5.0}$
		4200	$93.39^{+0.84}_{-0.99}$	$21.0^{+3.7}_{-3.3}$
		4400	$95.25^{+0.77}_{-0.71}$	$14.0^{+2.4}_{-1.9}$
On	2-21	3600	$80.9^{+2.2}_{-2.4}$	88^{+21}_{-18}
		4000	$90.5^{+1.3}_{-1.5}$	$30.3^{+5.9}_{-4.8}$
		4200	$93.3^{+0.9}_{-1.1}$	$19.5^{+3.5}_{-3.0}$
		4400	$95.20^{+0.72}_{-0.93}$	$13.0^{+2.3}_{-1.8}$
Off	2-26	3600	$81.8^{+1.9}_{-2.0}$	165^{+37}_{-29}
		4000	$90.8^{+1.1}_{-1.1}$	51^{+10}_{-8}
		4200	$93.23^{+0.69}_{-0.86}$	$29.9^{+5.3}_{-4.3}$
		4400	$94.83^{+0.61}_{-0.63}$	$19.0^{+3.3}_{-2.6}$
On	2-26	3600	$81.9^{+1.8}_{-2.0}$	146^{+31}_{-23}
		4000	$90.8^{+1.0}_{-1.1}$	51^{+10}_{-9}
		4200	$93.7^{+0.8}_{-1.0}$	$31.6^{+5.9}_{-4.7}$
		4400	$95.29^{+0.55}_{-0.81}$	$20.3^{+3.5}_{-2.9}$

Table D.11.: 3.0 GeV/c, GTU tracks, all, summation.

Settings		Drift velocity	Effective electron	Pion suppression
TC	SW	[cm/μs]	efficiency [%]	
Off	2-21	1.4	$83.64^{+0.65}_{-0.65}$	$59.7^{+3.5}_{-3.4}$
		1.5	$90.06^{+0.41}_{-0.47}$	$35.2^{+2.0}_{-1.8}$
		1.6	$93.45^{+0.29}_{-0.29}$	$23.3^{+1.3}_{-1.1}$
On	2-21	1.4	$83.27^{+0.58}_{-0.62}$	$55.9^{+3.6}_{-3.2}$
		1.5	$90.04^{+0.45}_{-0.46}$	$35.1^{+2.2}_{-1.8}$
		1.6	$92.65^{+0.39}_{-0.37}$	$24.7^{+1.4}_{-1.3}$
Off	2-26	1.4	$89.75^{+0.42}_{-0.45}$	$63.7^{+4.2}_{-4.1}$
		1.5	$90.15^{+0.33}_{-0.41}$	$54.1^{+3.4}_{-2.8}$
		1.6	$90.57^{+0.34}_{-0.38}$	$49.6^{+2.9}_{-2.9}$
On	2-26	1.4	$91.44^{+0.59}_{-0.61}$	$51.4^{+5.8}_{-4.1}$
		1.5	$90.16^{+0.59}_{-0.59}$	$60.5^{+6.5}_{-5.0}$
		1.6	$88.41^{+0.59}_{-0.75}$	$72.3^{+8.6}_{-5.9}$

Settings		Gas gain	Effective electron	Pion suppression
TC	SW	[arb. unit]	efficiency [%]	
Off	2-21	3600	$80.05^{+0.67}_{-0.70}$	$115.1^{+7.9}_{-8.3}$
		4000	$90.14^{+0.43}_{-0.42}$	$33.1^{+2.1}_{-1.5}$
		4200	$93.05^{+0.32}_{-0.29}$	$20.5^{+1.1}_{-0.9}$
		4400	$94.93^{+0.22}_{-0.25}$	$13.82^{+0.67}_{-0.64}$
On	2-21	3600	$80.76^{+0.58}_{-0.58}$	$96.2^{+5.8}_{-6.6}$
		4000	$90.27^{+0.35}_{-0.35}$	$31.2^{+1.7}_{-1.4}$
		4200	$93.07^{+0.31}_{-0.30}$	$19.7^{+1.0}_{-0.8}$
		4400	$94.88^{+0.19}_{-0.22}$	$13.10^{+0.59}_{-0.55}$
Off	2-26	3600	$81.19^{+0.55}_{-0.66}$	181^{+18}_{-10}
		4000	$90.15^{+0.35}_{-0.45}$	$54.6^{+3.7}_{-2.8}$
		4200	$92.71^{+0.30}_{-0.34}$	$31.4^{+1.8}_{-1.5}$
		4400	$94.26^{+0.22}_{-0.23}$	$19.6^{+1.2}_{-0.8}$
On	2-26	3600	$81.50^{+0.87}_{-0.97}$	175^{+15}_{-15}
		4000	$90.47^{+0.54}_{-0.54}$	$55.4^{+5.5}_{-4.4}$
		4200	$93.30^{+0.38}_{-0.52}$	$33.3^{+2.7}_{-2.1}$
		4400	$94.95^{+0.34}_{-0.33}$	$21.0^{+1.6}_{-1.3}$

Table D.12.: 3.0 GeV/c, GTU tracks, all, likelihood.

D.2. Results for 5.0 GeV/c Particles

To obtain results for the PID performance of 5.0 GeV/c particles, the same LUTs as for 3.0 GeV/c particles have been used. The thresholds have also been adapted from the 3.0 GeV/c case, such that the electron efficiency is different from 90%, in general, also for the nominal conditions.
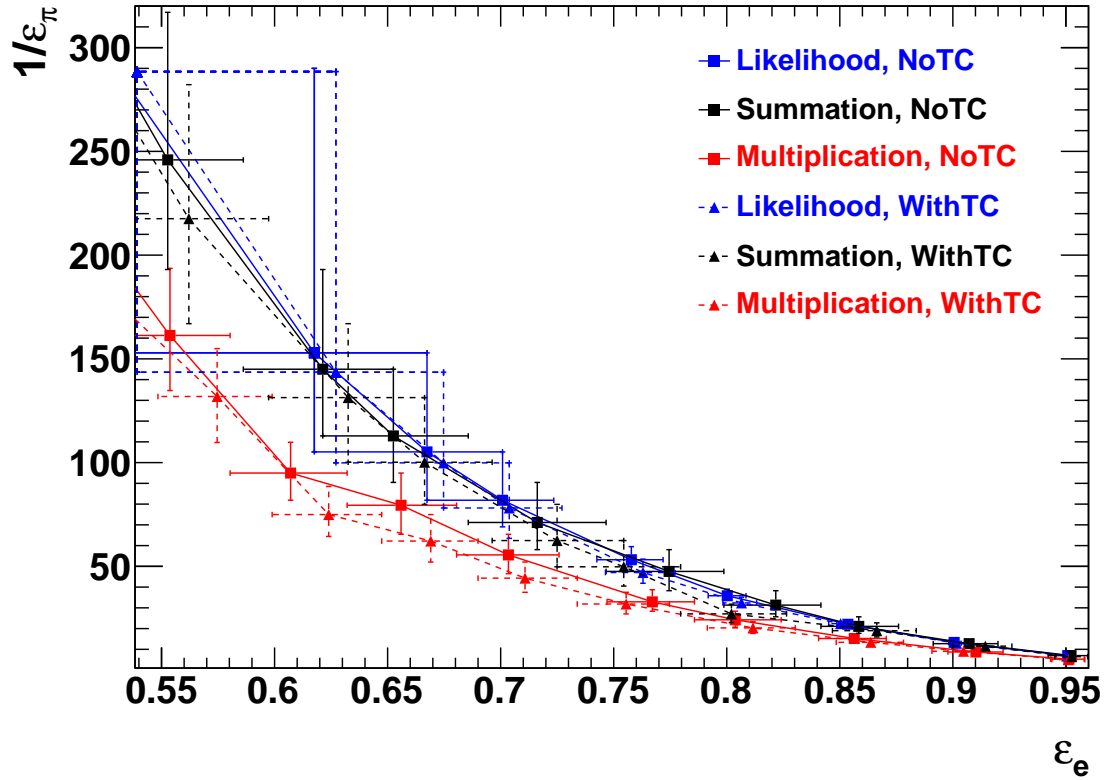
Figure D.3.: Pion suppression as a function of electron efficiency for the tracklets stage, 5 GeV/c, only pions, SW 2-21 and normal gas gain and drift velocity. The curves are just trend lines (no fits!) through the data points and are coloured differently for the different combination methods: likelihood (blue), summation (black), multiplication (red). Data for TC off is illustrated by solid lines and squares, data for TC on by broken lines and triangles. For further details, refer to Fig. 5.2 (p. 86) and to the discussion in the text.
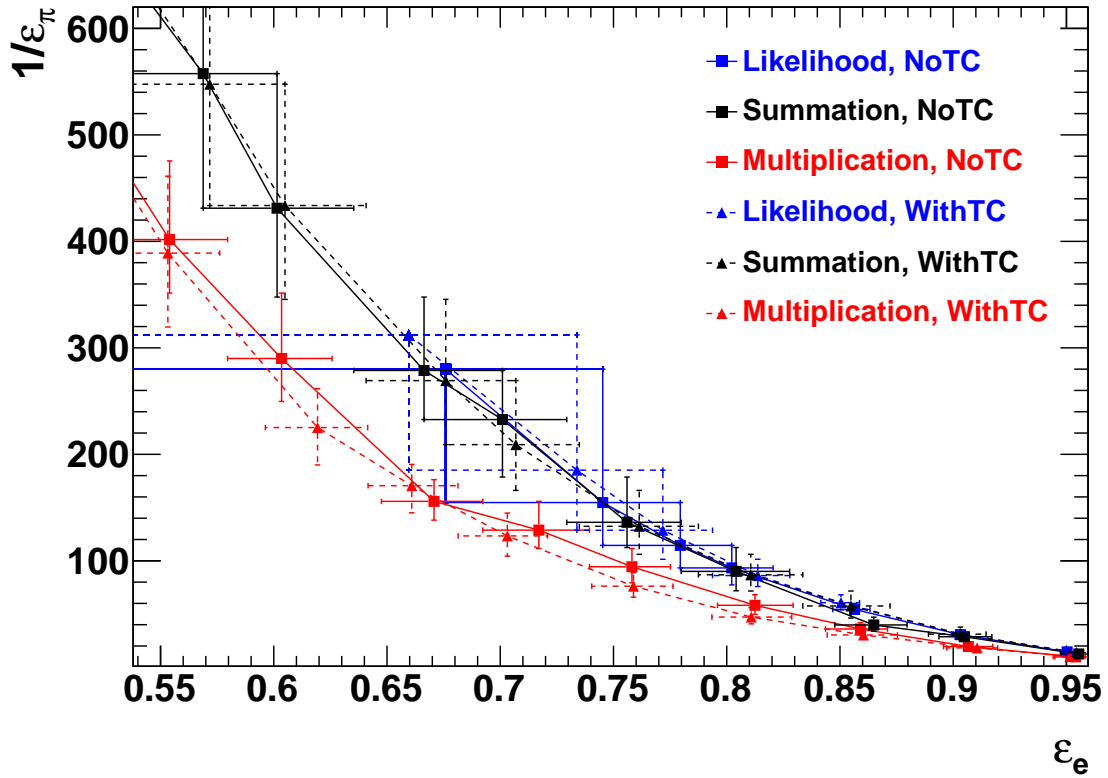
Figure D.4.: Pion suppression as a function of electron efficiency for the tracklets stage, 5 GeV/c, only pions, SW 2-26 and normal gas gain and drift velocity. The curves are just trend lines (no fits!) through the data points and are coloured differently for the different combination methods: likelihood (blue), summation (black), multiplication (red). Data for TC off is illustrated by solid lines and squares, data for TC on by broken lines and triangles. For further details, refer to Fig. 5.2 (p. 86) and to the discussion in the text.
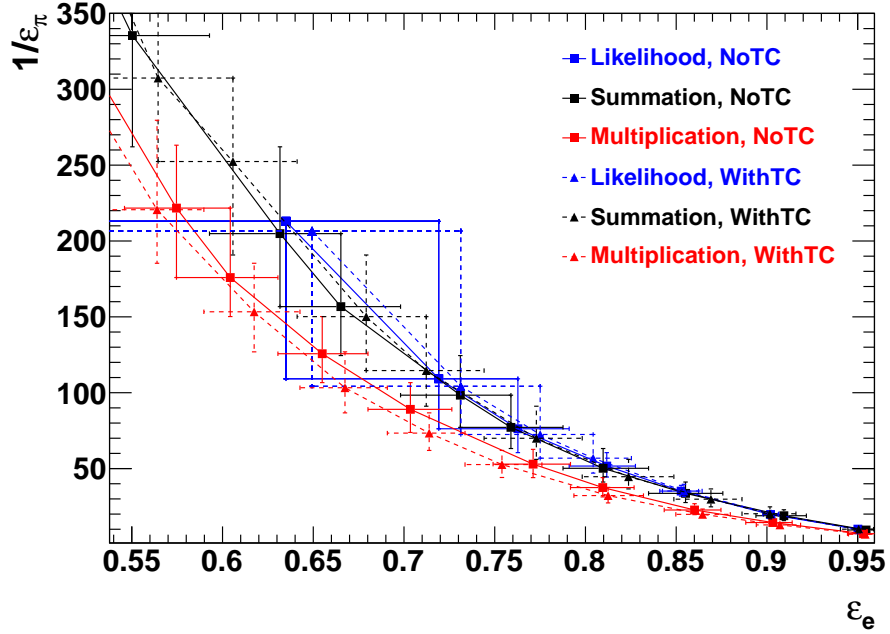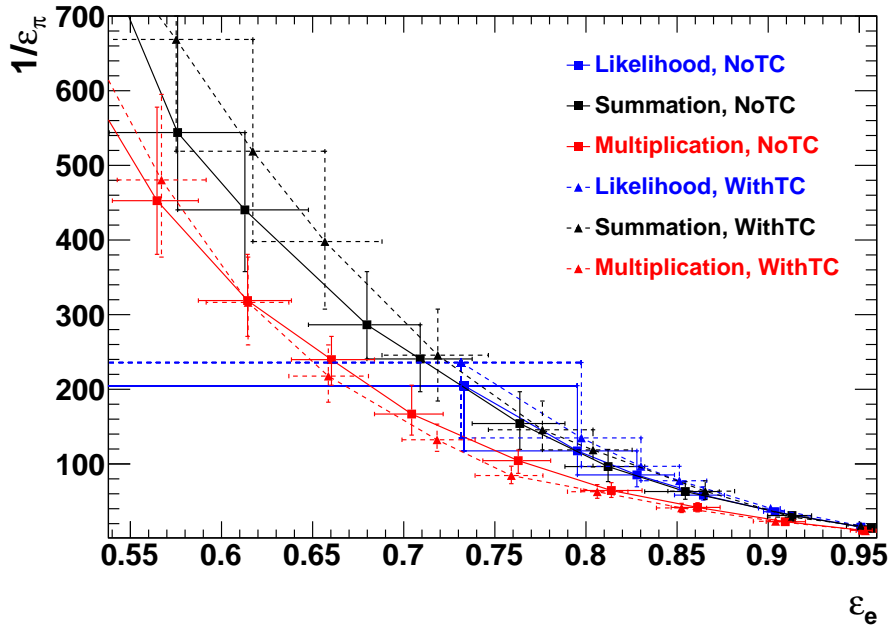
(a) SW 2-21

(b) SW 2-26

Figure D.5.: Pion suppression as a function of electron efficiency for the GTU tracks stage, 5 GeV/c, only pions, normal gas gain and drift velocity and **a)** SW 2-21 and **b)** SW 2-26. The curves are just trend lines (no fits!) through the data points and are coloured differently for the different combination methods: likelihood (blue), summation (black), multiplication (red). Data for TC off is illustrated by solid lines and squares, data for TC on by broken lines and triangles. For further details, refer to Fig. 5.2 (p. 86) and to the discussion in the text.

Settings		Drift velocity	Effective electron	Pion suppression
TC	SW	[cm/μs]	efficiency [%]	
Off	2-21	1.4	$87.1^{+1.4}_{-1.5}$	$11.5^{+1.9}_{-1.5}$
		1.5	$92.2^{+1.1}_{-1.2}$	$7.7^{+1.0}_{-0.9}$
		1.6	$94.95^{+0.72}_{-0.82}$	$5.76^{+0.73}_{-0.63}$
On	2-21	1.4	$87.7^{+1.3}_{-1.8}$	$10.7^{+1.7}_{-1.3}$
		1.5	$92.7^{+0.9}_{-1.1}$	$7.04^{+0.91}_{-0.77}$
		1.6	$94.52^{+0.66}_{-0.74}$	$5.70^{+0.66}_{-0.59}$
Off	2-26	1.4	$92.83^{+0.91}_{-0.86}$	$15.9^{+2.4}_{-2.2}$
		1.5	$92.9^{+0.9}_{-1.2}$	$14.6^{+2.3}_{-1.8}$
		1.6	$92.3^{+0.9}_{-1.0}$	$14.3^{+2.0}_{-1.9}$
On	2-26	1.4	$94.56^{+0.68}_{-0.79}$	$11.2^{+1.4}_{-1.2}$
		1.5	$92.93^{+0.76}_{-0.95}$	$13.8^{+1.8}_{-1.6}$
		1.6	$90.1^{+1.0}_{-1.0}$	$17.0^{+2.5}_{-2.1}$

Settings		Gas gain	Effective electron	Pion suppression
TC	SW	[arb. unit]	efficiency [%]	
Off	2-21	3600	$84.7^{+1.6}_{-1.8}$	$20.0^{+3.6}_{-3.0}$
		4000	$92.5^{+1.0}_{-1.1}$	$7.6^{+1.0}_{-1.0}$
		4200	$94.73^{+0.79}_{-0.81}$	$5.16^{+0.64}_{-0.54}$
		4400	$96.23^{+0.56}_{-0.61}$	$3.80^{+0.40}_{-0.35}$
On	2-21	3600	$85.0^{+1.6}_{-1.6}$	$18.0^{+3.0}_{-2.4}$
		4000	$92.0^{+1.0}_{-1.1}$	$7.08^{+0.93}_{-0.77}$
		4200	$94.22^{+0.72}_{-0.82}$	$4.95^{+0.54}_{-0.47}$
		4400	$95.62^{+0.64}_{-0.69}$	$3.71^{+0.35}_{-0.32}$
Off	2-26	3600	$85.4^{+1.6}_{-1.6}$	$48.3^{+8.3}_{-7.9}$
		4000	$93.12^{+0.86}_{-0.99}$	$14.6^{+2.5}_{-1.8}$
		4200	$95.09^{+0.68}_{-0.77}$	$9.3^{+1.3}_{-1.1}$
		4400	$96.55^{+0.46}_{-0.54}$	$6.15^{+0.78}_{-0.64}$
On	2-26	3600	$84.8^{+1.4}_{-1.6}$	$43.4^{+6.6}_{-5.9}$
		4000	$92.11^{+0.88}_{-0.92}$	$14.1^{+1.9}_{-1.6}$
		4200	$94.27^{+0.69}_{-0.76}$	$9.1^{+1.1}_{-1.0}$
		4400	$95.82^{+0.50}_{-0.60}$	$6.16^{+0.67}_{-0.55}$

Table D.13.: 5.0 GeV/c, tracklets, only pions, multiplication.

Settings		Drift velocity	Effective electron	Pion suppression
TC	SW	[cm/μs]	efficiency [%]	
Off	2-21	1.4	$87.8^{+1.5}_{-1.9}$	$14.0^{+2.6}_{-1.9}$
		1.5	$93.2^{+1.1}_{-1.2}$	$9.3^{+1.6}_{-1.2}$
		1.6	$95.67^{+0.71}_{-0.71}$	$6.9^{+1.0}_{-0.8}$
On	2-21	1.4	$86.6^{+1.8}_{-1.9}$	$14.9^{+2.8}_{-2.2}$
		1.5	$92.6^{+1.0}_{-1.2}$	$9.9^{+1.7}_{-1.3}$
		1.6	$94.66^{+0.77}_{-0.82}$	$7.7^{+1.2}_{-1.0}$
Off	2-26	1.4	$93.0^{+1.0}_{-1.1}$	$21.7^{+3.9}_{-3.3}$
		1.5	$92.8^{+1.1}_{-1.1}$	$20.3^{+3.6}_{-3.1}$
		1.6	$92.5^{+1.1}_{-1.2}$	$19.4^{+3.5}_{-3.0}$
On	2-26	1.4	$94.3^{+0.9}_{-1.1}$	$18.1^{+3.3}_{-2.8}$
		1.5	$92.7^{+1.2}_{-1.2}$	$22.0^{+3.9}_{-3.4}$
		1.6	$90.4^{+1.3}_{-1.4}$	$27.4^{+5.6}_{-3.9}$

Settings		Gas gain	Effective electron	Pion suppression
TC	SW	[arb. unit]	efficiency [%]	
Off	2-21	3600	$83.0^{+2.0}_{-2.2}$	$29.6^{+6.6}_{-5.0}$
		4000	$92.0^{+1.1}_{-1.4}$	$10.8^{+1.9}_{-1.6}$
		4200	$94.58^{+0.81}_{-0.98}$	$7.1^{+1.2}_{-0.9}$
		4400	$96.27^{+0.54}_{-0.64}$	$4.99^{+0.67}_{-0.54}$
On	2-21	3600	$84.3^{+1.8}_{-2.0}$	$25.8^{+5.2}_{-4.2}$
		4000	$92.0^{+1.1}_{-1.2}$	$10.2^{+1.6}_{-1.3}$
		4200	$94.44^{+0.85}_{-0.93}$	$6.58^{+1.00}_{-0.83}$
		4400	$96.02^{+0.58}_{-0.74}$	$4.71^{+0.59}_{-0.48}$
Off	2-26	3600	$84.7^{+1.7}_{-1.8}$	63^{+12}_{-11}
		4000	$93.0^{+0.9}_{-1.1}$	$20.3^{+3.9}_{-3.2}$
		4200	$95.21^{+0.72}_{-0.79}$	$12.5^{+2.0}_{-1.7}$
		4400	$96.72^{+0.50}_{-0.61}$	$8.1^{+1.2}_{-1.0}$
On	2-26	3600	$84.5^{+1.7}_{-1.9}$	69^{+13}_{-12}
		4000	$92.5^{+1.0}_{-1.1}$	$21.7^{+4.2}_{-3.0}$
		4200	$94.84^{+0.78}_{-0.86}$	$13.5^{+2.2}_{-1.8}$
		4400	$96.44^{+0.49}_{-0.66}$	$8.9^{+1.4}_{-1.1}$

Table D.14.: 5.0 GeV/c, tracklets, only pions, summation.

Settings		Drift velocity	Effective electron	Pion suppression
TC	SW	[cm/μs]	efficiency [%]	
Off	2-21	1.4	$86.18^{+0.32}_{-0.22}$	$15.83^{+0.38}_{-0.36}$
		1.5	$92.21^{+0.19}_{-0.22}$	$10.39^{+0.21}_{-0.23}$
		1.6	$95.09^{+0.11}_{-0.10}$	$7.58^{+0.16}_{-0.15}$
On	2-21	1.4	$86.25^{+0.23}_{-0.22}$	$15.24^{+0.36}_{-0.34}$
		1.5	$92.44^{+0.14}_{-0.14}$	$9.99^{+0.23}_{-0.19}$
		1.6	$94.52^{+0.12}_{-0.08}$	$7.78^{+0.14}_{-0.14}$
Off	2-26	1.4	$93.00^{+0.11}_{-0.09}$	$21.76^{+0.59}_{-0.71}$
		1.5	$92.79^{+0.19}_{-0.18}$	$20.34^{+0.68}_{-0.52}$
		1.6	$92.45^{+0.17}_{-0.22}$	$19.63^{+0.66}_{-0.53}$
On	2-26	1.4	$94.18^{+0.11}_{-0.14}$	$18.32^{+0.50}_{-0.51}$
		1.5	$92.57^{+0.19}_{-0.14}$	$22.33^{+0.73}_{-0.62}$
		1.6	$90.15^{+0.25}_{-0.23}$	$27.55^{+0.84}_{-0.92}$

Settings		Gas gain	Effective electron	Pion suppression
TC	SW	[arb. unit]	efficiency [%]	
Off	2-21	3600	$82.94^{+0.25}_{-0.28}$	$29.38^{+0.78}_{-0.98}$
		4000	$91.95^{+0.16}_{-0.15}$	$10.73^{+0.25}_{-0.24}$
		4200	$94.57^{+0.12}_{-0.12}$	$7.13^{+0.13}_{-0.16}$
		4400	$96.229^{+0.097}_{-0.089}$	$4.959^{+0.092}_{-0.082}$
On	2-21	3600	$84.20^{+0.27}_{-0.26}$	$25.72^{+0.63}_{-0.75}$
		4000	$92.00^{+0.17}_{-0.18}$	$9.77^{+0.18}_{-0.20}$
		4200	$94.41^{+0.12}_{-0.14}$	$6.55^{+0.12}_{-0.13}$
		4400	$95.966^{+0.080}_{-0.080}$	$4.711^{+0.074}_{-0.077}$
Off	2-26	3600	$84.89^{+0.28}_{-0.31}$	$62.1^{+2.2}_{-1.7}$
		4000	$93.08^{+0.16}_{-0.15}$	$19.95^{+0.57}_{-0.49}$
		4200	$95.26^{+0.10}_{-0.12}$	$12.36^{+0.29}_{-0.33}$
		4400	$96.735^{+0.092}_{-0.089}$	$8.12^{+0.19}_{-0.16}$
On	2-26	3600	$84.23^{+0.27}_{-0.29}$	$69.2^{+3.3}_{-2.5}$
		4000	$92.30^{+0.19}_{-0.18}$	$21.79^{+0.59}_{-0.56}$
		4200	$94.68^{+0.14}_{-0.16}$	$13.41^{+0.34}_{-0.30}$
		4400	$96.33^{+0.10}_{-0.10}$	$8.80^{+0.19}_{-0.21}$

Table D.15.: 5.0 GeV/c, tracklets, only pions, likelihood.

| Settings | | Drift velocity | Effective electron | Pion suppression |
TC	SW	[cm/μs]	efficiency [%]	
Off	2-21	1.4	$87.7^{+1.3}_{-1.4}$	$13.5^{+1.8}_{-1.6}$
		1.5	$92.4^{+1.1}_{-1.0}$	$9.1^{+1.1}_{-0.9}$
		1.6	$95.00^{+0.72}_{-0.72}$	$7.11^{+0.75}_{-0.66}$
On	2-21	1.4	$86.7^{+1.4}_{-1.3}$	$13.3^{+1.6}_{-1.5}$
		1.5	$91.9^{+1.0}_{-1.1}$	$9.1^{+1.0}_{-0.9}$
		1.6	$93.91^{+0.77}_{-0.67}$	$7.45^{+0.74}_{-0.67}$
Off	2-26	1.4	$93.50^{+0.88}_{-0.91}$	$17.0^{+2.4}_{-2.0}$
		1.5	$93.49^{+0.79}_{-0.93}$	$15.8^{+2.0}_{-1.8}$
		1.6	$92.76^{+0.83}_{-0.94}$	$15.9^{+2.0}_{-1.9}$
On	2-26	1.4	$94.23^{+0.60}_{-0.59}$	$13.9^{+1.5}_{-1.3}$
		1.5	$92.34^{+0.76}_{-0.90}$	$16.9^{+1.8}_{-1.6}$
		1.6	$89.3^{+1.0}_{-1.1}$	$21.1^{+2.5}_{-2.3}$

| Settings | | Gas gain | Effective electron | Pion suppression |
TC	SW	[arb. unit]	efficiency [%]	
Off	2-21	3600	$85.5^{+1.6}_{-1.5}$	$22.8^{+3.7}_{-3.1}$
		4000	$92.71^{+0.88}_{-0.92}$	$9.0^{+1.1}_{-1.0}$
		4200	$94.80^{+0.72}_{-0.81}$	$6.36^{+0.67}_{-0.59}$
		4400	$96.16^{+0.52}_{-0.52}$	$4.81^{+0.45}_{-0.41}$
On	2-21	3600	$85.7^{+1.4}_{-1.4}$	$18.5^{+2.4}_{-2.2}$
		4000	$92.28^{+0.90}_{-0.96}$	$8.03^{+0.85}_{-0.74}$
		4200	$94.35^{+0.69}_{-0.75}$	$5.89^{+0.53}_{-0.47}$
		4400	$95.70^{+0.56}_{-0.64}$	$4.56^{+0.37}_{-0.33}$
Off	2-26	3600	$86.9^{+1.3}_{-1.4}$	$49.1^{+7.9}_{-7.0}$
		4000	$93.71^{+0.78}_{-0.85}$	$16.1^{+2.2}_{-1.8}$
		4200	$95.46^{+0.58}_{-0.69}$	$10.4^{+1.2}_{-1.1}$
		4400	$96.74^{+0.44}_{-0.47}$	$7.22^{+0.75}_{-0.66}$
On	2-26	3600	$85.5^{+1.3}_{-1.5}$	$43.3^{+5.7}_{-5.3}$
		4000	$92.23^{+0.82}_{-0.89}$	$15.5^{+1.7}_{-1.5}$
		4200	$94.28^{+0.67}_{-0.72}$	$10.3^{+1.1}_{-1.0}$
		4400	$95.59^{+0.54}_{-0.54}$	$7.34^{+0.66}_{-0.61}$

Table D.16.: 5.0 GeV/c, tracklets, all, multiplication.

Settings		Drift velocity	Effective electron	Pion suppression
TC	SW	[cm/μs]	efficiency [%]	
Off	2-21	1.4	$87.7^{+1.6}_{-1.9}$	$19.0^{+3.5}_{-2.7}$
		1.5	$93.1^{+0.9}_{-1.2}$	$12.6^{+2.0}_{-1.7}$
		1.6	$95.48^{+0.69}_{-0.76}$	$9.5^{+1.3}_{-1.1}$
On	2-21	1.4	$86.4^{+1.8}_{-1.9}$	$19.6^{+3.7}_{-2.9}$
		1.5	$92.4^{+1.2}_{-1.2}$	$13.1^{+2.1}_{-1.8}$
		1.6	$94.52^{+0.65}_{-0.87}$	$10.4^{+1.6}_{-1.3}$
Off	2-26	1.4	$92.95^{+0.97}_{-0.99}$	$29.6^{+5.4}_{-4.6}$
		1.5	$92.8^{+0.9}_{-1.1}$	$26.7^{+4.7}_{-3.9}$
		1.6	$92.4^{+1.1}_{-1.1}$	$26.0^{+4.5}_{-3.8}$
On	2-26	1.4	$94.50^{+0.82}_{-0.88}$	$22.6^{+4.1}_{-3.3}$
		1.5	$92.9^{+1.1}_{-1.2}$	$27.7^{+4.7}_{-4.0}$
		1.6	$90.6^{+1.1}_{-1.3}$	$35.0^{+6.4}_{-5.2}$

Settings		Gas gain	Effective electron	Pion suppression
TC	SW	[arb. unit]	efficiency [%]	
Off	2-21	3600	$84.9^{+1.7}_{-1.9}$	$33.7^{+6.8}_{-5.3}$
		4000	$92.9^{+1.0}_{-1.1}$	$12.7^{+1.9}_{-1.6}$
		4200	$95.16^{+0.66}_{-0.81}$	$8.5^{+1.2}_{-1.0}$
		4400	$96.58^{+0.50}_{-0.56}$	$6.14^{+0.74}_{-0.64}$
On	2-21	3600	$84.3^{+1.8}_{-1.9}$	$32.3^{+6.3}_{-5.2}$
		4000	$91.9^{+1.1}_{-1.2}$	$12.6^{+2.0}_{-1.7}$
		4200	$94.35^{+0.78}_{-0.92}$	$8.6^{+1.2}_{-1.0}$
		4400	$95.85^{+0.65}_{-0.67}$	$6.28^{+0.76}_{-0.67}$
Off	2-26	3600	$84.8^{+1.7}_{-1.8}$	85^{+18}_{-14}
		4000	$92.9^{+0.9}_{-1.0}$	$27.2^{+4.8}_{-4.2}$
		4200	$95.06^{+0.73}_{-0.72}$	$16.8^{+2.6}_{-2.2}$
		4400	$96.58^{+0.51}_{-0.58}$	$11.1^{+1.6}_{-1.3}$
On	2-26	3600	$85.1^{+1.7}_{-1.9}$	80^{+17}_{-14}
		4000	$92.6^{+1.0}_{-1.2}$	$26.8^{+4.8}_{-4.0}$
		4200	$94.90^{+0.75}_{-0.92}$	$17.0^{+2.8}_{-2.3}$
		4400	$96.36^{+0.57}_{-0.64}$	$11.4^{+1.7}_{-1.4}$

Table D.17.: 5.0 GeV/c, tracklets, all, summation.

Settings		Drift velocity	Effective electron	Pion suppression
TC	SW	[cm/μs]	efficiency [%]	
Off	2-21	1.4	$86.39^{+0.32}_{-0.28}$	$20.87^{+0.47}_{-0.52}$
		1.5	$92.30^{+0.14}_{-0.20}$	$13.51^{+0.29}_{-0.27}$
		1.6	$94.99^{+0.12}_{-0.11}$	$10.14^{+0.21}_{-0.21}$
On	2-21	1.4	$86.55^{+0.28}_{-0.33}$	$19.17^{+0.49}_{-0.44}$
		1.5	$92.41^{+0.19}_{-0.24}$	$12.62^{+0.30}_{-0.27}$
		1.6	$94.43^{+0.17}_{-0.14}$	$10.07^{+0.20}_{-0.19}$
Off	2-26	1.4	$93.07^{+0.17}_{-0.16}$	$28.71^{+0.93}_{-0.87}$
		1.5	$93.01^{+0.17}_{-0.28}$	$26.01^{+0.84}_{-0.81}$
		1.6	$92.42^{+0.23}_{-0.21}$	$25.67^{+0.79}_{-0.84}$
On	2-26	1.4	$94.23^{+0.29}_{-0.25}$	$24.0^{+1.2}_{-1.1}$
		1.5	$92.60^{+0.36}_{-0.30}$	$28.9^{+1.4}_{-1.2}$
		1.6	$90.00^{+0.34}_{-0.37}$	$36.7^{+1.9}_{-1.7}$

Settings		Gas gain	Effective electron	Pion suppression
TC	SW	[arb. unit]	efficiency [%]	
Off	2-21	3600	$83.52^{+0.30}_{-0.25}$	$37.62^{+0.95}_{-0.90}$
		4000	$92.07^{+0.17}_{-0.23}$	$13.84^{+0.30}_{-0.29}$
		4200	$94.49^{+0.12}_{-0.12}$	$9.22^{+0.19}_{-0.18}$
		4400	$96.09^{+0.11}_{-0.08}$	$6.60^{+0.11}_{-0.11}$
On	2-21	3600	$84.24^{+0.24}_{-0.24}$	$31.26^{+0.85}_{-0.80}$
		4000	$91.87^{+0.14}_{-0.18}$	$12.25^{+0.25}_{-0.24}$
		4200	$94.17^{+0.12}_{-0.11}$	$8.43^{+0.16}_{-0.15}$
		4400	$95.77^{+0.12}_{-0.10}$	$6.18^{+0.10}_{-0.10}$
Off	2-26	3600	$85.49^{+0.33}_{-0.33}$	$80.4^{+3.0}_{-2.8}$
		4000	$93.31^{+0.18}_{-0.21}$	$25.42^{+0.91}_{-0.74}$
		4200	$95.36^{+0.11}_{-0.16}$	$15.85^{+0.44}_{-0.42}$
		4400	$96.77^{+0.09}_{-0.10}$	$10.48^{+0.28}_{-0.24}$
On	2-26	3600	$84.38^{+0.30}_{-0.37}$	$82.7^{+3.6}_{-2.9}$
		4000	$92.06^{+0.20}_{-0.21}$	$26.99^{+0.86}_{-0.70}$
		4200	$94.40^{+0.13}_{-0.18}$	$17.00^{+0.47}_{-0.46}$
		4400	$95.93^{+0.11}_{-0.11}$	$11.40^{+0.28}_{-0.28}$

Table D.18.: 5.0 GeV/c, tracklets, all, likelihood.

Settings		Drift velocity	Effective electron	Pion suppression
TC	SW	[cm/μs]	efficiency [%]	
Off	2-21	1.4	$87.7^{+1.3}_{-1.7}$	$17.8^{+2.8}_{-2.4}$
		1.5	$92.5^{+1.0}_{-1.1}$	$10.7^{+1.6}_{-1.5}$
		1.6	$95.27^{+0.61}_{-0.74}$	$7.3^{+1.0}_{-0.9}$
On	2-21	1.4	$87.2^{+1.4}_{-1.6}$	$16.1^{+2.6}_{-2.0}$
		1.5	$92.85^{+0.97}_{-0.99}$	$9.8^{+1.5}_{-1.2}$
		1.6	$95.02^{+0.58}_{-0.76}$	$7.25^{+0.99}_{-0.80}$
Off	2-26	1.4	$92.80^{+0.76}_{-0.99}$	$19.1^{+2.9}_{-2.6}$
		1.5	$92.86^{+0.81}_{-0.81}$	$16.8^{+2.7}_{-2.3}$
		1.6	$92.94^{+0.87}_{-0.85}$	$15.4^{+2.3}_{-2.1}$
On	2-26	1.4	$94.37^{+0.73}_{-0.87}$	$12.8^{+1.7}_{-1.5}$
		1.5	$93.27^{+0.80}_{-0.89}$	$15.2^{+2.2}_{-1.9}$
		1.6	$91.8^{+0.9}_{-1.1}$	$18.1^{+2.7}_{-2.1}$

Settings		Gas gain	Effective electron	Pion suppression
TC	SW	[arb. unit]	efficiency [%]	
Off	2-21	3600	$84.6^{+1.7}_{-1.9}$	$33.0^{+6.3}_{-5.4}$
		4000	$92.8^{+1.0}_{-1.1}$	$10.6^{+1.6}_{-1.4}$
		4200	$94.96^{+0.71}_{-0.79}$	$6.75^{+0.88}_{-0.78}$
		4400	$96.48^{+0.46}_{-0.55}$	$4.57^{+0.56}_{-0.47}$
On	2-21	3600	$85.0^{+1.5}_{-1.7}$	$27.6^{+5.2}_{-3.8}$
		4000	$92.6^{+0.9}_{-1.0}$	$9.8^{+1.3}_{-1.2}$
		4200	$94.53^{+0.70}_{-0.82}$	$6.37^{+0.78}_{-0.72}$
		4400	$95.95^{+0.54}_{-0.59}$	$4.43^{+0.46}_{-0.43}$
Off	2-26	3600	$85.6^{+1.4}_{-1.6}$	57^{+10}_{-9}
		4000	$92.87^{+0.81}_{-0.86}$	$16.7^{+2.5}_{-2.3}$
		4200	$94.74^{+0.67}_{-0.70}$	$9.8^{+1.3}_{-1.2}$
		4400	$96.19^{+0.48}_{-0.50}$	$6.40^{+0.77}_{-0.67}$
On	2-26	3600	$85.9^{+1.3}_{-1.4}$	$49.2^{+6.9}_{-7.5}$
		4000	$93.00^{+0.80}_{-0.87}$	$15.1^{+2.0}_{-1.9}$
		4200	$94.77^{+0.65}_{-0.70}$	$9.4^{+1.2}_{-1.0}$
		4400	$96.23^{+0.48}_{-0.52}$	$6.13^{+0.67}_{-0.58}$

Table D.19.: 5.0 GeV/c, GTU tracks, only pions, multiplication.

Settings		Drift velocity	Effective electron	Pion suppression
TC	SW	[cm/μs]	efficiency [%]	
Off	2-21	1.4	$85.9^{+1.8}_{-2.1}$	$25.8^{+5.3}_{-4.1}$
		1.5	$92.2^{+1.2}_{-1.2}$	$15.7^{+3.2}_{-2.4}$
		1.6	$95.34^{+0.71}_{-0.95}$	$10.4^{+1.9}_{-1.5}$
On	2-21	1.4	$86.6^{+1.8}_{-1.8}$	$23.1^{+5.0}_{-3.7}$
		1.5	$93.0^{+1.0}_{-1.4}$	$14.2^{+2.6}_{-2.3}$
		1.6	$95.5^{+0.8}_{-1.0}$	$10.2^{+1.9}_{-1.5}$
Off	2-26	1.4	$92.85^{+0.96}_{-0.85}$	$25.0^{+5.3}_{-4.2}$
		1.5	$93.24^{+0.90}_{-0.86}$	$22.1^{+4.0}_{-3.5}$
		1.6	$93.43^{+0.82}_{-0.92}$	$20.1^{+3.7}_{-3.1}$
On	2-26	1.4	$94.31^{+0.85}_{-0.95}$	$20.2^{+4.2}_{-3.2}$
		1.5	$93.34^{+0.95}_{-0.98}$	$24.0^{+4.8}_{-3.8}$
		1.6	$92.1^{+1.0}_{-1.2}$	$29.1^{+5.9}_{-4.6}$

Settings		Gas gain	Effective electron	Pion suppression
TC	SW	[arb. unit]	efficiency [%]	
Off	2-21	3600	$82.5^{+2.1}_{-2.3}$	48^{+11}_{-9}
		4000	$92.4^{+1.2}_{-1.2}$	$15.7^{+3.1}_{-2.6}$
		4200	$94.78^{+0.85}_{-0.86}$	$9.5^{+1.5}_{-1.3}$
		4400	$96.58^{+0.49}_{-0.63}$	$6.24^{+0.99}_{-0.77}$
On	2-21	3600	$84.2^{+1.9}_{-2.2}$	$41.5^{+8.7}_{-7.8}$
		4000	$92.7^{+1.1}_{-1.3}$	$14.0^{+2.7}_{-2.1}$
		4200	$94.91^{+0.79}_{-0.94}$	$8.8^{+1.5}_{-1.2}$
		4400	$96.47^{+0.59}_{-0.72}$	$5.88^{+0.92}_{-0.77}$
Off	2-26	3600	$85.3^{+1.6}_{-1.8}$	69^{+16}_{-13}
		4000	$93.3^{+0.9}_{-1.0}$	$21.9^{+4.4}_{-3.4}$
		4200	$95.30^{+0.62}_{-0.69}$	$12.7^{+2.2}_{-1.8}$
		4400	$96.64^{+0.45}_{-0.53}$	$8.2^{+1.3}_{-1.0}$
On	2-26	3600	$85.3^{+1.6}_{-1.9}$	77^{+16}_{-15}
		4000	$93.2^{+0.9}_{-1.1}$	$24.5^{+5.3}_{-4.2}$
		4200	$95.28^{+0.67}_{-0.85}$	$14.3^{+2.6}_{-2.2}$
		4400	$96.71^{+0.54}_{-0.62}$	$9.1^{+1.5}_{-1.2}$

Table D.20.: 5.0 GeV/c, GTU tracks, only pions, summation.

Settings		Drift velocity	Effective electron	Pion suppression
TC	SW	[cm/μs]	efficiency [%]	
Off	2-21	1.4	$86.33^{+0.37}_{-0.32}$	$24.7^{+1.1}_{-1.1}$
		1.5	$92.38^{+0.27}_{-0.26}$	$15.09^{+0.57}_{-0.46}$
		1.6	$95.22^{+0.20}_{-0.21}$	$10.02^{+0.34}_{-0.35}$
On	2-21	1.4	$86.06^{+0.42}_{-0.42}$	$24.4^{+0.9}_{-1.1}$
		1.5	$92.52^{+0.32}_{-0.29}$	$14.74^{+0.67}_{-0.55}$
		1.6	$94.99^{+0.23}_{-0.17}$	$10.55^{+0.35}_{-0.35}$
Off	2-26	1.4	$92.72^{+0.23}_{-0.26}$	$26.5^{+1.2}_{-1.1}$
		1.5	$93.00^{+0.13}_{-0.23}$	$23.3^{+1.1}_{-0.9}$
		1.6	$92.95^{+0.20}_{-0.18}$	$21.3^{+1.1}_{-0.8}$
On	2-26	1.4	$94.01^{+0.18}_{-0.16}$	$21.4^{+1.1}_{-0.9}$
		1.5	$93.01^{+0.27}_{-0.31}$	$25.5^{+1.2}_{-1.2}$
		1.6	$91.62^{+0.30}_{-0.27}$	$30.6^{+1.6}_{-1.4}$

Settings		Gas gain	Effective electron	Pion suppression
TC	SW	[arb. unit]	efficiency [%]	
Off	2-21	3600	$82.94^{+0.44}_{-0.47}$	$45.8^{+1.9}_{-1.5}$
		4000	$92.50^{+0.22}_{-0.26}$	$15.00^{+0.55}_{-0.53}$
		4200	$94.84^{+0.18}_{-0.19}$	$9.14^{+0.34}_{-0.29}$
		4400	$96.52^{+0.12}_{-0.11}$	$6.09^{+0.18}_{-0.17}$
On	2-21	3600	$83.65^{+0.42}_{-0.48}$	$44.7^{+2.1}_{-1.9}$
		4000	$92.31^{+0.26}_{-0.25}$	$14.54^{+0.56}_{-0.61}$
		4200	$94.51^{+0.21}_{-0.22}$	$9.10^{+0.35}_{-0.27}$
		4400	$96.13^{+0.15}_{-0.14}$	$6.06^{+0.20}_{-0.19}$
Off	2-26	3600	$84.81^{+0.41}_{-0.47}$	$76.5^{+3.5}_{-4.4}$
		4000	$92.94^{+0.20}_{-0.25}$	$23.0^{+1.1}_{-1.1}$
		4200	$94.99^{+0.15}_{-0.16}$	$13.36^{+0.51}_{-0.53}$
		4400	$96.36^{+0.12}_{-0.15}$	$8.60^{+0.30}_{-0.28}$
On	2-26	3600	$85.18^{+0.40}_{-0.42}$	$79.4^{+4.7}_{-3.4}$
		4000	$93.13^{+0.23}_{-0.23}$	$24.4^{+1.3}_{-1.0}$
		4200	$95.07^{+0.18}_{-0.17}$	$14.32^{+0.60}_{-0.53}$
		4400	$96.57^{+0.13}_{-0.15}$	$9.07^{+0.32}_{-0.27}$

Table D.21.: 5.0 GeV/c, GTU tracks, only pions, likelihood.

Settings		Drift velocity	Effective electron	Pion suppression
TC	SW	[cm/μs]	efficiency [%]	
Off	2-21	1.4	$87.8^{+1.3}_{-1.5}$	$20.6^{+3.2}_{-2.7}$
		1.5	$92.2^{+1.0}_{-1.0}$	$13.1^{+1.7}_{-1.5}$
		1.6	$94.88^{+0.60}_{-0.76}$	$9.1^{+1.1}_{-1.0}$
On	2-21	1.4	$87.1^{+1.3}_{-1.8}$	$17.9^{+2.4}_{-2.1}$
		1.5	$92.3^{+1.1}_{-0.9}$	$11.5^{+1.4}_{-1.2}$
		1.6	$94.57^{+0.65}_{-0.77}$	$8.74^{+0.98}_{-0.85}$
Off	2-26	1.4	$92.78^{+0.79}_{-0.89}$	$21.7^{+3.1}_{-2.7}$
		1.5	$92.88^{+0.73}_{-0.90}$	$19.5^{+2.8}_{-2.3}$
		1.6	$92.88^{+0.71}_{-0.84}$	$18.0^{+2.5}_{-2.1}$
On	2-26	1.4	$94.14^{+0.62}_{-0.80}$	$14.8^{+1.7}_{-1.4}$
		1.5	$92.69^{+0.84}_{-0.75}$	$17.5^{+2.0}_{-1.7}$
		1.6	$91.2^{+0.8}_{-1.0}$	$22.5^{+2.8}_{-2.4}$

Settings		Gas gain	Effective electron	Pion suppression
TC	SW	[arb. unit]	efficiency [%]	
Off	2-21	3600	$84.9^{+1.5}_{-1.7}$	$38.7^{+6.5}_{-5.6}$
		4000	$92.56^{+0.89}_{-0.96}$	$12.5^{+1.6}_{-1.5}$
		4200	$94.58^{+0.71}_{-0.76}$	$8.52^{+0.99}_{-0.88}$
		4400	$96.04^{+0.50}_{-0.53}$	$5.90^{+0.58}_{-0.54}$
On	2-21	3600	$85.0^{+1.6}_{-1.5}$	$31.0^{+4.5}_{-4.1}$
		4000	$92.29^{+0.93}_{-0.93}$	$11.5^{+1.3}_{-1.2}$
		4200	$94.23^{+0.68}_{-0.78}$	$7.82^{+0.80}_{-0.72}$
		4400	$95.67^{+0.55}_{-0.57}$	$5.70^{+0.53}_{-0.46}$
Off	2-26	3600	$86.0^{+1.3}_{-1.3}$	63^{+10}_{-9}
		4000	$92.89^{+0.78}_{-0.81}$	$19.5^{+2.6}_{-2.4}$
		4200	$94.58^{+0.60}_{-0.62}$	$11.8^{+1.4}_{-1.3}$
		4400	$96.03^{+0.44}_{-0.52}$	$7.88^{+0.86}_{-0.76}$
On	2-26	3600	$85.5^{+1.2}_{-1.3}$	$52.4^{+7.5}_{-6.5}$
		4000	$92.63^{+0.79}_{-0.87}$	$17.6^{+2.0}_{-1.9}$
		4200	$94.41^{+0.59}_{-0.66}$	$10.8^{+1.2}_{-1.0}$
		4400	$96.01^{+0.45}_{-0.54}$	$7.81^{+0.71}_{-0.65}$

Table D.22.: 5.0 GeV/c, GTU tracks, all, multiplication.

Settings		Drift velocity	Effective electron	Pion suppression
TC	SW	[cm/μs]	efficiency [%]	
Off	2-21	1.4	$86.3^{+1.8}_{-1.8}$	$32.8^{+6.4}_{-5.3}$
		1.5	$92.2^{+1.1}_{-1.2}$	$20.3^{+3.8}_{-3.1}$
		1.6	$95.27^{+0.70}_{-0.90}$	$13.6^{+2.4}_{-1.9}$
On	2-21	1.4	$86.5^{+1.8}_{-1.7}$	$29.4^{+5.9}_{-4.7}$
		1.5	$92.8^{+1.2}_{-1.3}$	$18.3^{+3.4}_{-2.8}$
		1.6	$95.23^{+0.93}_{-0.95}$	$13.4^{+2.5}_{-1.9}$
Off	2-26	1.4	$93.0^{+0.9}_{-1.0}$	$32.4^{+6.1}_{-4.7}$
		1.5	$93.26^{+0.89}_{-0.95}$	$28.9^{+5.0}_{-4.4}$
		1.6	$93.38^{+0.89}_{-0.87}$	$26.4^{+4.7}_{-3.9}$
On	2-26	1.4	$94.63^{+0.83}_{-0.85}$	$24.8^{+4.5}_{-3.7}$
		1.5	$93.62^{+0.92}_{-0.93}$	$29.3^{+5.4}_{-4.4}$
		1.6	$92.3^{+1.0}_{-1.1}$	$38.2^{+7.1}_{-6.0}$

| Settings		Gas gain	Effective electron	Pion suppression
TC	SW	[arb. unit]	efficiency [%]	
Off	2-21	3600	$83.1^{+2.0}_{-2.1}$	64^{+14}_{-11}
		4000	$92.5^{+1.1}_{-1.3}$	$19.5^{+3.6}_{-2.9}$
		4200	$94.75^{+0.80}_{-0.88}$	$12.6^{+2.1}_{-1.6}$
		4400	$96.45^{+0.51}_{-0.65}$	$8.3^{+1.2}_{-1.0}$
On	2-21	3600	$84.2^{+1.9}_{-2.2}$	54^{+12}_{-10}
		4000	$92.6^{+1.1}_{-1.3}$	$18.2^{+3.4}_{-2.7}$
		4200	$94.72^{+0.83}_{-0.91}$	$11.8^{+2.0}_{-1.6}$
		4400	$96.32^{+0.62}_{-0.71}$	$8.1^{+1.2}_{-1.0}$
Off	2-26	3600	$85.6^{+1.7}_{-1.7}$	92^{+21}_{-15}
		4000	$93.31^{+0.86}_{-0.97}$	$28.7^{+5.4}_{-4.1}$
		4200	$95.24^{+0.60}_{-0.71}$	$16.9^{+2.8}_{-2.3}$
		4400	$96.57^{+0.47}_{-0.57}$	$11.0^{+1.6}_{-1.4}$
On	2-26	3600	$85.8^{+1.7}_{-1.8}$	91^{+20}_{-15}
		4000	$93.5^{+0.9}_{-1.0}$	$29.4^{+5.7}_{-4.4}$
		4200	$95.47^{+0.66}_{-0.82}$	$17.2^{+2.9}_{-2.4}$
		4400	$96.90^{+0.50}_{-0.61}$	$11.7^{+1.8}_{-1.5}$

Table D.23.: 5.0 GeV/*c*, GTU tracks, all, summation.

| Settings | | Drift velocity | Effective electron | Pion suppression |
TC	SW	[cm/μs]	efficiency [%]	
Off	2-21	1.4	$86.50^{+0.51}_{-0.56}$	$31.7^{+1.7}_{-1.4}$
		1.5	$92.12^{+0.32}_{-0.38}$	$19.7^{+1.1}_{-0.9}$
		1.6	$94.96^{+0.24}_{-0.28}$	$13.37^{+0.62}_{-0.57}$
On	2-21	1.4	$85.85^{+0.54}_{-0.56}$	$31.3^{+1.7}_{-1.7}$
		1.5	$92.13^{+0.50}_{-0.39}$	$19.00^{+0.99}_{-0.92}$
		1.6	$94.76^{+0.21}_{-0.24}$	$13.88^{+0.73}_{-0.58}$
Off	2-26	1.4	$92.90^{+0.21}_{-0.31}$	$33.4^{+1.9}_{-1.7}$
		1.5	$92.97^{+0.30}_{-0.27}$	$29.80^{+1.8}_{-1.6}$
		1.6	$92.96^{+0.26}_{-0.32}$	$27.3^{+1.6}_{-1.4}$
On	2-26	1.4	$93.97^{+0.53}_{-0.41}$	$28.1^{+2.8}_{-2.2}$
		1.5	$93.02^{+0.57}_{-0.62}$	$32.6^{+3.5}_{-2.6}$
		1.6	$91.50^{+0.60}_{-0.66}$	$42.6^{+4.5}_{-3.5}$

| Settings | | Gas gain | Effective electron | Pion suppression |
TC	SW	[arb. unit]	efficiency [%]	
Off	2-21	3600	$83.18^{+0.59}_{-0.65}$	$62.6^{+4.1}_{-3.5}$
		4000	$92.34^{+0.30}_{-0.36}$	$18.86^{+0.93}_{-0.83}$
		4200	$94.56^{+0.24}_{-0.27}$	$12.29^{+0.57}_{-0.51}$
		4400	$96.21^{+0.17}_{-0.20}$	$8.11^{+0.35}_{-0.31}$
On	2-21	3600	$84.09^{+0.50}_{-0.62}$	$54.9^{+3.7}_{-2.8}$
		4000	$92.44^{+0.30}_{-0.33}$	$18.10^{+0.88}_{-0.79}$
		4200	$94.52^{+0.21}_{-0.24}$	$11.64^{+0.52}_{-0.46}$
		4400	$96.08^{+0.17}_{-0.19}$	$7.99^{+0.30}_{-0.28}$
Off	2-26	3600	$85.27^{+0.49}_{-0.60}$	$97.4^{+6.4}_{-5.5}$
		4000	$92.95^{+0.30}_{-0.31}$	$29.5^{+1.8}_{-1.5}$
		4200	$94.87^{+0.21}_{-0.22}$	$17.18^{+0.95}_{-0.75}$
		4400	$96.23^{+0.18}_{-0.22}$	$11.13^{+0.54}_{-0.47}$
On	2-26	3600	$85.61^{+0.68}_{-0.77}$	98^{+10}_{-8}
		4000	$93.39^{+0.33}_{-0.47}$	$30.2^{+2.5}_{-2.1}$
		4200	$95.24^{+0.27}_{-0.32}$	$17.5^{+1.3}_{-1.0}$
		4400	$96.71^{+0.24}_{-0.28}$	$11.93^{+0.83}_{-0.69}$

Table D.24.: 5.0 GeV/c, GTU tracks, all, likelihood.

D.3. Trends for the GTU Tracks Stage

This section summarises the trends for the GTU tracks stage, that are discussed in section 5.11. The most important point is that the trends and relative changes for the GTU tracks stage coincide with those of the tracklets stage within the errors in most cases. The error estimation for Tabs. D.25-D.28 is commented in section 5.4.
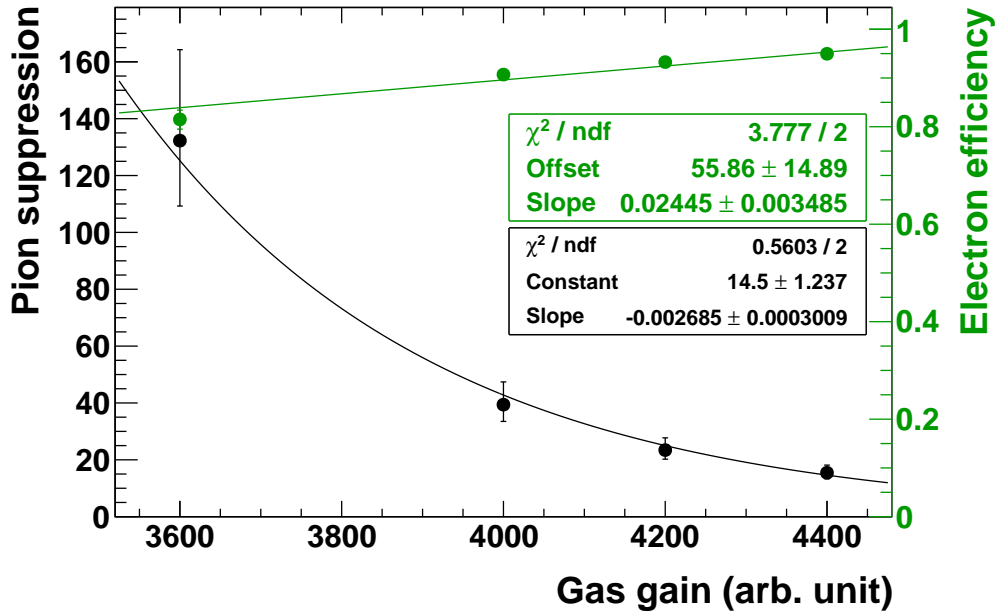
Figure D.6.: Impact of the gas gain on the PID. The data points are for the GTU tracks stage, 3 GeV/c, only pions, no TC, SW 2-26. The used combination method is "summation" as currently used by the GTU. The figure shows the dependence of the electron efficiency (green, right axis) and the pion suppression (black, left axis) on the gas gain. The shown curves are fit results. Obviously, in the considered gas gain region, the electron efficiency exhibits a linear behaviour, whereas the pion suppression is described reasonably well by an exponential function.

Relative change of gas gain [%]	Relative change of electron efficiency [%]		Relative change of pion suppression [%]	
	SW 2-21	SW 2-26	SW 2-21	SW 2-26
-10%	-11.93 ± 0.62	-10.54 ± 0.66	$+239 \pm 20$	$+236 \pm 20$
$+5\%$	$+3.39 \pm 0.24$	$+2.89 \pm 0.46$	-37.6 ± 3.5	-42.6 ± 3.4
$+10\%$	$+5.44 \pm 0.45$	$+4.75 \pm 0.43$	-60.3 ± 2.3	-63.5 ± 2.2

Table D.25.: Relative changes of electron efficiency and pion suppression with gas gain for 3.0 GeV/c particles, GTU tracks stage, only pions, no tail cancellation, likelihood method. Gas gain 4000 is the reference gas gain. Taking into account the errors, the results of all three combination methods (other methods not shown) are consistent.

TC	Change of drift velocity [cm/μs]	Relative change of electron efficiency [%]	
		SW 2-21	SW 2-26
Off	-0.1	-7.61 ± 0.67	-0.71 ± 0.53
	$+0.1$	$+4.02 \pm 0.48$	$+0.58 \pm 0.51$
On	-0.1	-7.64 ± 0.63	$+1.36 \pm 0.48$
	$+0.1$	$+3.09 \pm 0.46$	-1.92 ± 0.54
TC	Change of drift velocity [cm/μs]	Relative change of pion suppression [%]	
		SW 2-21	SW 2-26
Off	-0.1	$+66 \pm 11$	$+16.1 \pm 8.4$
	$+0.1$	-31.6 ± 4.1	-6.9 ± 6.6
On	-0.1	$+65 \pm 11$	-15.7 ± 5.6
	$+0.1$	-26.3 ± 4.3	$+19.3 \pm 7.4$

Table D.26.: Relative changes of electron efficiency and pion suppression with drift velocity for 3.0 GeV/c particles, GTU tracks stage, only pions, likelihood method. The reference drift velocity is 1.5 cm/μs. Taking into account the errors, the results of all three combination methods (other methods not shown) are consistent.

Gas gain	Relative change of pion suppression [%]	
[arb. unit]	SW 2-21	SW 2-26
3600	-6.2 ± 5.7	$+0.4 \pm 8.7$
4000	-1.1 ± 5.8	$+8.4 \pm 6.3$
4200	$+0.9 \pm 4.9$	$+9.9 \pm 6.8$
4400	$+1.3 \pm 5.1$	$+10.1 \pm 6.6$
Drift velocity	Relative change of pion suppression [%]	
[cm/μs]	SW 2-21	SW 2-26
1.4	-3.7 ± 6.7	-20.4 ± 5.6
1.5	-2.9 ± 5.8	$+9.7 \pm 7.5$
1.6	$+4.7 \pm 6.2$	$+40.5 \pm 9.0$

Table D.27.: Relative changes of pion suppression for TC on compared to TC off for 3.0 GeV/c particles, GTU tracks stage, only pions, likelihood method. Taking into account the errors, the results of all three combination methods (other methods not shown) are consistent. Note that the electron efficiency is, in general, different for TC on and TC off.

Settings		Pion suppression		Relative change of
TC	SW	only pions	all	pion suppression *only pions → all* [%]
Off	2-21	$27.5^{+1.2}_{-1.0}$	$35.2^{+2.0}_{-1.8}$	$+28.0 \pm 9.2$
On		$26.7^{+1.1}_{-1.1}$	$35.1^{+2.2}_{-1.8}$	$+31.5 \pm 9.9$
Off	2-26	$43.5^{+2.3}_{-1.5}$	$54.1^{+3.4}_{-2.8}$	$+24 \pm 10$
On		$47.7^{+2.1}_{-2.1}$	$60.5^{+6.5}_{-5.0}$	$+27 \pm 15$

Table D.28.: Impact of other particle species on the PID performance demonstrated for 3.0 GeV/c particles, drift velocity 1.5 cm/μs, nominal gas gain, GTU tracks stage, likelihood method. *Only pions* means that only electrons and pions are taken into account, whereas in case of *all*, also muons, protons and kaons (with 1:1:1:1 relative abundance) are considered. By design, the electron efficiencies are consistent with 90% for all cases and not shown for this reason. In the right column, the relative change of the pion suppression from *only pions* to *all* is stated.

Note that "pion suppression" is used as a synonym for "non-electron suppression" in case of *all*, since it is the commonly used phrase.

Appendix E.

List of Acronyms

A collection of some important acronyms:

2D LQ	Two-dimensional likelihood on deposited charge in two chamber sectors
ACORDE	ALICE Cosmic Ray Detector
ADC	Analogue to Digital Converter
ALICE	A Large Ion Collider Experiment
CTP	Central Trigger Processor
DAQ	Data Acquisition
DCS	Detector Control System
DDL	Detector Data Link
EMCal	Electromagnetic Calorimeter
ESD	Event Summary Data
FMD	Forward Multiplicity Detector
FSM	Finite State Machine
GTU	Global Tracking Unit
HLT	High-Level Trigger
HMPID	High Momentum Particle Identification
ISF	Inverse Scale Factor
ITS	Inner Tracking System
LHC	Large Hadron Collider
LQ	Likelihood on total deposited charge
LTM	Local Trigger Module
LUT	Look-Up Table
MB	Minimum Bias

Appendix E. List of Acronyms

MC	Monte Carlo
MCM	Multi-Chip Module
MRPC	Mulit-gap Resistive Plate Chamber
MWPC	Multi-Wire Proportional Chamber
NN	Neural Network
ORI	Optical Readout Interface
PASA	Pre-Amplifier and Shaper
PHOS	Photon Spectrometer
PID	Particle Identification
PMD	Photon Multiplicity Detector
PRF	Pad Response Function
QCD	Quantum Chromodynamics
QED	Quantum Electrodynamics
QFT	Quantum Field Theory
QGP	Quark-Gluon Plasma
RICH	Ring Imaging Cherenkov Detector
SDD	Silicon Drift Detector
SF	Scale Factor
SM	Supermodule
SMU	Supermodule Unit
SPD	Silicon Pixel Detector
SSD	Silicon Strip Detector
SW	Summation Window
TC	Tail Cancellation
TMU	Track Matching Unit
TOF	Time Of Flight
TPC	Time Projection Chamber
TPP	Tracklet Preprocessor
TR	Transition Radiation
TRAP	Tracklet Processor
TRD	Transition Radiation Detector
TTC	Trigger Timing and Control
ZDC	Zero Degree Calorimeter

Bibliography

[1] P. Braun-Munzinger and J. Stachel. The quest for the quark-gluon plasma. *Nature*, 448(7151):302–309, 2007. doi:10.1038/nature06080.

[2] K. Nakamura et al. (Particle Data Group). Review of Particle Physics. *Journal of Physics G*, 37, 075021 (2010) and 2011 partial update for the 2012 edition. URL `http://pdg.lbl.gov`.

[3] S. Chatrchyan et al. (CMS Collaboration). Search for a heavy bottom-like quark in pp collisions at $\sqrt{s} = 7$ TeV. *Physics Letters B*, 701(2):204–223, 2011.

[4] I. J. R. Aitchison, A. J. G. Hey. *Gauge Theories in Particle Physics, Volume I: From Relativisitc Quantum Mechanics to QED.* Graduate student series in physics. Taylor & Francis Group, New York London, 3rd edition, 2003.

[5] I. J. R. Aitchison, A. J. G. Hey. *Gauge Theories in Particle Physics, Volume II: Non-Abelian Gauge Theories: QCD and the Electroweak Theory.* Graduate student series in physics. Taylor & Francis Group, New York London, 3rd edition, 2004.

[6] The DOE/NSF Nuclear Science Advisory Committee. The Frontiers of Nuclear Science, A Long Range Plan. arXiv:0809.3137v1 [nucl-ex], 2008.

[7] N. Cabibbo and G. Parisi. Exponential hadronic spectrum and quark liberation. *Physics Letters B*, 59(1):67–69, 1975. doi:10.1016/0370-2693(75)90158-6.

[8] J.C. Collins and M.J. Perry. Superdense Matter: Neutrons or Asymptotically Free Quarks? *Physical Review Letters*, 34(21):1353–1356, 1975. doi:10.1103/PhysRevLett.34.1353.

[9] H. Satz. Limits of Confinement: The first 15 Years of Ultra-Relativisic Heavy Ion Studies. *Nuclear Physics A*, 715:3c–19c, 2003.

[10] A. Rakotozafindrabe et al. Cold Nuclear Matter effects on J/ψ production with extrinsic p_t at $\sqrt{s_{NN}} = 2.76$ TeV at the LHC. *Nuclear Physics A*, 855(1):327–330, 2011. doi:10.1016/j.nuclphysa.2011.02.071.

Bibliography

[11] C. Carli, editor. *Proceedings of the Chamonix 2011 workshop on LHC Performance*, 2011. CERN-ATS-2011-005, URL `https://espace.cern.ch/acc-tec-sector/chamonix.aspx`.

[12] B.G. Zakharov. Variation of jet quenching from RHIC to LHC and thermal suppression of the QCD coupling constant. *JETP Letters*, 93(12):683–687, 2011. doi:10.1134/S0021364011120162.

[13] K. Aamodt et al. (ALICE Collaboration). Suppression of Charged Particle Production at Large Transverse Momentum in Central Pb–Pb Collisions at $\sqrt{s_{NN}}$ = 2.76 TeV. *Physics Letters B*, 696(1-2):30–39, 2011. arXiv:1012.1004v1 [nucl-ex].

[14] B.R. Martin, G. Shaw. *Particle Physics*. John Wiley & Sons, West Sussex, 3rd edition, 2008.

[15] Donald H. Perkins. *Introduction to High Energy Physics*. Cambridge University Press, Cambridge, 4th edition, 2000.

[16] B. Povh, K. Rith, C. Scholz, F. Zetsche. *Teilchen und Kerne: Eine Einführung in die physikalischen Konzepte*. Springer, Berlin Heidelberg, 8th edition, 2009.

[17] C. Aarts et al. Bottomonium at Non-zero Temperature from Lattice Nonrelativistic QCD. arXiv:1109.1475v1 [hep-ph], 2011.

[18] Á. Mócsy. Quarkonia from Lattice and Potential Models. Presentation at the 417th WE-Heraeus-Seminar ("Characterization of the Quark Gluon Plasma with Heavy Quarks") in Bad Honnef, June 2008.

[19] Z. Hu (for the CMS Collaboration). Bottomonium production measured in PbPb and pp collision by CMS. *CMS Conference Report*. CMS-CR-2011-119, 2011.

[20] Jean-Luc Caron. Layout of the LEP tunnel including future LHC infrastructures, 1997. AC Collection. Pictures from 1992 to 2002.

[21] O. Brüning et al. LHC Design Report Volume I: The LHC Main Ring. CERN-2004-003-V1, CERN (Geneva), 2004.

[22] L. Rossi. Superconductivity: its role, its success and its setbacks in the Large Hadron Collider of CERN. *Superconductor Science and Technology*, 23(3):034001, 2010. doi:10.1088/0953-2048/23/3/034001.

[23] K. Aamodt et al. (ALICE Collaboration). The ALICE experiment at the CERN LHC. *Journal of Instrumentation*, 3(8):S08002, 2008. doi:10.1088/1748-0221/3/08/S08002.

[24] ALICE website: The ALICE experiment. URL `http://aliceinfo.cern.ch/Public/en/Chapter2/Chap2Experiment-en.html`.

[25] F. Carminati et al. (ALICE Collaboration). ALICE: Physics Performance Report, Volume I. *Journal of Physics G: Nuclear and Particle Physics*, 30(11):1517–1763, 2004. doi:10.1088/0954-3899/30/11/001.

[26] Y. Schutz. Heavy-Ion Physics at LHC. Presentation at Quark Matter in Oakland, January 2004.

[27] ALICE Collaboration. ALICE Technical Design Report of the Inner Tracking System (ITS). Technical report, CERN/LHCC 99-12, CERN, 1999.

[28] ALICE Collaboration. ALICE Technical Design Report of the Time Projection Chamber. Technical report, CERN/LHCC 2000-00 1, CERN, 2000.

[29] K. Aamodt et al. (ALICE Collaboration). Rapidity and transverse momentum dependence of inclusive J/ψ production in pp collisions at $\sqrt{s} = 7$ TeV. CERN-PH-EP-2011-057. arXiv:1105.0380v2 [hep-ex], 2011.

[30] ALICE Collaboration. ALICE Technical Design Report of the Time of Flight System (TOF). Technical report, CERN/LHCC 2000-12, CERN, 2000.

[31] ALICE Collaboration. ALICE Technical Design Report of the High Momentum Particle Identification Detector. Technical report, CERN/LHCC 98-19, CERN, 1998.

[32] ALICE Collaboration. ALICE Technical Design Report of the Photon Spectrometer (PHOS). Technical report, CERN/LHCC 99-4, CERN, 1999.

[33] ALICE Collaboration. ALICE Electromagnetic Calorimeter Technical Design Report. Technical report, CERN/LHCC 2008-014, CERN, 2008.

[34] ALICE Collaboration. ALICE Technical Design Report of the Dimuon Forward Spectrometer. Technical report, CERN/LHCC 99-22, CERN, 1999.

[35] ALICE Collaboration. ALICE Technical Design Report on Forward Detectors: FMD, T0 and V0. Technical report, CERN-LHCC-2004-025, CERN, 2004.

[36] A. Fernández et al. (ACORDE Collaboration). ACORDE a cosmic ray detector for ALICE. *Nuclear Instrumentation and Methods in Physics Research A*, 572(1):102–103, 2007. doi: 10.1016/j.nima.2006.10.336.

[37] ALICE Collaboration. ALICE Technical Design Report of the Trigger Data Acquisition High-Level Trigger and Control System. Technical report, CERN/LHCC 2003-062, CERN, 2004.

Bibliography

[38] The ALICE Off-line Project. URL `http://aliweb.cern.ch/Offline/AliRoot/Manual.html`.

[39] An Object-Oriented Data Analysis Framework. URL `http://root.cern.ch/`.

[40] The ALICE Offline Bible. URL `http://aliceinfo.cern.ch/Offline/AliRoot/Manual.html`.

[41] J. D. Jackson. *Classical Electrodynamics.* John Wiley & Sons, New York, 3rd edition, 1998.

[42] ALICE Collaboration. ALICE Technical Design Report of the Transition Radiation Detector. Technical report, CERN/LHCC 2001-021, CERN, 2001.

[43] A. Wilk. *Particle Identification Using Artificial Neural Networks with the ALICE Transition Radiation Detector.* PhD thesis, University of Münster, Institut für Kernphysik, 2010.

[44] R. Bailhache. *Calibration of the ALICE Transition Radiation Detector and a study of Z^0 and heavy quark production in pp collisions at the LHC .* PhD thesis, Tech. University of Darmstadt, 2008.

[45] J. de Cuveland. *Entwicklung der globalen Spurrekonstrukionseinheit für den ALICE-Übergangsstrahlungsdetektor am LHC (CERN).* Diploma thesis, University of Heidelberg, Kirchoff-Insitut für Physik, 2003.

[46] U. Westerhoff. *The FEE Server Control Engine of the ALICE-TRD.* Diploma thesis, University of Münster, Institut für Kernphysik, 2009.

[47] V. Angelov et al. *ALICE TRAP User Manual,* revision 1.1, 2005. Latest version: URL `https://alice.physi.uni-heidelberg.de/svn/trd/TRAP_docu/trunk/`.

[48] Homepage of the ETM company. URL `http://www.etm.at/`.

[49] J. Mercardo. *Development of the control system of the ALICE Transition Radiation Detector and of a test environment for quality-assurance of its front-end electronics.* PhD thesis, University of Heidelberg, Physikalisches Institut, 2008.

[50] J. Klein. *Commissioning of and Preparations for Physics with the Transition Radiation Detector in A Large Ion Collider Experiment at CERN.* Diploma thesis, University of Heidelberg, Physikalisches Institut, 2008.

[51] CMS Collaboration. Upsilon production cross section in *pp* collisions at $\sqrt{s} = 7$ TeV. *CMS Physics Analysis Summary.* CMS-PAS-BPH-10-003 (2010), 2010.

[52] Norbert Herrmann. Private communication.

[53] Yvonne C. Pachmayer. Private communication.

[54] K. Oyama (for the ALICE Collaboration). Cross section normalization in ALICE. Presentation at Quark Matter in Annecy, May 2011.

[55] T. Dietel, J. Klein, K. Oyama, K. Schweda. *TRD Documentation Project*, May 2010.

[56] E. Scapparone et al. A topological trigger based on the Time-of-Flight detector for the ALICE experiment. *Nuclear Instrumentation and Methods in Physics Research A*, 602(2):372–376, 2009. doi:10.1016/j.nima.2008.12.016.

[57] D. Acosta et al. (CDF Collaboration). Υ Production and Polarization in $p\bar{p}$ Collisions at $\sqrt{s} = 1.8$ TeV. *Physical Review Letters*, 88(16):161802, 2002. doi:10.1103/PhysRevLett.88.161802.

[58] B. Alessandro et al. (ALICE Collaboration). ALICE: Physics Performance Report, Volume II. *Journal of Physics G: Nuclear and Particle Physics*, 32(10):1295–2040, 2006. doi:10.1088/0954-3899/32/10/001.

[59] ALICE Trigger Pattern. URL http://aliweb.cern.ch/Offline/Activities/TriggerPattern.html.

[60] Jochen Klein. Private communication.

[61] A. Andronic (for the ALICE TRD Collaboration). Electron identification performance with ALICE TRD prototypes. *Nuclear Instrumentation and Methods in Physics Research A*, 522(1-2):40–44, 2004. doi:10.1016/j.nima.2004.01.015.

[62] T. Mahmoud (for the ALICE TRD Collaboration). The ALICE transition radiation detector. *Nuclear Instrumentation and Methods in Physics Research A*, 502(1):127–132, 2003. doi:10.1016/S0168-9002(02)02168-X.

[63] U. Westerhoff. *Thesis in preparation.* PhD thesis, University of Münster, Institut für Kernphysik.

[64] Anton Andronic. Private communication.

[65] C. Adler et al. Position reconstruction in drift chambers operated with Xe, CO_2 (15%). *Nuclear Instrumentation and Methods in Physics Research A*, 540(1):140–157, 2005. doi:10.1016/j.nima.2004.11.016.

[66] Raphaëlle Bailhache. Private communication.

[67] Yifei Wang. Private communication.

Bibliography

[68] W. Blum, W. Riegler, L. Rolandi. *Particle Detection with Drift Chambers.* Springer, Berlin Heidelberg, 2nd edition, 2008.

[69] Timetric website: Atmospheric pressure at Geneva Airport, Switzerland – LSGG. URL `http://timetric.com/dataset/metar/?indexes=atmospheric-pressure-geneva-airport-switzerland-lsgg-metar`.

[70] G. Cowan. *Statistical Data Analysis.* Oxford University Press, Oxford, 1998.

[71] Uwe Westerhoff. Private communication.

[72] X. Lu. *Thesis in preparation.* PhD thesis, University of Heidelberg, Physikalisches Institut.

[73] A. Andronic, S. F. Biagi, P. Braun-Munzinger, C. Garabatos and G. Tsiledakis. Drift velocity and gain in argon- and xenon-based mixtures. *Nuclear Instrumentation and Methods in Physics Research A*, A523:302-308, 2004. doi:10.1016/j.nima.2003.11.426.

[74] Oliver Busch. Private communication.

[75] M. Al Helwi. *Gain Calibration of the ALICE Transition Radiation Detector with Krypton-83.* Diploma thesis, University of Heidelberg, Physikalisches Institut, 2010.

[76] J. Stiller. *Thesis in preparation.* Diploma thesis, University of Heidelberg, Physikalisches Institut.

[77] L. Betev, P. Chochula. Definition of the ALICE Coordinate System and Basic Rules for Sub-detector Components Numbering. ALICE Internal Note ALICE-INT-2003-038, 2003. URL `http://edms.cern.ch/file/406391/1`.

[78] Stefan Kirsch. Private communication.

Acknowledgements

At this point, I want to thank Prof. Dr. Johanna Stachel for the outstanding opportunity to work in this comprehensive and interesting field of research, accompanied by very exciting times at CERN.

Many special thanks go to Jochen Klein and Uwe Westerhoff for their enlightening discussions and their close and productive collaboration.

I also would like to thank Xianguo Lu for his help with the deposited charge fits.

Furthermore, I greatly appreciate the instructive discussions with Yvonne Pachmayer and Prof. Norbert Herrman.

For the introduction to life at CERN and valuable advices, I am very grateful to Dr. Kai Schweda and Dr. Ken Oyama.

I would like to thank GSI and the Physikalisches Institut Heidelberg for offering me plenty of computer power and data.

For a detailed review of my thesis, I want to express my gratitude to Jochen Klein, Yvonne Pachmayer, Kai Schweda and Uwe Westerhoff.

Last but not least, I am deeply indebted to my girlfriend for her outstanding patience, understanding and her support.

Erklärung:

Ich versichere, dass ich diese Arbeit selbstständig verfasst habe und keine anderen als die angegebenen Quellen und Hilfsmittel benutzt habe.

Heidelberg, den (Datum)   . . . .